論文 / 著書情報
Article / Book Information

題目(和文)	プラスチック光ファイバ中のブリルアン散乱特性の解明とそのセンシング応用
Title(English)	A Study on Brillouin Scattering Properties in Plastic Optical Fibers for Sensing Applications
著者(和文)	林寧生
Author(English)	neisei hayashi
出典(和文)	学位:博士（工学）, 学位授与機関:東京工業大学, 報告番号:甲第9880号, 授与年月日:2015年3月26日, 学位の種別:課程博士, 審査員:中村　健太郎,黒澤　実,田原　麻梨江,植之原　裕行,宮本　智之
Citation(English)	Degree:, Conferring organization: Tokyo Institute of Technology, Report number:甲第9880号, Conferred date:2015/3/26, Degree Type:Course doctor, Examiner:,,,,
学位種別(和文)	博士論文
Type(English)	Doctoral Thesis

Dissertation

博士号請求論文

A Study on Brillouin Scattering Properties in Plastic Optical Fibers for Sensing Applications

プラスチック光ファイバ中のブリルアン散乱特性の解明とそのセンシング応用

Supervisor: **Professor Kentaro Nakamura**

指導教員: 中村 健太郎 教授

Submitted on Feb. 24, 2014

2015年2月24日提出

Department of Information Processing
Interdisciplinary Graduate School of Science and Engineering,
Tokyo Institute of technology

東京工業大学大学院総合理工学研究科物理情報システム専攻

Neisei HAYASHI

林 寧生

Abstract

Due to their light weight, small diameter, immunity against electro-magnetic noise, etc., optical fiber sensors have been increasingly required for monitoring diverse civil structures, such as buildings, dams, levees, bridges, pipelines, tunnels, and aircraft wings. Above all, Brillouin scattering-based fiber-optic sensors have been extensively studied because they can measure strain/temperature distribution along the fibers. To date, only glass optical fibers have been used for their sensor heads, but they are quite fragile and cannot withstand strains of approximately 3%. As one method of solving this problem, employing polymer/plastic optical fibers (POFs) in such Brillouin sensors has attracted considerable attention, which have extremely high flexibility and can withstand > 50% strain. POFs also have a unique feature called the “memory effect”, with which the information on the applied large strain can be stored owing to their plastic deformation.

In this dissertation, we study on distributed strain and temperature sensing based on Brillouin scattering in POFs. To begin with, we clarify the unique Brillouin properties in POFs. We then provide the first demonstration of distributed sensing. Besides, we conduct some research related to its performance improvement. In the following paragraphs, we describe these three topics in detail.

As for the clarification of the Brillouin properties in POFs, first, we observe the non-monotonic dependence of Brillouin gain spectra (BGSs) on relatively large strain of < 20%. Subsequently, we investigate the BGS dependence on larger strain of up to 60% and observe abrupt upshift of the Brillouin frequency shift (BFS), which phenomenon we name the “BFS hopping.” Finally, we experimentally show that, after this effect occurs, Brillouin scattering in POFs is applicable to extremely high-precision temperature sensing with low strain sensitivity.

As for the first demonstration of distributed strain and temperature sensing using POFs, we succeed in achieving a centimeter-order spatial resolution and a high signal-to-noise ratio (SNR) by employing Brillouin optical correlation-domain reflectometry (BOCDR). We then clarify the performance limitation of this system and develop two configurations of simplified BOCDR setups, both of which are experimentally shown to work appropriately.

The additional achievements related to the performance improvement of the POF-based distributed sensors consist of the following five parts: (i) clarification of the stimulated Brillouin scattering properties in POFs for SNR enhancement; (ii) estimation of the Brillouin properties in PMMA-POFs toward higher-sensitivity temperature sensing; (iii) fast flaw detection in POFs using infrared thermometry for efficient selection of high-quality POFs to be used as sensor heads; (iv) observation of BGS in tapered POFs toward implementation of a memory function regarding temperature; and (v) observation of a fiber fuse phenomenon in POFs toward understanding of the performance limitation of POF-based Brillouin sensors.

In Chapter 1: “Introduction,” the time-, frequency-, and correlation-domain techniques are reviewed as the background of this work. The characteristics of POFs are then explained. Brillouin scattering in POFs is also described with some recent progress. The ultimate performance of POF-based Brillouin sensors is theoretically estimated.

In Chapter 2: “Brillouin properties in large-strain applied POFs,” in Section 1: “Brillouin gain spectrum (BGS) dependence on large strain,” first, we investigate the dependence of BGS on large strain of > 20% in a perfluorinated graded-index (PFGI-) POF at 1.55 μm, and prove that the dependence of BFS is highly non-monotonic. We predict that temperature sensors even with zero strain sensitivity can be implemented by use of this non-monotonic nature. Meanwhile, the Stokes power decreases rapidly when the applied strain is > ~10%. This behavior seems to originate from the propagation loss dependence on large strain. By exploiting the Stokes power dependence, we can probably solve the problem of how to identify the applied strain, when the identification is difficult only by BFS because of its non-monotonic nature.

In Chapter 2, Section 2: “Brillouin frequency shift hopping,” we investigate the BGS dependence on large strain of up to 60% in a POF, and find that the BFS abruptly changes from ~2.7 GHz to ~3.2 GHz. We name this phenomenon “BFS hopping,” and find it to originate from the varied acoustic velocity induced by the stepwise change in the core diameter of the POF. This is because of the yielding of the overcladding layer composed of polycarbonate. Then the use of the Stokes power ratio (defined as the ratio of the Stokes power of the new peak to that of the initial peak) to determine the large strain applied to the POF is discussed. After the occurrence of the BFS hopping phenomenon, the BFS dependence coefficients on strain and temperature in the POF are measured to be −65.6 MHz/% and −4.04 MHz/K respectively. These values indicate that, compared to an unstrained POF, further higher-precision temperature sensing with lower strain sensitivity is feasible.

In Chapter 3: “Distributed strain and temperature sensing using POFs,” in Section 1: “First demonstration based on BOCDR,” we present the first demonstration of distributed strain/temperature sensing with a high spatial resolution in POFs based on BOCDR. A 50-cm-long strained (or heated) POF section is clearly detected with a theoretical spatial resolution of 34 cm, a high sampling rate of 3.3 Hz, and a high SNR. A 10-cm-long heated POF section is also successfully detected with a theoretical resolution of 7.4 cm. The performance limitation of this system is then discussed.

In Chapter 3, Section 2: “Simplification of experimental setup,” first, we develop simplified (S-) BOCDR, where the light Fresnel-reflected at a partial reflection point (or the fiber end) is used as reference light and an additional reference path used in standard implementations can be removed. This configuration is useful for practical application and enhancement of SNR in BOCDR. Then, we implement S-BOCDR using a POF as a fiber under test, which provides the following advantages over S-BOCDR using a standard silica single-mode fiber (SMF): (1) the Fresnel-reflected light can be stably returned at the interface between the POF and an SMF (the pigtail of an optical circulator), and (2) the effect of the 0th correlation peak can be easily and effectively suppressed by exploiting a so-called BFS-hopping phenomenon. We then experimentally demonstrate a distributed measurement and detect a 0.46-m-long heated POF section.

In Chapter 4: “Relevant work for improvement of POF-based Brillouin sensors,” in Section 1: “Characterization of stimulated Brillouin scattering in POFs,” we observe stimulated Brillouin scattering in POFs using a pump-probe technique without lock-in detection, and fully investigate the dependences of the BGS on POF length, pump power, probe power, and temperature. Since the POF has relatively high propagation loss of 250 dB/km at 1.55 μm, an optimal POF length exists for SBS observation, which is found to be approximately 3.8 m with 21.1-dBm pump and 22.2-dBm probe waves. As the probe and pump powers are increased, the Stokes power is also raised but nonlinearly. The temperature dependence of the BFS is –4.02 MHz/K, which agrees well with the previous report. These results indicate that the Brillouin signal in POFs observed with this technique can be directly applied to the development of POF-based Brillouin optical time-domain analysis systems for high-precision temperature sensing.

In Chapter 4, Section 2: “Estimation of Brillouin properties in PMMA-POFs,” first, in order to confirm the validity of this method, we show that the estimated BFS of a PFGI-POF of ~2.9 GHz at 1.55 μm moderately agrees with the actual value previously reported. Then, we measure the acoustic velocity in a poly(methyl methacrylate)-based (PMMA-) POF with a 980 μm core diameter to be 2.8×10^3 m/s, from which its BFS is estimated to be ~5.4 GHz at 1.55 μm and ~13 GHz at 650 nm. We also find that the BFS varies linearly depending on temperature with a coefficient of approximately –17 MHz/K at 650 nm pump. Since this value is –7.1 times larger than that of silica fibers at 650 nm (2.4 MHz/K), and is even 1.7 times larger than that of PFGI-POFs at 650 nm (–10.0 MHz/K), we think that PMMA-POFs are potentially applicable to high-precision temperature sensing.

In Chapter 4, Section 3: "Fast flaw detection in POFs using infrared thermometry," we demonstrate a fast and cost-effective method of detecting flaws in POFs using an infrared thermometer. The optical loss dependence of the measured temperature at the flaw is found to be linear with a proportionality constant of approximately 0.74 °C/dB when the propagating light is 24.5 dBm (282 mW) at 1.55 μm. The propagating optical power dependence of the measured temperature at the flaw with a fixed loss also shows a linear behavior, which predicts that a high optical input power is preferable to precise estimation of the loss.

In Chapter 4, Section 4: "Observation of BGS in tapered POF," we report on the first observation of the BGS in a PFGI-POF tapered by a heat-and-pull technique. The Stokes power is slightly enhanced by tapering probably on account of higher optical power density in the core. In addition, the BFS is decreased by ~40 MHz, which is experimentally verified to be partially caused by high heating temperature applied to the POF during the taper fabrication process. We anticipate that our findings will provide a basic principle of temperature sensing with "memory" function.

In Chapter 4, Section 5: "Observation of POF fuse," we report on the observation of POF fuse phenomenon. Although optical fibers with a high transmission capacity are in demand, the problem of the fiber fuse phenomenon needs to be resolved to prevent the destruction of fibers. Here, we experimentally demonstrate a fuse propagation velocity of 21.9 mm/s, which is 1‑2 orders of magnitude slower than that in standard silica fibers. The achieved threshold power density and proportionality constant between the propagation velocity and the power density are 1/180 of and 170 times the values for silica fibers, respectively. An oscillatory continuous curve instead of periodic voids is formed after the passage of the fuse. An easy fuse termination method is also presented. These results provide a useful guideline for the performance limitation of POF-based Brillouin sensors from the aspect of highest incident power.

In Chapter 5: “Conclusions,” we summarize the achievements of this work and give some open problems and future prospects.

Contents

1 Introduction 1

2 Brillouin properties in large-strain applied POFs 30

1 Introduction

This Chapter describes the overall background and the purpose of this thesis. We start by reviewing the history of optical fibers and their sensing applications called “fiber-optic nerve systems.” A basic principle of fiber-optic sensors based on Brillouin scattering is also described. Then, three sensing technologies such as time-, frequency-, and correlation-domain techniques are explained. Finally, the history, physical properties, and the Brillouin scattering in POFs are overviewed.

1. 1 Background

1. 1. 1 Birth of optical fibers

The history of the optical fibers is showed in Table 1.1. In 1966, Charles K. Kao [1] made a discovery that led to a breakthrough in fiber optics. He carefully calculated how

Table. 1.1. History of optical fibers

Year	Events
1966	Optical transmission capability theoretically predicted [1]
1970	Optical communication experimentally demonstrated [5] (but with high propagation loss)
1979	Propagation loss drastically improved to 0.2 dB/km [7]
2009	C. K. Kao awarded the Nobel Prize in Physics

to transmit light over long distances via optical glass fibers. With a fiber of purest glass it would be possible to transmit light signals over 100 km, compared to only 20 m for the fibers available in the 1960's [2-4]. Kao's enthusiasm inspired other researchers to share his vision of the future potential of fiber optics. The first ultra-pure fiber with a loss below 20 dB/km was successfully fabricated just four years later, in 1970 [5]. Further progress in fabrication technology [6] resulted in a loss of only 0.2 dB/km in the 1.55-μm wavelength region [7], a loss level limited mainly by the fundamental process of Rayleigh scattering. The availability of low-loss silica fibers led not only to a revolution in the field of optical fiber communications [8-11] but also to the advent of the new field of optical fiber sensors [12-17]. In 2009, the Nobel Prize in Physics was awarded for two scientific achievements that have helped to shape the foundations of networked societies. They have created many practical innovations for everyday life and provided new tools for scientific exploration.

1. 1. 2 Optical fiber sensors

Monitoring of structures, such as buildings, bridges, highways, tunnels, dams, pipelines, containers, airplanes, *etc.*, is useful from the economic and security points of view; and so is monitoring of materials [18-22]. To date, such monitoring has been conventionally based on visual inspection [23]. The drawbacks of this method include a long measurement time (caused by the limited range for inspection) and the infeasibility of measuring the internal defects in structures at a glance. One way to overcome these drawbacks is to use electrical or fiber-optic sensors. Electrical sensors are widely used due to their high accuracy, fast measurement speed, high reliability, and low cost [24]. The problem with these sensors is that they cannot be cascaded or multiplexed using a common interrogation unit. Since each strain gauge requires two wires for power supply, some wires for the signal path (in most cases), and an amplifier unit, the sensor system is quite complex, especially when employed to monitor large buildings. Other problems

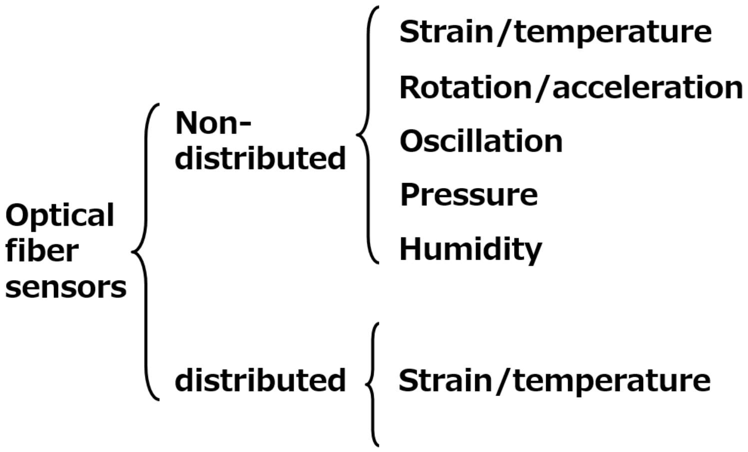

Figure 1.1 Classification of optical fiber sensors.

with strain gauges apart from their poor multiplexing capability are susceptibility to electromagnetic interference (EMI), long-term degradation, and sometimes a restricted temperature range. Meanwhile, fiber-optic sensors have various advantages such as light weight, small size, immunity to EMI, high-temperature tolerance, broad bandwidth, and environmental robustness, and feasibility of completely distributed measurement [25]. Here, sensor types are classified into two: non-distributed and distributed sensors, as shown in Fig. 1.1. Non-distributed sensors have been used to measure a variety of physical parameters including strain/temperature [26-28], rotation/acceleration [29,30], oscillation [31], pressure [32], and humidity [33]. In the meantime, strain and temperature have also been measured using distributed sensors based on nonlinear phenomena such as Rayleigh scattering, Raman scattering, and Brillouin scattering, which will be explained in the next section.

For the health monitoring of the civil structures, optical fiber sensors based on Brillouin scattering have been widely studied so far. After explaining the principle of Brillouin scattering in Section 1.2, conventional distributed sensing techniques based on Brillouin scattering, such as time-, frequency-, and correlation-domain techniques, are reviewed in Section 1.3. In Section 1.4, the history, physical properties, and Brillouin properties of POFs are explained. In Section 1.5, the performance of POF-based Brillouin sensors was estimated. In Section 1.6, the purpose and the constitution of this thesis are described.

1. 2 Brillouin scattering

Light scattering in optical fibers is omnipresent irrespective of the amount of optical power present in the fibers. It can be categorized into two regimes: spontaneous and stimulated scatterings [34]. Spontaneous light scattering refers to the process under conditions such that the optical material properties are unaffected by the presence of the incident electric field. For input optical fields of sufficient intensities, spontaneous light scattering becomes quite intense; thus in the stimulated regime the nature of the scattering process grossly modifies the optical properties of the material system and vice versa. Spontaneous and stimulated scattering in optical fibers can result from Raman, and Brillouin scattering phenomena. Each scattering process is always present in optical fibers, because no fiber is free from microscopic defects or thermal fluctuations which originate the three processes. For a monochromatic incident lightwave at frequency f_0, the three processes are well described in Fig. 1.2.

These scattering phenomena physically correspond to two main cases: elastic scattering and inelastic scattering. In elastic scattering, that is, Rayleigh scattering, the scattered photons maintain their energy and thus have the same frequency of the incident light. On the other hand, in inelastic scattering, that is, Brillouin scattering (interaction with acoustic phonons) and Raman scattering (interaction with optical phonons), the scattered photons lose or gain energy and thus undergo a frequency shift. In “Stokes-type” scattering, the photons lose energy and their frequency is down-shifted; in “anti-Stokes-type” scattering, the photons gain energy with their frequency up-shifted. Here we should note that there is large difference in frequency shift between these scatterings for either

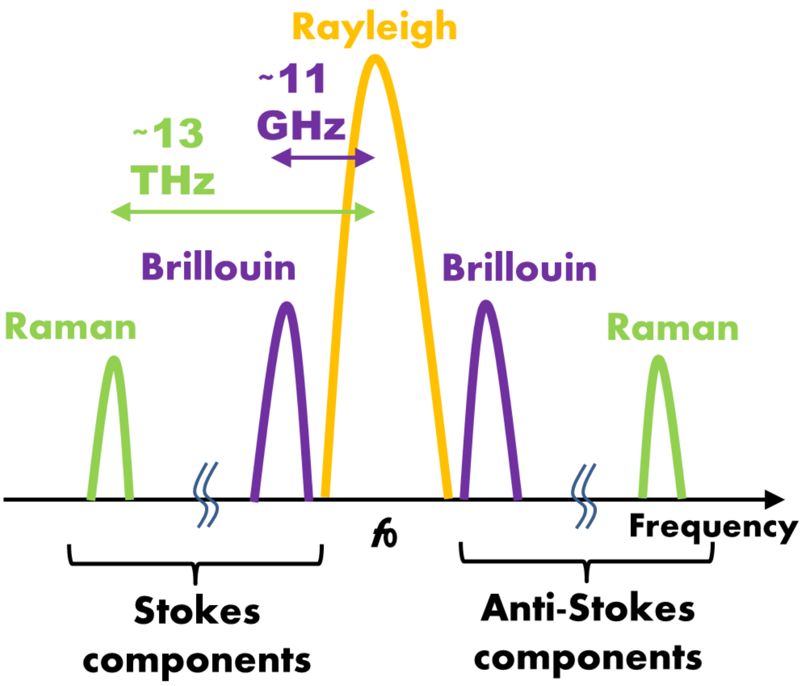

Figure 1.2 Schematics of the spectra of the reflected light due to Rayleigh, Brillouin, and Raman scattering in silica fibers at 1.55 µm.

Stokes-type or anti-Stokes-type scattering, though we made a combined depiction of them in Fig. 1.2.

Among the three scatterings, Brillouin scattering is especially suitable for making distributed sensors, because its frequency shift is linearly dependent on both strain [35] and temperature [36], as described later. So, in this thesis, we will focus on Brillouin scattering. Brillouin scattering is a photon-phonon interaction, in other words, it is based on the annihilation of a pump photon that creates a Stokes photon and a phonon simultaneously. The phonon is the vibrated modes of atoms, which is also called a propagation density wave or an acoustic phonon. The Brillouin frequency shift (BFS) is about 11 GHz in silica fibers, and the Brillouin-scattered light is dominantly down-shifted in frequency due to the Doppler effect associated with the forward-moving acoustic waves.

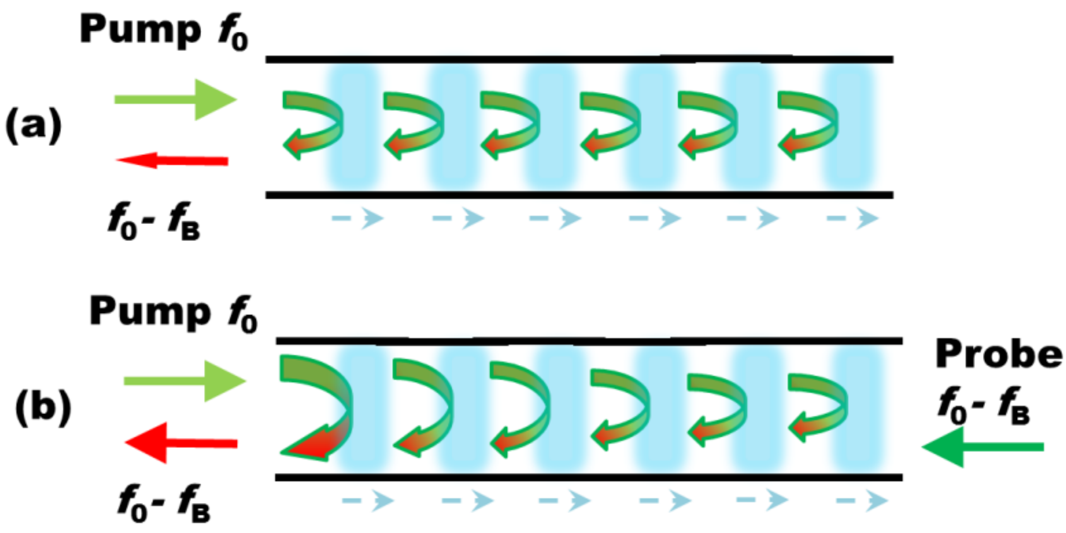

Figure 1.3 Schematics of (a) spontaneous Brillouin scattering, and (b) stimulated Brillouin scattering.

The spectrum of the Brillouin-scattered Stokes light is called Brillouin gain spectrum (BGS), which includes three important parameters: the Brillouin gain peak coefficient g_{B0}, the BFS, and the Brillouin bandwidth $\Delta\nu_B$. The gain peak coefficient g_{B0} lies in the range of 1.5–3×10^{-11} m/W [37, 38]. The BFS f_B (or ν_B) is given by [34]

$$f_B = \frac{2}{\lambda} n \cdot v_a = \frac{2n}{\lambda}\sqrt{\frac{E}{\rho}}, \tag{1.1}$$

where n is the effective refractive index of the fiber, and v_a is the effective longitudinal acoustic velocity, E the Young's modulus, and ρ the density. Both n and v_a are determined by the waveguide structures of the optical modes and the longitudinal modes, which are related to the silica dopant materials and their distributions along the cross section of the fiber [39]. The Brillouin bandwidth $\Delta\nu_B$ is originally decided by the damping lifetime $\tau_{dp}\ (=1/\Gamma)$ of acoustic phonons as

$$\Delta\nu_B = \frac{\Gamma}{2\pi} \quad , \tag{1.2}$$

where Γ denoted the decay rate of the acoustic phonons in the fiber. The typical value of $\Delta\nu_B$ is about 30 MHz.

As is already mentioned, Brillouin scattering is classified into two configurations: spontaneous Brillouin scattering and stimulated Brillouin scattering (SBS). The configuration for spontaneous Brillouin scattering is shown in Fig. 1.3(a), where only one pump light beam is injected into one end of the fiber. Its reflectivity is –90 dB/m, which is even lower than Rayleigh scattering. In contrast, the reflectivity of stimulated Brillouin scattering is about –50 dB/m. In order to induce stimulation, a probe light beam is injected to the other end of the fiber in addition to the pump light, as shown in Fig. 1.3(b).

In general, the Stokes power grows higher with increasing pump power. When the pump power becomes higher than a certain power called Brillouin threshold, the Stokes power begins to drastically increase due to the transition from SpBS to SBS. The Brillouin threshold P_{th} is expressed as [40]

$$P_{\mathrm{th}} = \frac{21bA_{\mathrm{eff}}}{Kg_{\mathrm{B}}L_{\mathrm{eff}}} , \tag{1.3}$$

where A_{eff} is the cross-sectional area and b is the correction factor for MMFs, which can be treated as 2 when the numerical aperture (NA) is ~0.2. K is the polarization factor [41,42], which is 1 if the polarization is maintained and 0.667 otherwise. L_{eff} is the effective length, which is defined as [34]

$$L_{\mathrm{eff}} = [1 - exp(-\alpha L)]/\alpha \tag{1.4}$$

(α, propagation loss; L, fiber length). g_{B} is the Brillouin gain coefficient, which is given by [42]

$$g_{\mathrm{B}} = \frac{2\pi p_{12}^2 n^7}{c\lambda_{\mathrm{p}}^2 \rho \upsilon_{\mathrm{A}} \Delta \nu_{\mathrm{B}}} , \tag{1.5}$$

where p_{12} is the longitudinal elasto-optic coefficient, n is the refractive index, c is the light velocity, λ_{p} is the optical wavelength, ρ is the density, and $\Delta\nu_{\mathrm{B}}$ is the Brillouin linewidth; υ_{A} is the acoustic velocity, which is a function of BFS.

Around 1990, it was clarified that the BFS has a good linear dependences on strain [35] and/or temperature [36], which can be expressed by

$$\Delta BFS = f_B - f_{B0} = C_{\varepsilon} \cdot \Delta\varepsilon + C_T \cdot \Delta T , \tag{1.6}$$

where C_{ε} and C_{T} are the strain and temperature coefficients of the BFS in the fiber; f_{B0} is the BFS at room temperature and in loose state as a reference point. Although the strain and temperature coefficients even in single-mode fibers (SMFs) are slightly different among each fiber, their typical values are C_ε ~ 0.04-0.05 MHz/με and C_T ~ 1.0-1.2 MHz/K at 1.55-μm wavelength. These linear dependences of the BFS on strain and temperature are the basic principles to measure the magnitude of strain and temperature change in Brillouin scattering-based optical fiber sensors.

1. 3 Distributed optic-fiber sensing techniques

1. 3. 1 Time-domain techniques

While the efficiency of spontaneous Brillouin scattering is extremely low, SBS allows much stronger signals to be produced. The first concept of Brillouin scattering-based distributed sensing was demonstrated by Horiguchi *et al.* and was named Brillouin optical time-domain analysis (BOTDA) [43-45]. In their configuration, as shown schematically in Fig. 1.4, a short pump pulse is sent into one end of the fiber under test (FUT), while a continuous wave probe beam with a frequency offset corresponding to the nominal BFS is launched into the other end of the FUT. The continuous wave (CW) probe light experiences Brillouin gain at the locations in the FUT where the frequency offset is matched to the peak Brillouin gain. Thus, the time dependence of the detected CW light provides the gain profile experienced by the probe light as the pump pulse passes along the FUT. Measurements carried out with a wide range of frequency offsets allow a full picture of the Brillouin frequency for each location in the FUT to be achieved. As a consequence, the distribution of strain and temperature can be derived within the spatial resolution determined by the width of the pump pulse τ_w, as

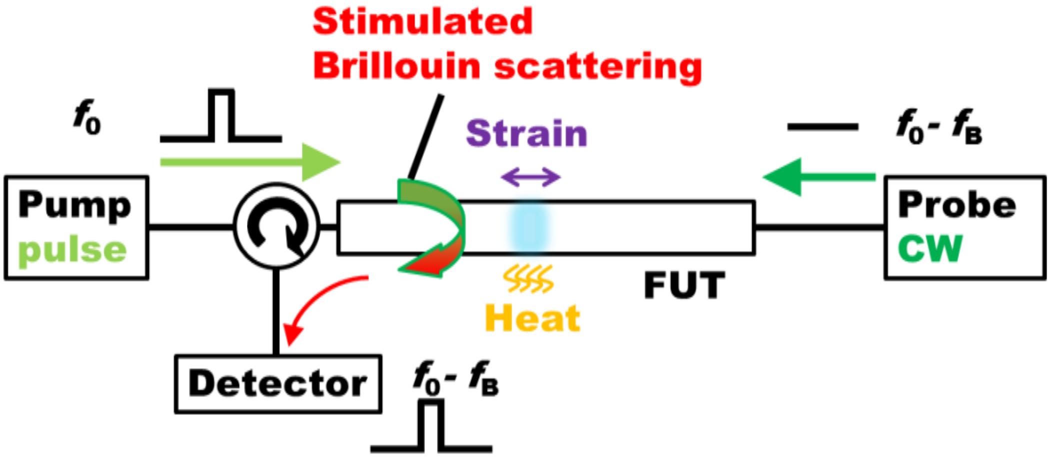

Figure 1.4 Schematic of basic BOTDA system.

$$\Delta z = \frac{c\tau_w}{2n} \quad , \tag{1.7}$$

where c is the light velocity in a vacuum.

Horiguchi *et al.* [46, 47] demonstrated 1-m spatial resolution with an 11-km SMF using 10-ns optical pulses generated by modulating 1.55-μm distributed-feedback laser diode (DFB-LD) with a combination of a fast electro-optic modulator (EOM) and an acousto-optic modulator (AOM). In their experiment, the linewidth of the measured BGS was about 80 MHz, which is about twice of that of spontaneous Brillouin scattering in the SMF. This is because the 10-ns optical pulse is comparable in bandwidth to the intrinsic BGS, and the frequency-convolved spectrum between the wide pulse and the BGS suffers broadening. As a consequence, it becomes difficult to accurately diagnose the BFS, and the reported accuracy was ~ 5 MHz corresponding to ~ 100 με. Hence, the ultimate spatial resolution of BOTDA is in principle limited to ~ 1 m [48,49].

To date, many researchers have been improving BOTDA systems to achieve enhanced spatial resolution [55-60] and extended measurement range [61,62]. As for the spatial resolution enhancement, Nikles *et al.* [53] proposed a method to stabilize the distribution of BGS and BFS by using an EOM to modulate a DFB-LD at 1.55 μm and thus generate the pump and the probe light beams from the same DFB-LD source. They achieved 80-cm spatial resolution and 1-km measurement range simultaneously, with a frequency resolution of 1 MHz corresponding to 20 με. Bao *et al.* [54] developed a Brillouin-loss-based BOTDA by reversing the functions of the coherent pulse laser and CW light. In this configuration, the strong CW light acts as a Brillouin pump wave, and the optical pulse with a scanned down-shifted frequency from that of the CW light works as a probe wave. By monitoring the Brillouin loss profile due to Brillouin interaction between the two light beams as a function of time or position along the FUT, they reported 25-cm spatial resolution [55] with a strain resolution of ~ 40 με. Recently, a "pulse pre-pump BOTDA" system was proposed [56,57], where ~10-ns pulse followed by 1-ns pulse was used to pre-excite the phonon field and obtain a resolution of ~10 cm. A "dark-pulse BOTDA" system with 2-cm spatial resolution was also developed [58,59], and was achieved. In 2010, BOTDA was implemented exploiting a Brillouin dynamic grating [60], in which 1-cm spatial resolution was achieved. This is one of the highest spatial resolutions ever reported in BOTDA systems. As for the measurement range extension, Soto *et al.* [61] achieved a measurement range of up to 120 km (with a spatial resolution of 5 m) by exploiting Raman amplification and optical pulse coding. Bao *et. al*. [62] obtained a 150-km measurement range by combined use of frequency-division multiplexers and in-line erbium-doped fiber (EDF) amplifiers.

Spontaneous Brillouin scattering-based fiber-optic distributed sensors called Brillouin optical time-domain reflectometry (BOTDR) was also explored [63,64]. Their schematic is shown in Fig. 1.5. One of the biggest advantages of BOTDR is that it works by light injection only from one end of the fiber. The techniques for BOTDR can be classified into two: the direct detection [63] and the coherent (heterodyne) detection [64]. In direct detection [63], the Brillouin signal must be optically separated from the large Rayleigh component before its detection, using FPIs, Mach-Zehnder interferometers, FBG-based optical filters, *etc*. Since the BFS is small, these optical filters must be highly

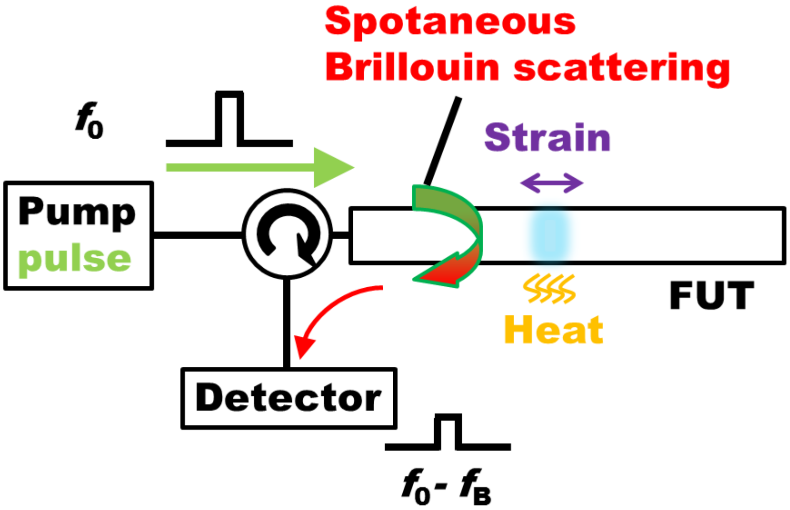

Figure 1.5 Schematic of basic BOTDR system.

stabilized.

In coherent detection [64], a strong narrow-linewidth reference oscillator such as part of the pump lightwave is employed, which allows excellent electrical selection of the Brillouin component as well as a greater dynamic range. The coherent detection had been achieved by the methods that employ frequency shift between the reference oscillator and the sensing pulses that is approximately equal to the BFS, bringing the signal-reference beat frequency within the bandwidth of a conventional photo-detector (PD). This frequency shift of the reference oscillator was attained by an AOM [64] or an EOM [65]. However, thanks to the development of electronics, recently PDs with extremely wide bandwidths (20 GHz or higher) have become commercially available. So, nowadays we do not necessarily employ the frequency shifter in the reference path.

The performance of BOTDR has also been improved. As was explained in the case of BOTDA [48,49], the spatial resolution of basic BOTDR is also limited to 1 m, because the BGS broadens rapidly as the optical pulse width decreases below 10 ns. However, a "double-pulse BOTDR" system was proposed by Koyamada *et al.* [66-68] to enhance the spatial resolution further, where double optical pulses are transmitted into the FUT instead of a conventional single optical pulse. So far, they have experimentally obtained 20-cm resolution. Wang *et. al.* [69] have experimentally achieved a 0.1-m spatial resolution in a 1-km FUT using complex data processing which they call the iterative subdivision method. To enlarge the measurement range, Raman amplification was employed to BOTDR with the coherent detection, resulting in 150-km range [70]. A new BOTDR system based on optical-pulse coding has also been proposed and studied [71,72].

1. 3. 2 Frequency-domain techniques

An alternative technique to build Brillouin scattering-based distributed sensors was demonstrated based on frequency-domain method, and was named Brillouin optical frequency-domain analysis (BOFDA) [73-76]. It employs a CW probe beam and a pump beam with sinusoidally-modulated intensity. When SBS occurs, the probe signal acquires an intensity modulation at the same frequency of the pump, and the induced modulation is measured by a vector network analyzer for a range of modulation frequencies. The baseband transfer function provides information similar to the pulse response measured in BOTDA or BOTDR. This frequency-domain approach seems to permit improvement of the signal-to-noise ratio (SNR) due to a synchronous detection, but the data analysis is still performed in the time domain after an inverse Fourier transform of the measured huge-size data. To date, Bernini *et. al.* [77] have achieved 3-cm spatial resolution using the iterative subdivision method.

1. 3. 3 Correlation-domain techniques

In order to mitigate the limitation of the spatial resolution and the measurement time in other techniques, a novel correlation-domain technology named Brillouin optical correlation-domain analysis (BOCDA) was proposed by Hotate *et al.* [78-100]. BOCDA is based on the technique called the synthesis of the optical coherence function (SOCF) [101-114], where the correlation between frequency-modulated lightwaves is controlled. The SOCF technique has so far been employed to develop FBG-multiplexed sensing

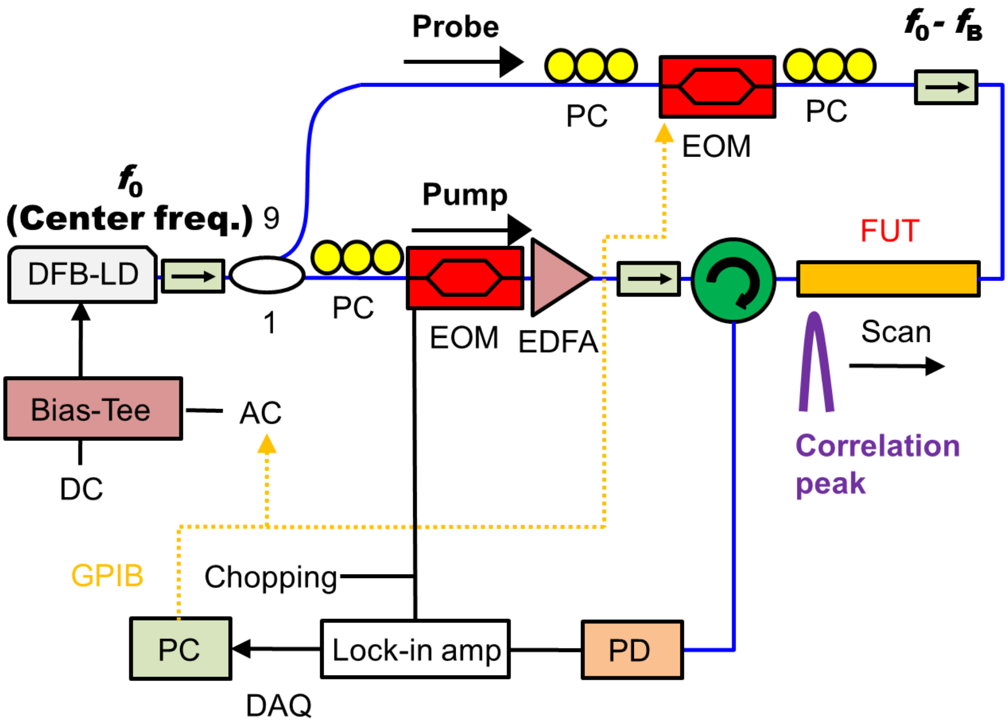

Figure 1.6 Schematic of basic BOCDA system. AC, alternating current; DAQ, data acquisition; DC, direct current; DFB-LD, distributed-feedback laser diode; EDFA, erbium-doped fiber amplifier; EOM, electro-optic modulator; FUT, fiber under test; GPIB, general-purpose interface bus; PC, personal computer; PD, photo-detector.

[103-105], optical coherence tomography [106,107], dynamic grating in EDFs [108-110], lateral-force sensing based on polarization-mode coupling [111,112], and Rayleigh scattering-based reflectometry [113,114] as well.

The basic experimental setup of BOCDA is depicted in Fig. 1.6. In BOCDA, the frequencies of counter-propagating pump and probe lightwaves are sinusoidally modulated. They are synchronous in phase because the two lightwaves are obtained by dividing the same light source except for a frequency difference, which can be expressed as

$$f_{pump} = f_0 + \Delta f \sin(2\pi f_m t) \quad , \tag{1.8}$$

$$f_{probe} = f_0 - f_B + \Delta f \sin(2\pi f_m t) \quad , \tag{1.9}$$

where f_0 is the optical frequency of the laser source without frequency modulation, f_m the sinusoidal-modulation frequency, Δf the sinusoidal-modulation amplitude, and f_B the frequency difference between pump and probe lightwaves, which is around the BFS of the FUT.

The synchronously-modulated pump and probe lightwaves generate beat power spectra and then intensify the acoustic phonons due to electrostriction effect that interact with the probe amplification from the pump light. The beat spectra have a delta-function-shaped distribution along the fiber due to the SOCF effect [101,102] as shown in Fig. 1.7. According to Hasegawa *et al.*'s detailed calculations [78,79], the observed BGS is expressed, by a 2-dimensional convolution of the beat spectra and the local BGS concerning frequency f and position z, as

$$G(z,f) = B(z,f) \otimes g(z,f) \quad , \tag{1.10}$$

where $B(z, f)$ is the synthesized beat spectra given by

$$B(z,f) = F\left[\left|E_{pump}(z,t)E_{probe}^{\ *}(z,t)\right|^2\right] \quad . \tag{1.11}$$

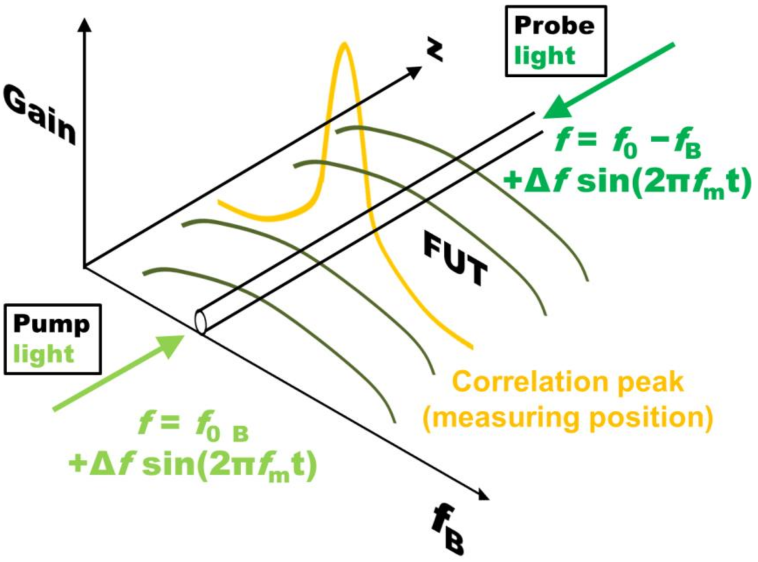

Figure 1.7 Schematic of the correlation peak in BOCDA.

Here $F[\,\cdot\,]$ denotes the operation of Fourier transform, and $g(z, f)$ is a local intrinsic BGS given by

$$g(z,f)=\frac{g_{B0}}{1+4\left[\left\{f-f_B(z)\right\}/\Delta\nu_B\right]^2}\quad . \tag{1.12}$$

The spatial resolution Δz is determined by the relation between the broadened beat spectra and the intrinsic BGS. Meanwhile, the measurement range d_m is determined by the interval between two correlation peaks, because only one correlation peak should exist within the range of the FUT to correctly resolve the strain-applied positions. According to detailed calculations [78,79], the spatial resolution Δz and the measurement range d_m are given by

$$\Delta z=\frac{v_g\cdot\Delta\nu_B}{2\pi\, f_m\Delta f}\quad , \tag{1.13}$$

$$d_m=\frac{v_g}{2\,f_m}\quad , \tag{1.14}$$

where v_g (= c/n) is the light velocity in the FUT. By sweeping f_m, the position of the non-0th correlation peaks can be scanned along the FUT, and thus a distributed measurement becomes feasible.

Up to now, the performance of BOCDA has been improved from a great variety of aspects [83-100,115]. First, the polarization diversity scheme was employed to suppress the polarization-dependent BGS fluctuations and thus to enhance the stability of the measurement [83]. A simultaneous use of Brillouin gain and loss was then demonstrated to improve the SNR [115]. Apodization based on intensity modulation was also implemented to enhance the dynamic range [84, 85]. Then, a low-coherence BOCDA system was proposed to resolve the trade-off between the spatial resolution and the measurement range [86,87]. The temporal gating scheme was also developed to mitigate this trade-off [88, 89]. Furthermore, extremely high nominal resolutions up to 1.6 mm were achieved using a single-sideband modulator (SSBM) instead of an EOM based on the double-lock-in scheme [90] and the beat-lock-in scheme [91]. To reduce the cost, a simplified BOCDA (S-BOCDA) system, in which an SSBM is not used, was implemented [92]. As for the sampling rate, it was enhanced to 1 kHz by employing an unbalanced Mach-Zehnder delay line to the S-BOCDA [93]. A discriminative measurement of strain and temperature has also been performed by Zou *et al.* [94, 95] with BOCDA using a novel acoustic dynamic grating. Finally, a quasi-one-end-access BOCDA system called “in-line BOCDA” was developed, with a mirror located at one end of the FUT [96]. Recently, many experiments from practical application standpoints have also been performed with fruitful results, such as health monitoring of aircraft and tunnels [97-100].

Thus, BOCDA is a powerful distributed sensing technology with an extremely high spatial resolution (cm- or mm-order) and a high sampling rate (~ 1 kHz). However, if part of the FUT cracks, the measurement can no longer be performed because two lightwaves must be injected into both ends of the FUT. In 2008, to resolve this problem of BOCDA, a novel sensing technology named Brillouin optical correlation-domain reflectometry (BOCDR) was proposed, which can measure the distribution of strain and/or temperature along an FUT by light injection only from one end of the fiber. BOCDR operates based on the combination of spontaneous Brillouin scattering and the correlation control of continuous lightwaves.

The conceptual schematic of the proposed BOCDR system is shown in Fig. 1.8 [116].

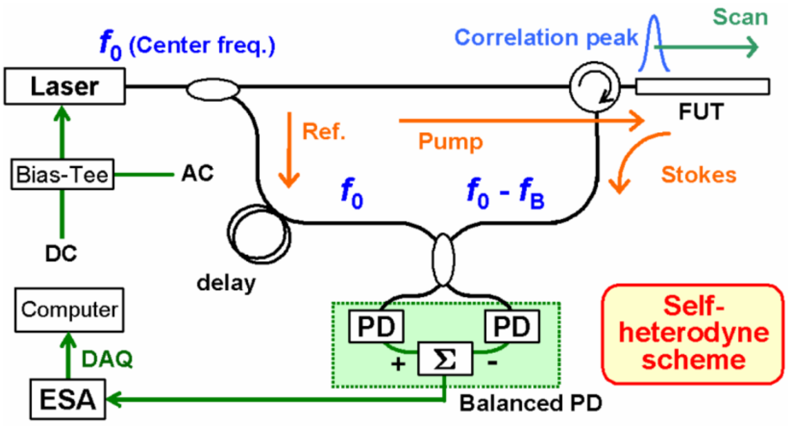

Figure 1.8 Conceptual schematic of BOCDR system [116].

A light beam from a laser is divided into pump and reference light beams. The pump light is injected into the FUT, and the Stokes light is directed into a heterodyne receiver composed of two balanced PDs. The reference light is used as an optical local oscillator. The electrical beat signal of the two light beams is monitored by an electrical spectrum analyzer (ESA). Since there is, without any additional frequency shifters, a frequency difference of about 11 GHz between the Stokes light and the reference light, this configuration is called self-heterodyne scheme.

In order to resolve the position in the FUT, the optical frequency of the light beam from the laser is directly modulated in a sinusoidal wave by modulating the injection current to the laser. From the viewpoint of time averaging, the correlation (or coherence) function is synthesized into a series of periodical peaks [18,102], whose period is inversely proportional to the frequency of the sinusoidal modulation fm. We control f_m to leave only one correlation peak within the range of the FUT, so that only the Brillouin scattering generated at the position correspondent to the peak has high correlation with the reference light, and then gives high heterodyne output. The peak frequency observed in the ESA gives the BFS caused at the position. By sweeping f_m, the correlation peak is scanned along the FUT to obtain the distribution of BGS or BFS. The spatial resolution Δz and the measurement range d_m (distance between the neighboring correlation peaks) of BOCDR are given by the same equations as those for BOCDA [79]. Then, the spatial resolution of BOCDR is given well by the same expression as that of BOCDA [79].

Here, we discuss the limitations of the spatial resolution and sensing points. Considering that f_m higher than $\Delta\nu_B$ does not contribute to the enhancement of Δz [117], and that Δf is practically limited to a half of BFS (ν_B) of the fiber because of the Rayleigh noise [116,117], the limitation of the spatial resolution Δz_{min} is given by

$$\Delta z_{min} = \frac{c}{\pi n \nu_B}. \tag{1.15}$$

The number of effective sensing points N_R, which can be regarded as an evaluation parameter of the system, is given by the ratio of d_m to Δz, as

$$N_R = \frac{d_m}{\Delta z} = \frac{\pi \Delta f}{\Delta \nu_B}. \tag{1.16}$$

To obtain higher N_R, Δf needs to be raised but it should be lower than $\nu_B/2$; N_R is thus limited to

$$N_{Rmax} = \frac{\pi \nu_B}{2\Delta \nu_B}. \tag{1.17}$$

In the first experiment by using the BOCDR, 40-cm spatial resolution has been experimentally demonstrated with 50-Hz sampling rate and 100-m-long FUT [116]. In 2009, a spatial resolution of 13 mm was experimentally demonstrated with a sampling rate of 50 Hz and 5-m-long FUT [118]. By use of a tellurite fiber, the spatial resolution has been enhanced up to approximately 6 mm [119]. In terms of enlargement of the measurement range, 27-cm resolution and 1.5-km measurement range have been achieved [120,121].

1. 4 Polymer/plastic optical fibers (POFs)

To date, glass optical fibers have been mainly used to develop Brillouin fiber sensors, which cannot, however, measure large strain of < 10%. One method for overcoming this problem is to implement such Brillouin sensors using POFs. They offer easy connection, high safety, and high flexibility with which they can withstand strain of > 50%. Therefore, our purpose is to implement distributed temperature and strain sensors based on Brillouin scattering in POFs. In this Section, we review the birth, physical properties, and Brillouin scattering in POFs.

1. 4. 1 Properties of POFs

The first prototype of POFs was developed by “Dupont” in U.S.A. in 1960 [122]. In 1975, the first product of POFs named “Eska” was commercialized by “Mitsubishi Rayon” in Japan. However, POFs had a serious problem that their propagation loss is extremely high (440 dB/km at 650 nm). In 1990, Keio University succeeded in improving the loss by inducing graded-index structure into the core of POFs and low loss (180 dB/km) was achieved. In 2000, the loss was improved even to 40 dB/km by the same group, using perfluorinated polymer as core materials [123].

POFs have attracted considerable attention for the past several decades due to their extremely easy and cost-effective connection [124, 125], high safety, and high flexibility [126] compared to conventional glass fibers. Owing to their propagation loss higher than that of silica glass fibers, POFs have been made use of in medium-range communication applications such as home networks and automobiles [127] as well as in high-strain monitoring applications [126,128]. In addition, a so-called "memory effect" [126] has been proposed as their new advantage. Commercially-available POFs are classified into two types: poly(methyl methacrylate) (PMMA)-based POFs and perfluorinated graded-index (PFGI-) POFs, the physical properties of which are described in 1.4.1.1 and 1.4.1.2.

1. 4. 1. 1 Poly(methyl methacrylate) Based (PMMA-) POFs

After explaining the physical characteristics of PMMA-POFs, we mention the difficulty in measuring Brillouin scattering in PMMA-POFs.

One of the commercially-available PMMA-POFs is composed of PMMA (Plexiglass®), which is an organic compound based on a polymerized material with an amorphous structure and glass transition temperature (Tg) close to 100 °C. The PMMA comprises several methyl (methacrylate) (MMA) monomers, as shown in Fig. 1.9 [129]. The PMMA-POFs have high propagation loss (200 dB/km at 650 nm) [124].

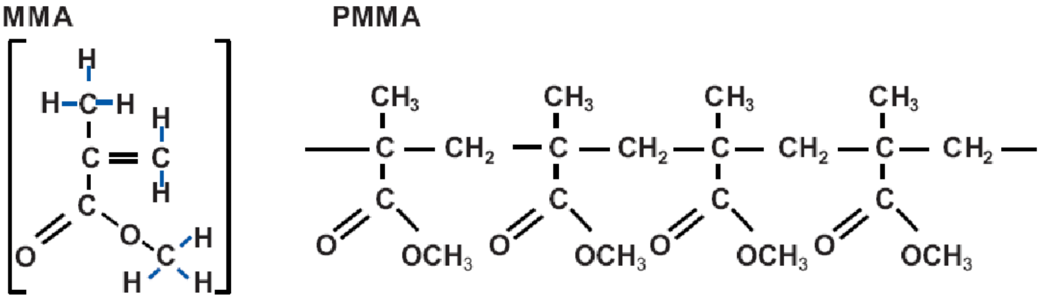

Fig. 1.9 Molecular geometry and bonding of the Plexiglass® [129].

The PMMA-POFs are cost-effective and widely used in communication applications, and so the observation of Brillouin scattering in PMMA-POFs is important for predicting the performance as sensors but difficult for the following two reasons: (1) the Brillouin signal is extremely small due to their large core diameter (typically 980 μm), and (2) it is not easy to prepare all the optical devices operating at ~650 nm, where the propagation loss of PMMA-POFs becomes lowest.

1. 4. 1. 2 Perfluorinated graded-index (PFGI-) POFs

One of the commercially-available PFGI-POFs is composed of cyclic transparent optical polymer (CYTOP®), which is an amorphous fluoropolymer with *T*g close to 108°C. The CYTOP® comprises only C-F bonds as shown in Fig. 1.10 [129]. Thus the PFGI-POFs have lower propagation loss (15 dB/km at 1300 nm) [124] than that of the PMMA-POFs.

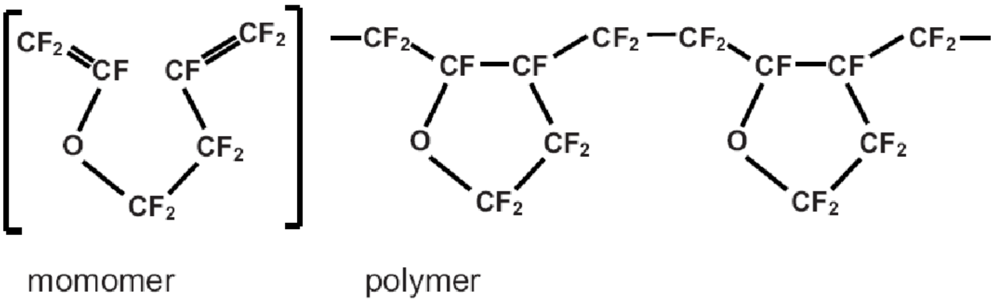

Fig. 1.10 Molecular geometry and bonding of the Plexiglas® [129].

Since not only visible light but also telecom wavelength light at up to 1550 nm can be transmitted though the PFGI-POFs, the relatively inexpensive optical devices operating at ~1550 nm can be used to observe their Brillouin scattering signal.

1. 4. 2 Optical fiber sensors using POFs

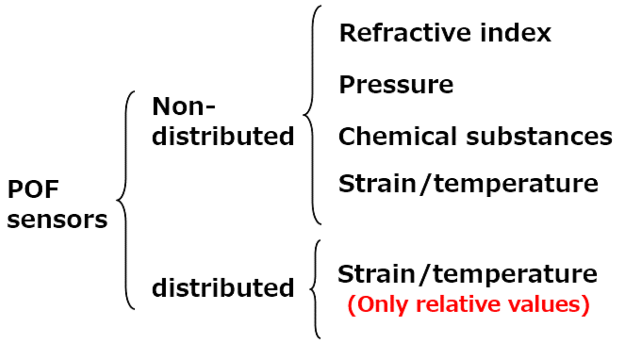

Fig. 1.11 Classification of optical fiber sensors using POFs.

Sensing applications using POFs are classified into two types: non-distributed and distributed sensing, as shown in Fig. 1.11. Non-distributed sensors have been used to measure a variety of physical parameters including refractive index [130], pressure [131], chemical concentration (or substance itself) [132-134]. Strain and temperature have been also measured by non-distributed sensors based either on fiber Bragg gratings [135] or on modal interference [136]. In the meantime, strain and temperature have been mainly measured using distributed sensors [126, 137]. These distributed sensors, however, were not capable of measuring the absolute values of strain and temperature.

1. 4. 3 Brillouin scattering in POFs

Many theoretical studies on Brillouin scattering in POFs had been reported [138,139], and thus its significance and usefulness had been recognized by a number of researchers. Nevertheless, no one had succeeded in experimentally observing Brillouin scattering in

POFs. However, the scattering has not been observed experimentally because there are three reasons as follows; namely, (1) since the core diameter of the POFs is ~100 times larger than that of standard single-mode glass fibers, the power density becomes much lower in POFs, which drastically reduces the efficiency of Brillouin scattering (= one of the nonlinear phenomena), (2) at the visible wavelength, where the propagation loss of standard POFs becomes minimal, some of the optical devices (circulator, amplifier, etc.) required to perform the Brillouin experiment do not exist (or are too expensive). To tackle these difficulties, Y. Mizuno *et al*. (1) employed graded-index POFs in which lightwave is concentrated at the core center, (2) employed perfluorinated POFs with relatively low propagation loss even at telecom wavelength, and also implemented an original experimental setup fully exploiting self-heterodyne detection as depicted in Fig. 1.12.

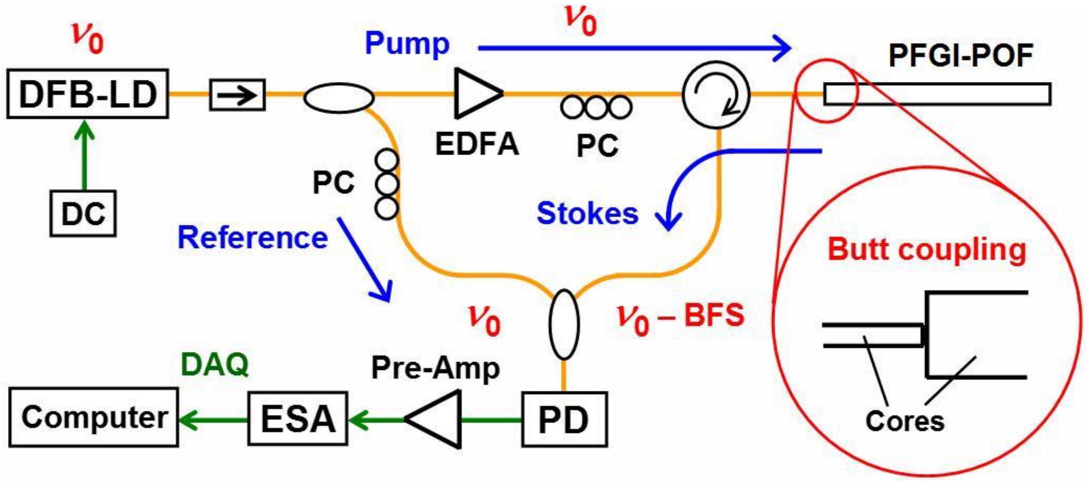

Fig. 1.12 Experimental setup based on original self-heterodyne detection [148].

After making these efforts, in 2010, Mizuno *et al*. finally succeeded in observing Brillouin scattering in POFs for the first time in the world [132], as shown in Fig. 1.13.

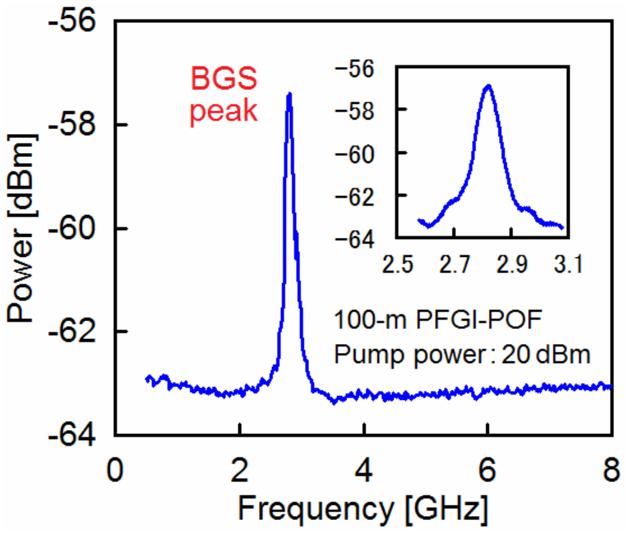

Fig. 1.13 Brillouin signals in a POF measured for the first time in the world [132].

In this observation, significant values of the scattering were clarified that the BFS of PFGI-POFs was measured 2.83 GHz, and the Brillouin gain coefficient was estimated to be 3.09×10^{-11} m/W, which was almost the same as that of a silica SMF. This success set the stage for other significant steps forward as follows:

[1] Clarification of Fundamental Properties

(1) BFS dependences on strain and temperature in POFs [141]; they showed negative dependences with coefficients of −121.8 MHz/% and −4.09 MHz/K, respectively, which are −0.2 and −3.5 times as large as those in silica fibers. These unique BFS dependences indicate that the Brillouin scattering in PFGI-POFs has a big potential for highly sensitive temperature sensing with strain insensitivity.

(2) Fresnel reflection (FR) properties at the ends of POFs [142]; the FR spectra at the ends of a step-index (SI-) multimode fiber (MMF) and a graded-index (GI-) MMF were investigated with heterodyne detection, and compared with that of a SMF. The FR spectra of the MMFs were found to spread broader than that of the SMF, and the

FR spectrum of the SI-MMF was even broader than that of the GI-MMF. It was also demonstrated that the observation of the BGS in a POF is severely influenced by the FR spectrum. This information will be a useful guideline for the design of robust Brillouin sensing systems using MMFs including POFs.

(3) Influence of core diameter and fiber length on Brillouin spectra in POFs [143]; the BGS properties of PFGI-POFs with 62.5-m core diameter were investigated. The Stokes power was extremely high compared to that of a PFGI-POF with 120-μm core, and the Brillouin threshold power for 5-m PFGI-POF was estimated to be 53.3 W. It was also shown that employing a PFGI-POF longer than m is not an effective way to enhance the Stokes signal. In addition, it was theoretically found that it is difficult to reduce the Brillouin threshold power of PFGI-POFs at 1.55-μm wavelength below that of long silica SMFs even if their core diameter is sufficiently decreased to satisfy the single-mode condition. Finally, the Brillouin linewidth narrowing effect was confirmed.

(4) Influence of fiber fabrication method on Brillouin spectra in POFs [144]; the BGS in three PFGI-POFs fabricated by different manufacturers at 1.32 and 1.55 μm was investigated. For all the PFGI-POFs, the Stokes power measured at 1.32 μm was higher than that at 1.55 μm due to the lower propagation loss, but striking difference in Stokes power was observed among the three. Then the optical time-domain reflectometry measurement was performed to clarify the reason for the difference, and it was showed that the actual propagation loss of the PFGI-POFs plays an extremely important role in BGS observation.

[2] Signal Improvement for Sensing Applications

(1) Induction of stimulated Brillouin scattering with pump-probe technique [145]; SBS in a PFGI-POF with 120-μm core diameter was experimentally observed for the first time, to the best of our knowledge, at 1.55 μm wavelength with the pump-probe technique. Compared to spontaneous Brillouin scattering previously reported, the BGS was detected with an extremely high signal-to-noise ratio, even with a short POF (1 m) and scrambled polarization state. The BGS dependences on probe power and temperature were also investigated.

(2) Enhancement of Brillouin signal using pulsed optical pump [146]; a new scheme for enhancing Brillouin Stokes power was developed, which exploits pulsed pump light and a low-power erbium-doped fiber amplifier. First, it was theoretically shown that, even when the pulsed pump light has low average power, the temporally averaged Stokes power can be enhanced if its peak power is higher than the Brillouin threshold power. Then, in the experiment, when a pulsed pump light with an average power of 20 mW, a duty ratio of 20%, and a pulse period of 2 μs was injected into a silica SMF, the Stokes power was enhanced by 25 dB relative to that with continuous-wave pump light having the same average power. This method will provide a useful and cost-effective way of characterizing the Brillouin scattering properties in POFs, such as BFS and its dependence on strain, temperature, moisture, and core materials.

(3) Improvement of coupling efficiency at POF/SMF boundary [147]; a simple, efficient, and cost-effective method to enhance a Brillouin scattering signal in PFGI-POFs was proposed and demonstrated. In this method, instead of the conventional butt-coupling of a POF to a SMF, a MMF with a proper mode-field diameter of the fundamental mode is additionally inserted between the two fibers to improve the optical coupling efficiency from the POF to the SMF. After theoretical analysis, it is experimentally shown that the Brillouin signal in the POF is clearly enhanced simply by inserting standard MMFs, which are commercially available at affordable cost.

(4) Method for efficient butt-coupling of different-type optical fibers [148]; by monitoring and maximizing the power of the Brillouin-scattered light, highly efficient butt coupling between an SMF and GI-MMFs was clarified to be easily achievable. The usefulness of this method was confirmed by the experimental results with three different GI-MMFs. Then, it was found that the BFS also depends on the relative core position due to the excitation of many higher order modes. This Brillouin-based core alignment method will greatly help GI-MMFs including GI-POFs to be utilized as sensing heads in fiber-optic sensing systems.

(5) Fresnel-assisted self-heterodyne detection [149]; it was experimentally shown that by utilizing the Fresnel-reflected light as the reference light, Brillouin signals in POFs can be observed with a higher SNR than those measured with standard self-heterodyne detection. This method was basically the same in setup as direct detection, leading to an additional advantage of system simplicity. Moreover, it was demonstrated that the Brillouin signal in a 1 cm-long POF can be observed with a moderate SNR using this technique, indicating a potential feasibility of POF-based distributed Brillouin measurement with millimeter-order spatial resolution.

(6) Fiber-optic interferometry: influence on Brillouin measurement [150]; an interference pattern was observed using a simple fiber-optic interferometer consisting of an ESA and a narrowband light source, which was commonly employed for observing the Brillouin gain spectrum. This interference pattern expanded well beyond the frequency range corresponding to the Brillouin frequency shift in silica fibers. Using both silica SMFs and POFs, we then experimentally proved that the distinctive noise in a self-heterodyne-based Brillouin measurement with an unoptimized polarization state originates from the interference between the reference light and the Fresnel-reflected light. This noise can be almost completely suppressed by employing a delay line that is longer than the coherence length of the light source and by artificially applying a high loss near the open end of the sensing fiber.

Thus, towards the first demonstration of distributed strain and temperature sensing based on Brillouin scattering in POFs, steady and innovative progress have been made from the viewpoints of clarification of fundamental properties and development of novel methods for signal improvement. However, in order to achieve the goal, further research is required.

1. 5 Performance estimation of POF-based Brillouin sensors

In this Section, before presenting the purpose and the constitution of this dissertation, we theoretically estimate the ultimate performance of POF-based Brillouin sensors, such as sensitivity, dynamic range, measurement range, and spatial resolution.

The strain and temperature sensitivities, i.e., their dependence coefficients of the BFS, can be theoretically calculated by differentiating Equation (1) with respect to strain and temperature [151]. Then we know that these coefficients are dependent on the changes in Young's modulus, refractive index, and Poisson's ratio caused by strain and temperature change. Among the three parameters, the change in Young's modulus is reported to have the largest contribution. The theoretical strain coefficient of the BFS in standard PMMA-based POFs is calculated to be −160.6 MHz/%, which is ~0.3 times larger than that in silica SMFs [151]. As is easily guessed, this difference originates from the difference of the strain dependence of Young's modulus [151]. In the same way, the temperature coefficient is calculated to be −6.72 MHz/K, which is ~6 times larger than that in silica SMFs [151]. This difference also originates from the difference of the Young's modulus dependence on temperature [151]. Thus, it is expected that, in POFs, the temperature sensitivity is much higher while the strain sensitivity is much lower than those in silica SMFs.

Next, the dynamic range of strain can be estimated as follows: first, by clarifying the fracture strain and the elastic-to-plastic transition in PMMA-POFs using the stress-strain curve, and then, by investigating the BFS dependence on large strain of ≥1% using the measured acoustic velocity in PMMA-POFs. As will be detailed in Section 2 in Chapter 4, by measuring the stress-strain curve, we find that the elastic-to-plastic transition occurs at 2% strain and that the fracture strain is 55%. We also find the estimated BFS dependence on large strain is non-monotonic in the plastic region, which leads to the fact that to discriminate the strains of > 2% and < 2% is difficult, if only the BFS dependence on large stain is used. In this sense, the dynamic strain range will be less than 2%. We believe, however, that this limitation will be further enhanced by exploiting other physical parameters, such as the Stokes power and Brillouin bandwidth.

The limitation of the measurement range is also discussed, which is highly related to the effective length of the FUT. The effective length of the PFGI-POF is calculated to be ~18 m at 1.55-μm wavelength by substituting a sufficiently long FUT length to the Equation (1.4), and so the measurement range will be limited to several tens of meters. This value will be elongated by using shorter optical wavelength at which the propagation loss is lower. For instance, by employing the light at 0.98 μm (the effective length can be up to ~400 m), the limitation will be enhanced to several hundreds of meters.

Finally, we discuss the spatial resolution, which depends on distributed sensing techniques. Here, we assume BOCDR, which we believe the most suitable for POF-based distributed sensing, as detailed in Section 1 in Chapter 3. Using Equation (1.15), the theoretical limitation of the spatial resolution of POF-based BOCDR is calculated to be 23 mm. This value is about a quarter of that of silica-based BOCDR, which is mainly caused by the difference in BFS. In terms of the practical applications, this resolution is sufficiently high because the sensing heads of Brillouin sensors are generally fixed to some structures with 0.5–1.0 m intervals. We should note that the resolution is in the trade-off relation with the measurement range. More detailed discussion will be found in Section 1 in Chapter 3.

1. 6 Purpose and constitution of this dissertation

The major purpose of this dissertation is to develop POF-based distributed strain and temperature sensors. This dissertation consists of the following five chapters: “1. Introduction,” “2. Brillouin properties in large-strain applied POFs,” “3. Distributed strain and temperature sensing using POFs,” “4. Relevant work for performance improvement of POF-based Brillouin sensors,” “5. Conclusions.”

In Chapter 2, we clarify the BGS dependence on large strain (< 20%) in POFs, and observe unique phenomenon named BFS hopping. In Chapter 3, we demonstrate the distributed sensing using POFs, and simplify its experimental setup. In Chapter 4, we perform the following six experiments to improve the performance of the POF-based distributed sensors: (i) clarification of the SBS properties in POFs for SNR enhancement, (ii) estimation of the Brillouin properties in PMMA-POFs toward higher-sensitivity temperature sensing, (iii) fast flaw detection in POFs using infrared thermometry for efficient selection of high-quality POFs to be used as sensor heads, (iv) observation of BGS in tapered POFs toward implementation of a memory function regarding temperature, and (v) observation of a fiber fuse phenomenon in POFs toward understanding of the performance limitation of POF-based Brillouin sensors. Finally, in Chapter 5, we present our concluding remarks of this dissertation and describe remaining problems and outlook for the future.

2 Brillouin properties in large-strain applied POFs

In this chapter, first, we measure a stress-strain curve of a plastic/polymer optical fiber (POF), and investigate the Brillouin gain spectrum (BGS) dependence on large strain of < 60%. We then observe and clarify a unique phenomenon named Brillouin frequency shift (BFS) hopping in POFs.

2. 1 Brillouin gain spectrum (BGS) dependence on large strain

In this Section, first, we obtain a stress-strain curve of a perfluorinated graded-index (PFGI-) POF, and show that the elastic-to-plastic transition occurs at approximetely10% strain. Then we investigate the dependence of Brillouin gain spectra (BGSs) on large strain of > 20% in the PFGI-POF, and prove, for the first time, that the dependence of BFS is highly non-monotonic. We predict that temperature sensors even with zero strain sensitivity can be performed by use of this non-monotonic nature. Meanwhile, the Stokes power decreases rapidly when the applied strain is > approximetely10%. This behavior seems to originate from the propagation loss dependence on large strain. By exploiting the Stokes power dependence, we can most likely solve the problem of how to identify the applied strain, when the identification is difficult merely by BFS because of its non-monotonic nature.

2. 1. 1 Introduction

Brillouin scattering in PFGI-POFs has already been experimentally observed, since various optical devices are available at telecom wavelength [140]. The BFS dependence on strain in PFGI-POFs has been measured to be linear with a coefficient of −121.8 MHz/%, but, in our previous experiment, the applied strain ranged merely from 0% to 0.8% [141]. Putting their memory effect in perspective, the BFS dependence on large strain in PFGI-POFs needs to be clarified.

In this Section, we experimentally investigate the dependence of BGS on large strain of up to 20% in a PFGI-POF. The BFS dependence is found to be non-monotonic, which agrees with our prediction concerning PMMA-POFs in Chap. 4, Section 2. By exploiting this non-monotonic nature, temperature sensing even with zero strain sensitivity will be feasible. As for the Stokes power, it is found to decrease drastically when the applied strain is larger than 10%. We show that this behavior is well explained by the propagation loss dependence on large strain. Utilizing the Stokes power dependence is one way to solve the problem of how we should identify the applied strain, when it is difficult merely by BFS due to its non-monotonic nature.

2. 1. 2 Experimental setup

We employed a 1.27-m-long PFGI-POF as a fiber under test (FUT), which had numerical aperture (NA) of 0.185, core/cladding diameter of 50 μm, cladding diameter of 100 μm, over cladding diameter of 750 μm, core refractive index of approximetely1.35, and propagation loss of approximetely250 dB/km at 1.55 μm. The experimental setup for investigating the BFS dependence on large strain in the PFGI-POF was basically the same as that previously reported in [140], where the BGS can be observed with a high resolution (3 MHz in this experiment) by self-heterodyne detection. One end of the PFGI-POF was butt-coupled to a silica SMF via an SC connector, and the other end was guided to an optical power-meter. Polarization state was adjusted for each measurement with polarization controllers so that the Stokes power may be maximal. Different strains of up to 20% were applied to the whole length of the PFGI-POF fixed on two translation stages. The temperature was kept at 27°C for all the measurements.

2. 1. 3 Experimental results

Fig. 2.1.1 shows a stress-strain curve of a 0.1-m PFGI-POF of the identical type, which was obtained with the same method (strain-applying speed: 100 mm/min) as in Chap. 4, Section 2. The cross-sectional area was assumed to be constant during the measurement. Fracture strain of the PFGI-POF was 71% and its elastic-plastic transition was apparently induced at several % strain [152]. The initial peak up to approximately 10% indicates the elastic-to-plastic transition [153].

The measured BGS dependence on large strain of up to 18.3% in the PFGI-POF is shown in Fig. 2.1.2(a). It took tens of seconds to manually apply a specific strain to the PFGI-POF; then, a few minutes later, the BGS measurement was performed.

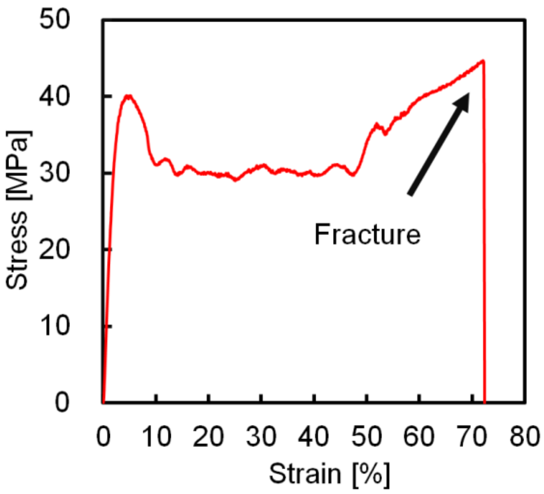

Fig. 2.1.1 Measured stress-strain curve of the PFGI-POF.

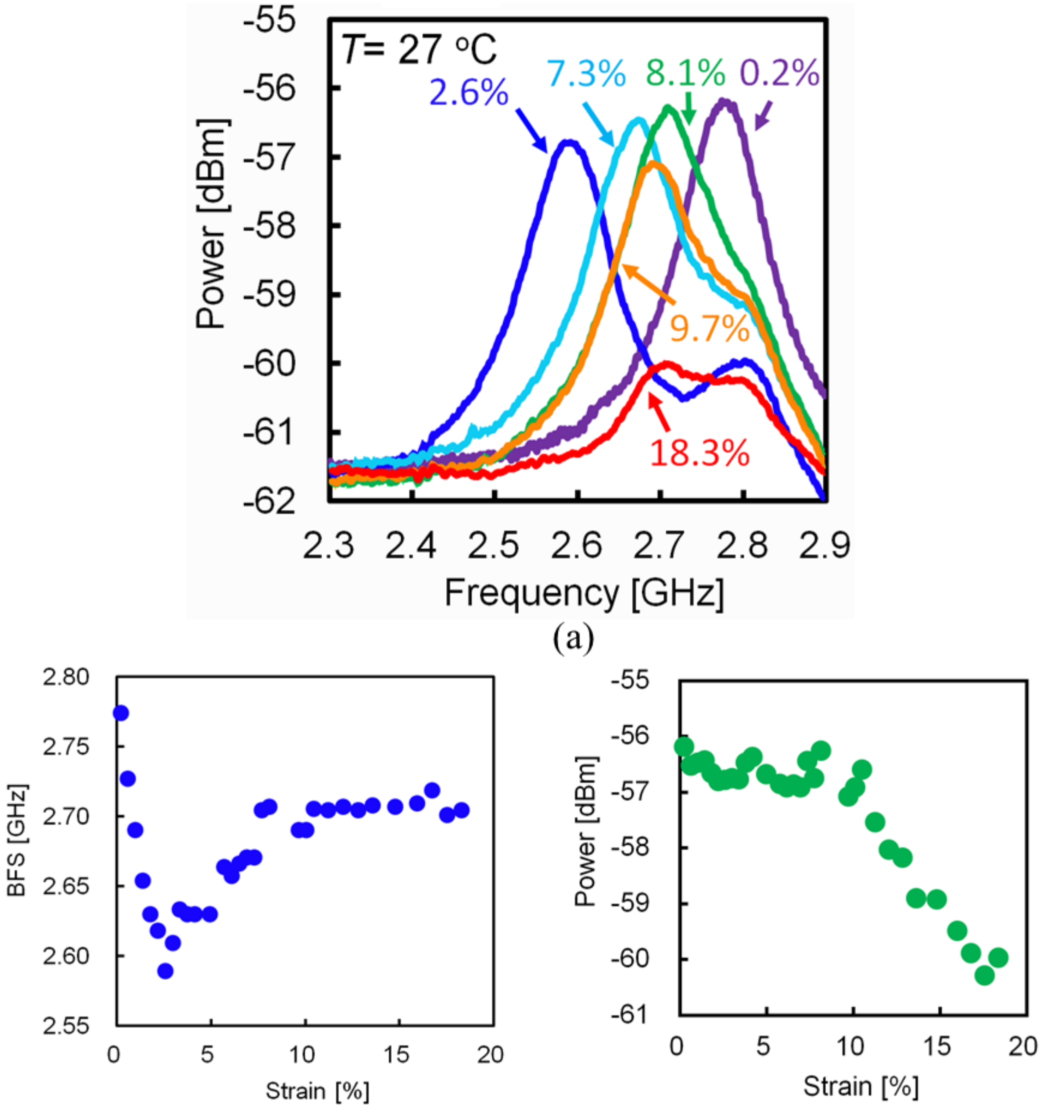

(a)

(b) (c)

Fig. 2.1.2 Measured large-strain dependences of (a) the BGS, (b) the BFS, and (c) the Stokes power in the PFGI-POF.

When the strain was 2.6%, a small peak was clearly observed at approximately 2.8 GHz. This peak was caused by a 6-cm portion of the PFGI-POF end connected to the silica SMF, to which proper strain was not applicable. From this measurement, the dependences of the BFS and the Stokes power on large strain can be plotted as shown in Figs. 2.1.2(b) and (c), respectively. In Fig. 2.1.2(b), the BFS dependence on strain was non-monotonic; with the increasing strain, the BFS shifted at first toward lower frequency (0-2.6%) (this shift agrees well with the result under small strain [141]), then toward higher frequency

(2.6-8.1%), and finally became almost constant (8.1-18.3%). This behavior may be caused by the Young's modulus dependence on large strain [141]. In Fig. 2.1.2(c), with the increasing strain, the Stokes power decreased, and its reduction grew drastic when the strain was over approximately 10%. At approximately 20% strain, the Stokes power became so low that the target BGS was buried by the noise, i.e., by the BGS of the small portion of the PFGI-POF without strain applied. The fluctuations in the Stokes power were caused by the unstable polarization state. The dependence of the Brillouin linewidth on large strain is also a significant property, but we did not evaluate it because the Stokes power was so small that its fair measurement was not feasible. The repeatability of the results above has been confirmed by performing the same measurements for other samples.

To clarify the origin of the Stokes power dependence on strain given in Fig. 2.1.2(c), the propagation loss was also measured as a function of strain as shown in Fig. 2.1.3(a). The loss drastically increased when the strain was over approximately 10%. Then, based on this figure, the strain dependence of the effective length was calculated using Eq. (1.4), which is given in Fig. 2.1.3(b). With the increasing strain, the effective length started to decrease drastically when the strain was over approximately 10%, which is in good agreement with the Stokes power dependence. In Fig. 2.1.3(b), when the strain was smaller than 5%, the effective length was slightly increased with the strain, because the actual fiber length was elongated owing to the strain and it compensated for the increase in the loss. This behavior is different from that in the Stokes power dependence in Fig. 2.1.2(c), but it is valid if we consider that the small peak at approximately 2.8 GHz caused by the small portion of the PFGI-POF was overlapped with the target BGS at such small strains. Thus, we presume that the reduction of the Stokes power in the PFGI-POF with strain is attributed to that of the propagation loss.

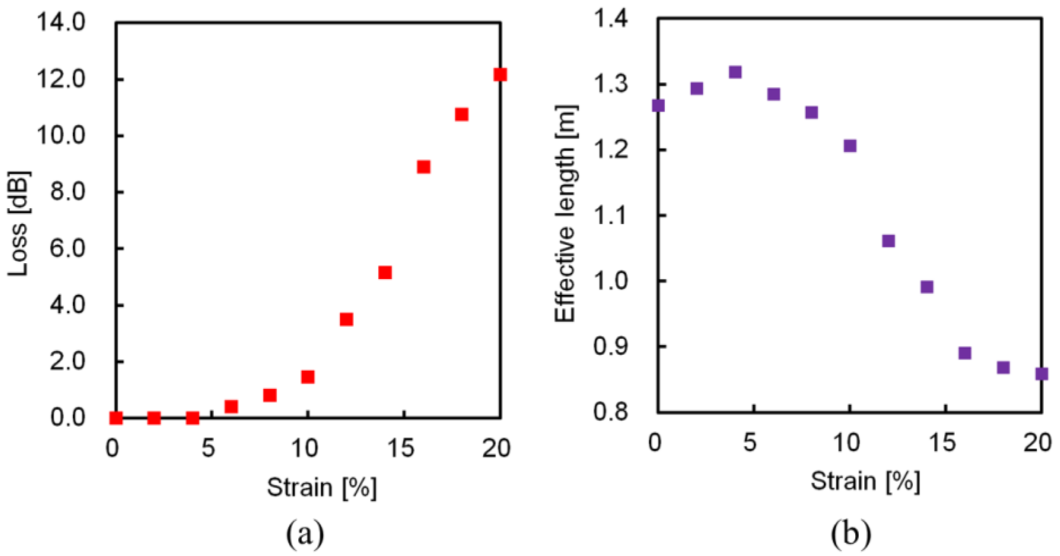

Fig. 2.1.3 Measured large-strain dependences of (a) the propagation loss and (b) the effective length in the PFGI-POF.

By exploiting these unique Brillouin features of PFGI-POFs, some useful devices and systems will be developed. For instance, the BFS in a PFGI-POF to which 10-15% strain is applied has no strain dependence, and consequently it may be used for temperature sensing with almost zero strain sensitivity. We must note that, due to the non-monotonic nature of BFS, the identification of the applied large strain is sometimes difficult only by BFS. We may solve this problem by applying approximately 2.6% strain beforehand and/or by using the Stokes power dependence on strain as well.

2. 1. 4 Conclusion

By applying large strain of up to 20%, the strain dependence of BGS in the PFGI-POF was measured in detail. The BFS exhibited a non-monotonic nature, with which temperature sensing even with zero strain sensitivity will be feasible. The Stokes power drastically dropped when the applied strain was larger than approximetely 10%. This behavior is probably caused by the large-strain dependence of the propagation loss. The identification of the applied strain is sometimes difficult only by BFS due to its non-monotonic nature; in that case, using the Stokes power dependence will be one of the solutions. Since this nature may vary depending on the time of applying strain or the types of the POFs (PMMA-POFs, partially-chlorinated POF, etc.), further investigation is required on this point. We believe that these results are of great significance in developing large-strain sensors based on Brillouin scattering in POFs.

2. 2 Observation of Brillouin frequency shift hopping

From this Section, we investigated the BGS dependence on large strain of up to 60 % in a POF at 1.55 μm, and found that the BFS abruptly changes from approximetely2.7 GHz to approximetely3.2 GHz. We named this phenomenon “BFS hopping,” and found it to originate from the varied acoustic velocity induced by the stepwise change in the core diameter of the POF. This is because of the yielding of the overcladding layer composed of polycarbonate. We also discuss the use of the Stokes power ratio (defined as the ratio of the Stokes power of the new peak to that of the initial peak) to determine the large strain applied to the POF. After the occurrence of BFS hopping phenomenon, the BFS dependence coefficients on strain and temperature in the POF were measured to be −65.6 MHz/% and −4.04 MHz/K respectively. These values indicate that, compared to an unstrained POF, further higher-precision temperature sensing with lower strain sensitivity is feasible.

2. 2. 1 Introduction

We have recently measured the BGS dependence on large strain of up to 20% (see Chap. 2, Section 1), and found that at approximately 10% strain the Brillouin Stokes power starts to decrease. We attributed the reason for this behavior to an increased propagation loss leading to a shortened effective length (see Chap. 2, Section 1). However, the drastic decrease (approximetely60%) in the Stokes power at 20% strain is not fully explained by only approximetely30% reduction of the effective length.

From this Section, we investigate the BGS dependence on even larger strain of up to 60% in a PFGI-POF at 1.55 μm, and find that the BFS abruptly changes from approximately 2.7 GHz to approximately 3.2 GHz. This provides a reasonable explanation for the phenomenon described above. We name this "BFS hopping," the origin of which is shown to be the varied acoustic velocity induced by the stepwise change in the core diameter. We also discuss the use of the Stokes power ratio (defined as the ratio of the Stokes power of the new peak to that of the initial peak) to determine the large strain applied to the POF. Further, from our measurements we found the strain- and temperature-dependence coefficients of the BFS in the slimmed-down POF (after the BFS hopping) to be −65.6 MHz/% and −4.04 MHz/K respectively, indicating that with lower strain sensitivity, higher-precision temperature sensing can be achieved.

2. 2. 2 Experimental setup

We employed a 0.6-m-long PFGI-POF with 50 μm core diameter. The core and cladding layers are composed of doped and undoped polyperfluorobutenylvinyl ether (trademark: CYTOP). The refractive index at the center of the core, the numerical aperture, and the propagation loss at 1.55 μm are 1.356, 0.185, and approximately 250 dB/km respectively. The polycarbonate reinforcement overcladding layer (diameter of 490 μm) reduces micro-bending losses and increases the load-bearing capability. Instead of the standard experimental setup based on self-heterodyne detection [140], we used a newly developed Fresnel-assisted setup [154], which can detect the BGS in POFs with a higher signal-to-noise ratio. Large strain was applied to the POF with two computer-controlled motorized stages at a room temperature of 20°C.

2. 2. 3 Experimental results

First, we measured the BGS dependence on large strain of up to 60% in the POF, as shown in Fig. 2.2.1(a). The pump power was 26 dBm, and the strain rate was 200 µm/s. The Brillouin peak observed at approximetely 2.8 GHz in the absence of strain shifted to lower frequency at < 2.3% strain, and then shifted to a higher frequency; its peak power gradually reduced with increasing strain (> 10%). This behavior has been reported earlier in Ref. [155]. However, we first report the appearance of an additional peak at approximetely3.2 GHz when strain was > 7.3% (Fig. 2.2.1(a). At 31% strain, the power of the two peaks is almost the same, and at 60% strain, the initial peak almost disappeared (note that the peak at approximetely 2.85 GHz originated from the approximetely3-cm-long unstrained POF section near the connector). The BFS of the two peaks were then plotted as functions of strain, as shown in Fig. 2.2.1(b). The dependence of the initial peak

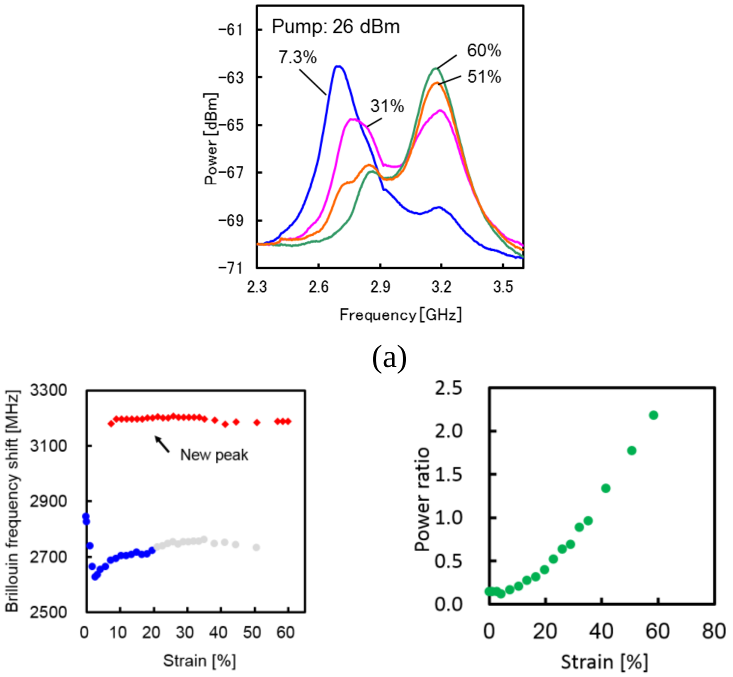

(a)

(b) (c)

Fig. 2.2.1. Measured large-strain dependence of (a) BGS, (b) BFS, and (c) Stokes power ratio in POF. In (b), the BFS of the initial peak was not accurately measured at strain of > 20 % (colored in gray).

showed the same non-monotonic behavior as previously reported [155] (> 20%, the BFS cannot be accurately measured). The BFS of the newly appeared peak was almost independent of the applied strain in this range. The strain dependence of the Stokes power ratio (defined as the ratio of the Stokes power of the new peak to that of the initial peak) can be plotted as shown in Fig. 2.2.1(c). The power ratio drastically increased when the strain was over approximately 3%. The strain at which the power ratio can be plotted was limited to approximately 60%, because the whole length of the strained section is slimmed at approximately 60%. The fluctuations in the power ratio were caused by the unstable polarization state. We speculate that large-strain sensing (< 60%) will be feasible by using this behavior, i.e., strain of up to ~10% can be determined using the BFS values (by applying 3% strain to the POF in advance), whereas strain of over 10% can be determined using the power ratio.

Next, side views of the POF in the presence of ~7.3% strain are shown in Fig. 2.2.2(a). Several sections were slimmed down in a stepwise manner, and with increasing strain, the slimmed sections grew longer (i.e., spread along the POF), while their outer diameter was maintained. This explains the independence of BFS from large strain (> 7.3%) described above. The core diameter of the slimmed-down POF was estimated to be 0.84 times of that of the unstrained POF from a cross-sectional view shown in Fig. 2.2.2(b). This phenomenon is probably caused by the yielding of the overcladding layer made up

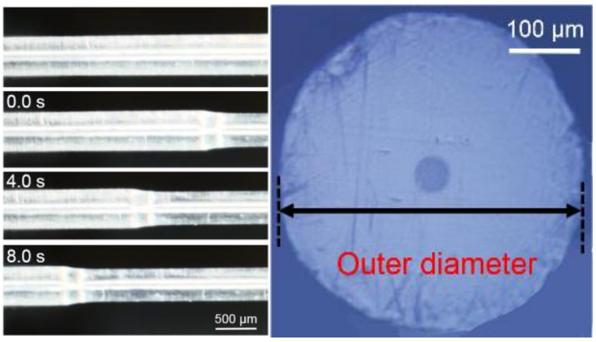

Fig. 2.2.2. (a) Side views of the slim-down process of the POF (taken every 4 s), and (b) cross-sectional view of the slimmed-down POF.

of polycarbonate, and not because of the core or cladding layers. The upper yield point of ~8.0% (see Fig. 6 in Ref. [156]) agrees with the strain at which the POF was slimmed down (according to the specification sheet, the upper yield point of CYTOP composing the core and cladding layers is approximately 20%). This abrupt change in the core diameter seems to have induced the change in the acoustic velocity, therefore resulting in the BFS hopping. Further, note that the unstable stress-strain curve of the PFGI-POF in the range from ~ 10 to 60% (see Fig. 2.2.1 in Ref. [155]) can also be explained by this phenomenon.

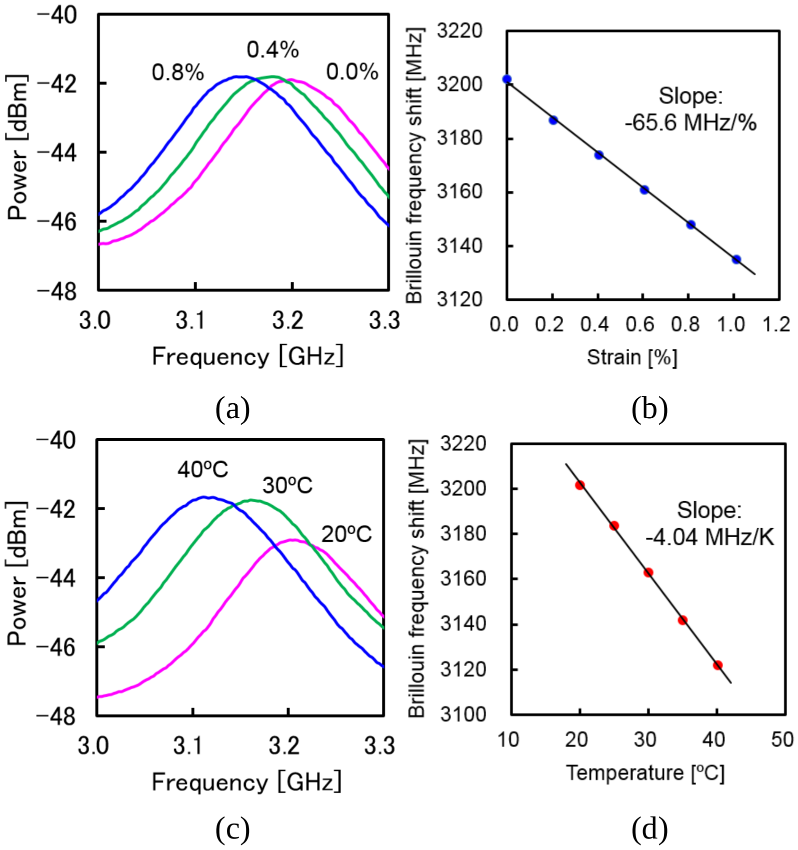

Fig. 2.2.3. Measured strain dependence of BGS (a) and BFS (b), and temperature dependence of BGS (c) and BFS (d) of the slimmed-down POF.

Finally, after the whole length of the POF was slimmed down at 60% strain, its BGS/BFS dependence on strain and temperature was investigated after the strain was released, and the results are shown in Figs. 2.2.3(a)–(d). Their BFS dependence coefficients were found to be −65.6 MHz/% and −4.04 MHz/K (Fig. 2.2.3(b) and (d)), which are 0.5 times [141] and 1.3 times [157] the value of an unstrained POF. This result indicates that further higher-precision temperature sensing with lower strain sensitivity is feasible by exploiting the Brillouin signals in the slimmed-down POFs.

2. 2. 4 Conclusion

The BGS dependence on large strain of up to 60% in a PFGI-POF was investigated at 1.55 µm, and an abrupt change in BFS from approximetely 2.7 GHz to approximetely 3.2 GHz was observed. We showed that this “BFS hopping” is probably caused by the varied acoustic velocity induced by the stepwise change in the core diameter (because of the yield of polycarbonate-based overcladding layer). We also discussed the use of the Stokes power ratio to determine the large strain applied to the POF. Subsequently, the strain- and temperature-dependence coefficients of the BFS in the slimmed-down POF were −65.6 MHz/% and −4.04 MHz/K respectively, which indicates the possibility of higher-precision temperature sensing with lower strain sensitivity. We believe that the physical aspects of these results are interesting and will be of great significance in developing POF-based large-strain sensing systems in the near future.

3 Distributed strain and temperature sensing using POFs

In this chapter, first we demonstrate distributed strain and temperature sensing using polymer/plastic optical fibers (POFs) based on correlation-domain technique. We then simplified the experimental setup.

3. 1 First demonstration based on correlation-domain technique

In this Section, we present the first demonstration of distributed strain/temperature sensing with a high spatial resolution in POFs based on Brillouin optical correlation-domain reflectometry. A 50-cm-long strain-applied (or heated) POF section is clearly detected with a theoretical spatial resolution of 34 cm, a high sampling rate of 3.3 Hz (per measured point), and a high signal-to-noise ratio. A 10-cm-long heated POF section is also successfully detected with a theoretical resolution of 7.4 cm. The performance limitation of this system is then discussed.

3. 1. 1 Introduction

Very recently, Minardo et al [158] have demonstrated low-resolution distributed temperature sensing in a POF based on Brillouin optical frequency-domain analysis (BOFDA). They detected a 4-m-long heated section—located at one end—of a 20-m-long POF, but the spatial resolution and signal-to-noise ratio (SNR) were not sufficiently high for practical use; relatively high cost of the devices such as a vector network analyzer and a microwave generator is also a problem. Although a 3-cm spatial resolution has been obtained by BOFDA in a silica single-mode fiber (SMF), such a high resolution has not been achieved in a POF not only because of the high propagation loss but also because of the weak Brillouin signal resulting from its large core diameter and multimode nature.

In this Section, we report on the first demonstration of distributed strain and temperature sensing with a centimeter-order spatial resolution in a POF based on Brillouin optical correlation-domain reflectometry (BOCDR), which is highly cost-effective. A 10-cm-long heated section—located away from both ends—of a 1.3-m-long POF is successfully detected with a theoretical spatial resolution of 7.4 cm and a sampling rate of 3.3 Hz per measured point (corresponding to a measurement time of approximately 1 minute, if the number of measured points is 200). We also discuss how the characteristics of POFs (Brillouin frequency shift (BFS), Brillouin bandwidth, propagation loss, etc.) affect the sensing performance of BOCDR.

3. 1. 2 Experimental setup

POFs employed in the experiment were PFGI-POFs with a numerical aperture of 0.185, a core diameter of 50 μm, a cladding diameter of 100 μm, an overcladding diameter of 500 μm, a core refractive index of approximately 1.35, and a propagation loss of approximately 250 dB/km at 1.55 μm. The core/cladding layers and the overcladding layer were composed of amorphous perfluorinated polymer and polycarbonate, respectively.

The schematic setup of BOCDR for distributed measurement in a POF is shown in Fig. 3.1.1, which is basically the same as that previously reported in [116]. All the optical paths except the POF were silica SMFs. A distributed-feedback laser diode at 1.55 μm with 1-MHz linewidth was used as a light source, and its output frequency was sinusoidally modulated by direct modulation of the driving current. Its output was divided into two light beams with a coupler. One was directly used as the reference light of heterodyne detection, after passing through a 1-km delay fiber to adjust the correlation peak order, and an erbium-doped fiber amplifier (EDFA) to enhance the beat signal. The other beam was amplified with another EDFA, and injected into the POF as the pump light (incident power: 27 dBm). The optical beat signal between the Stokes light and the reference light was then converted to an electrical signal with a photo detector (PD), which was finally monitored with an electrical spectrum analyzer (ESA) with a 300-kHz frequency resolution. Polarization state was optimized with a polarization controller (PC) at the beginning of each distributed measurement so that the Rayleigh noise was minimal [159].

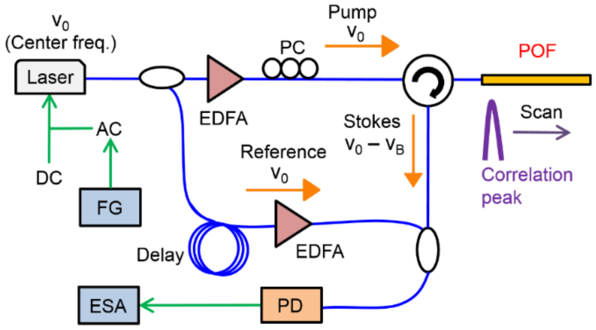

Fig. 3.1.1. (Color online) Schematic setup of BOCDR. EDFA, erbium-doped fiber amplifier; ESA, electrical spectrum analyzer; FG, function generator; PC polarization controller; PD, photo detector.

3. 1. 3 Experimental results

First, we demonstrate distributed strain and temperature sensing with a moderate spatial resolution but with a high SNR. The modulation frequency f_m was swept from 11.654 to 11.698 MHz, corresponding to the measurement range d_m of 9.5 m according to Eq. (1.14). The modulation amplitude Δf was set to 0.9 GHz, resulting in the theoretical spatial resolution Δz of 34 cm from Eq. (1.13) (the Brillouin bandwidth $\Delta\nu_B$ is approximately 100 MHz in a POF). Their ratio N_R was 28. The 56th correlation peak was used. The overall sampling rate of single-location measurement was 3.3 Hz.

Fig. 3.1.2 shows the structure of a 2-m-long POF to be measured, in which strains of < 1.2% were applied to a 50-cm-long section fixed on a translation stage, or the same section was heated up to 65°C. One end of the POF was butt-coupled to a silica SMF (second port of the circulator) via an SC connector, and the other end was cut at 8 degrees to suppress the Fresnel reflection. The room temperature was 18°C.

The measured BFS distribution when strain was applied is shown in Fig. 3.1.3(a). The measurement time was approximately 1 minute (200 points), which can be set shorter by reducing the measured points. The 50-cm-long strain-applied section was successfully detected. The BFS shifted to lower frequency with increasing strain with a proportionality constant of −115.3 MHz/%, which was moderately consistent with that previously reported (−121.8 MHz/% [141]). The BFS changed even along the strain-free sections by about ±10 MHz, which indicates that the strain measurement error is ±0.09%.

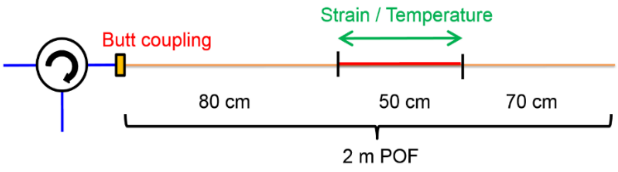

Fig. 3.1.2. Structure of POF under test (1).

The measured BFS distribution when temperature was changed is also shown in Fig. 3.1.3(b), where the 50-cm-long heated section was clearly detected. The measurement time was also about 1 minute. The proportionality constant of temperature dependence was −3.27 MHz/°C, which is in good agreement with previous result (−3.2 MHz/% [160]). The temperature measurement error was evaluated to be approximately ±3.1°C.

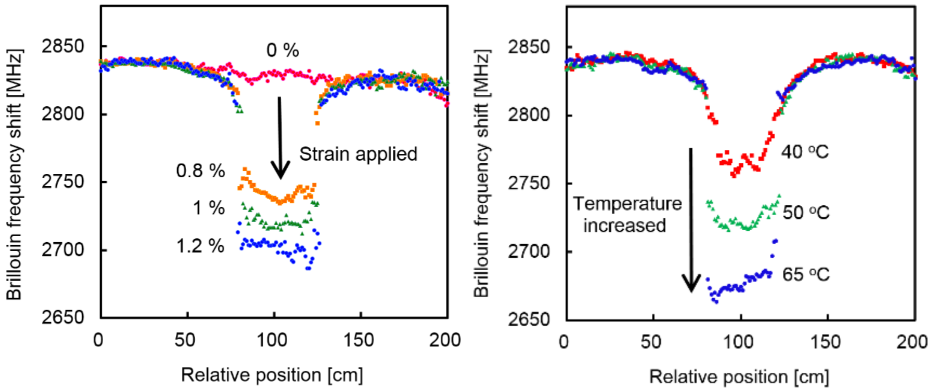

(a) (b)

Fig. 3.1.3. (Color online) Measured BFS distributions with a 50-cm-long section (a) strain-applied, and (b) heated.

Next, we demonstrate distributed temperature sensing with a centimeter-order spatial resolution. The modulation configurations of the light source were: f_m = 53.321 – 53.451 MHz and Δf = 0.9 GHz, corresponding to d_m of 2.1 m and Δz of 7.4 cm (N_R = 28). Fig. 3.1.4 shows the structure of a 1.3-m-long POF employed, where a 10-cm-long section was heated to 40°C.

Fig. 3.1.5(a) shows the measured distribution of normalized BGS along the POF, and Fig. 3.1.5(b) shows the BGS examples at non-heated and heated positions (relative positions of 67 cm and 104 cm, respectively). Fig. 3.1.5(c) shows the BFS distribution corresponding to Fig. 3.1.5(a). The measurement time was approximately 40 seconds (130 points). The BFS clearly downshifted at the 10-cm-long heated section. The amount of the BFS shift was approximately 26 MHz, which agrees well with the actual temperature (40°C). The gradual BFS changes at the relative positions of approximately 90 cm and approximately 115 cm were probably caused by the overlap of two broad BGSs ($\Delta\nu_B$ approximately 100 MHz) from the sections with and without temperature changed.

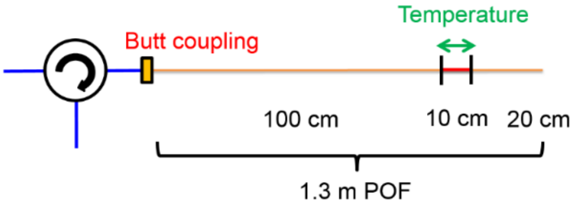

Fig. 3.1.4. (Color online) Structure of POF under test (2).

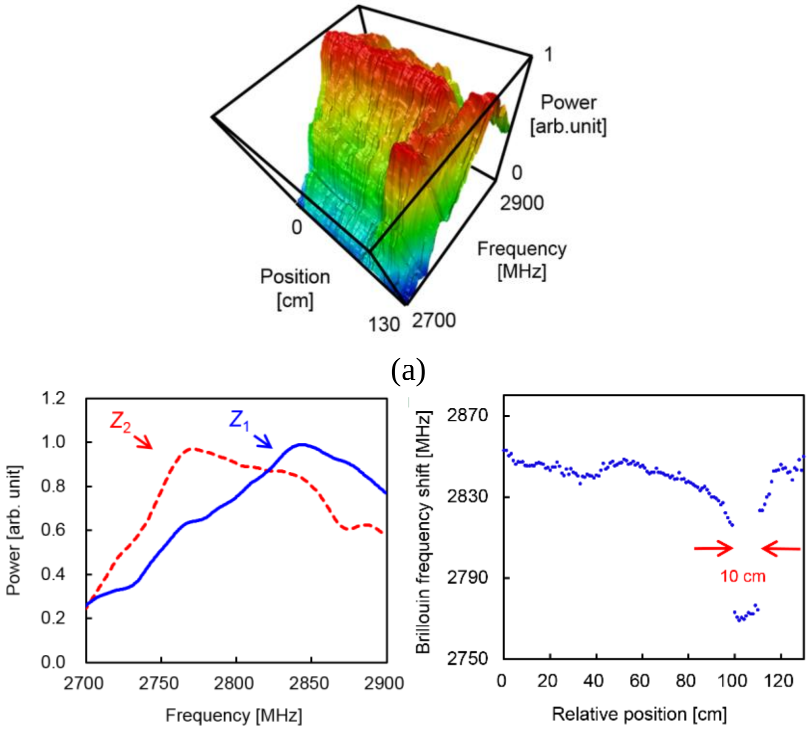

(b) (c)

Fig. 3.1.5. (Color online) (a) Normalized BGS distribution, (b) examples of BGS (Z_1: at 67 cm (room temperature); Z_2: at 104 cm (heated)), and (c) BFS distribution measured with cm-order resolution.

Finally, we compare the performances of POF-based BOCDR with those of silica SMF-based BOCDR. First, according to Eq. (1.15), the highest spatial resolution Δz_{min} theoretically achievable in POF-based BOCDR (ν_B approximately 2.8 GHz; n approximately 1.35) is calculated to be 23 mm, which is approximately 1/4 of that in SMF-based BOCDR (ν_B approximately 10.8 GHz; n approximately 1.46). However, a weak Brillouin signal in a POF [141], leading to a low SNR, practically limits the spatial resolution, as shown in the aforementioned experiment. Next, according to Eq. (1.17), the maximal number of effective sensing points N_{Rmax} of POF-based BOCDR ($\Delta\nu_B$ approximately 100 MHz) is calculated to be 44, which is approximately 1/13 of that of SMF-based BOCDR ($\Delta\nu_B$ approximately 30 MHz). This problem can be mitigated by employing so-called temporal-gating [120] and double-modulation schemes [121]. Note that the measurement range d_m itself is limited not only by its trade-off relation to Δz but also by the high propagation loss (250 dB/km at 1.55 μm) of the POF. Currently, the practical limitation of d_m is several tens of meters (depending on Δz, incident power, and many other parameters); we believe it can be elongated to several hundreds of meters by using shorter pump wavelengths at which the propagation loss is much lower. As for the sampling rate of single-location measurement, 3.3 Hz demonstrated in the experiment is restricted by the speed of signal acquisition from the ESA via a general-purpose interface bus, which might be further enhanced by use of faster data acquisition methods that have been implemented in SMF-based BOCDR and BOCDA. Highly accurate discriminative sensing of strain and temperature [161] using POFs is another important problem to be tackled.

3. 1. 4 Conclusion

Distributed strain and temperature sensing with a centimeter-order spatial resolution in a POF was demonstrated for the first time using a cost-effective BOCDR technique. A 10-cm-long heated section of a 1.3-m-long POF was successfully detected with a theoretical spatial resolution of 7.4 cm and a sampling rate of 3.3 Hz (per measured point). The limitation of the sensing performances was discussed. We believe that our results have overcome a stereotype of perceiving POF-based Brillouin distributed sensing with a high resolution and/or a high SNR as almost infeasible.

3. 2 Simplification of experimental setup

In this Section, first, we develop simplified (S-) BOCDR, where the light Fresnel-reflected at a partial reflection point (or the fiber end) is used as reference light and an additional reference path used in standard implementations can be removed. This configuration is useful for practical application and enhancement of SNR in BOCDR. Then, we implement S-BOCDR using a POF as a fiber under test, which provides the following advantages over S-BOCDR using a standard silica single-mode fiber (SMF): (1) the Fresnel-reflected light can be stably returned at the interface between the POF and an SMF (the pigtail of an optical circulator), and (2) the effect of the 0th correlation peak can be easily and effectively suppressed by exploiting a so-called BFS-hopping phenomenon. We then experimentally demonstrate a distributed measurement and detect a 0.46-m-long heated POF section.

3. 2. 1 Introduction

One of the practical advantages of BOCDR is a system simplicity and cost efficiency; the experimental setup of its basic configuration does not include relatively expensive devices, such as electro-optic modulators (optical-pulse generators, single-sideband modulators, etc) and vector network analyzers (cf. Brillouin optical frequency-domain analysis (BOFDA). Further simplification of the BOCDR system will greatly enhance its utility.

In this work, first, we develop an even simpler experimental setup of BOCDR, named S-BOCDR (S-BOCDR-1), which exploits as reference light the Fresnel-reflected light from an open end of a sensing fiber and does not include an additional reference path used in standard implementations. After clarifying the theoretical limitations of spatial resolution, measurement range, and their ratio, we demonstrate a distributed strain measurement with a < 100-mm spatial resolution and a 4.1-m measurement range. Then, we focus on two disadvantages of S-BOCDR: (1) measurement can be performed only along half of the FUT length (distal from the open end), and (2) measurement cannot be continued when the FUT has even one breakage point. To overcome these drawbacks, we here develop an alternative configuration of S-BOCDR (S-BOCDR-2) where the light Fresnel-reflected at a partial reflection point (artificially produced near an optical circulator) is used as reference light. With this configuration, measurement of another half of the FUT length (proximal to the open end) is possible, which is more convenient for practical applications. Even when the FUT has a breakage point, measurement can be conducted at least up to that point. We demonstrate a distributed measurement for detecting a 1.46-m-long strained section with a high signal-to-noise ratio (SNR). Finally, by implementing S-BOCDR-2 using a POF, we mitigate the two problems still remaining in S-BOCDR-2: (1) the unstable power of the Stokes light that propagates through the partial reflection point (such as an air gap; extensive disturbance makes a distributed measurement difficult), and (2) the need for preparation of optical fibers with sufficiently different BFS values, which are inserted around the partial reflection point to suppress the influence of the 0th correlation peak. As for problem (1) mentioned above, the Stokes light can be stably returned from the POF through the interface between the POF and the silica SMF; this structure is simpler and more robust than that of previous S-BOCDR-2. As for problem (2), the BFS in the POF can be irreversibly upshifted by approximately 300 MHz only by applying large strain (named BFS hopping). A distributed measurement is experimentally demonstrated, in which a 0.46-m-long heated POF section is successfully detected.

3. 2. 2 Principle

A basic BOCDR setup is depicted in Fig. 3.2.1(a) in Ref. [116]. The beat signal of

Stokes and reference lights is detected as a BGS. By sinusoidal modulation of the laser frequency, correlation peaks are periodically distributed along the FUT; the distance between the adjacent peaks is set to be longer than the FUT length, so that only one correlation peak exists in the FUT. Correlation peaks of any order can be located in the FUT by controlling the optical path-length difference between the pump and the reference paths. The correlation peak position can be scanned along the FUT by sweeping the frequency of the sinusoidal modulation; thus, a distributed BGS measurement can be performed. As has been discussed in detail and summarized in Ref. [117], the measurement range, spatial resolution, theoretical value of the highest resolution, range-to-resolution ratio (effective number of sensing points), and theoretical value of the highest ratio are expressed as Chap. 1, Section 3.3.

Fig. 3.2.1(b) shows a setup of S-BOCDR. In Fig. 3.2.1(b), the laser output is injected directly into the FUT, and the reflected light (consisting not only of the Brillouin-Stokes light but also of the reference light that is Fresnel reflected at the FUT open end) is detected. When the laser frequency is subject to sinusoidal modulation, correlation peaks are generated along the FUT. As the 0th correlation peak is fixed at a zero-optical-path-difference point, i.e., at the FUT open end, some loss is artificially applied near the open end to suppress its influence. The initial configuration of S-BOCDR has two drawbacks: (1) the measurement range is limited to half of the FUT length (distal from the open end) and (2) the measurement becomes non-feasible when the FUT has a breakage point. The measurement range, spatial resolution, theoretical value of the highest resolution, range-to-resolution ratio, and theoretical value of the highest ratio are given by

$$d_{\text{S-BOCDR}} = \frac{L}{2}, \tag{3.1}$$

$$\Delta z_{\text{S-BOCDR}} = \frac{\Delta\nu_B\,(L-l)}{\pi\,\Delta f}\ , \tag{3.2}$$

$$\Delta z_{\text{S-BOCDR}}^{\min} = \frac{2\,\Delta\nu_B\,(L - l)}{\pi\,BFS}\ , \tag{3.3}$$

$$N_{\text{S-BOCDR}} = \frac{\pi\,\Delta f}{2\,\Delta\nu_B}\,, \tag{3.4}$$

$$N_{\text{S-BOCDR}}^{\max} = \frac{\pi\,BFS}{4\,\Delta\nu_B}\,, \tag{3.5}$$

respectively, where L is the FUT length, and l is the sensing position in the FUT.

Two configurations of S-BOCDR will be presented in this Section; one (S-BOCDR-1) uses the light Fresnel-reflected at the open end of the FUT, while the other (S-BOCDR-2) uses the light Fresnel-reflected at the partial reflection point artificially induced near an optical circulator. When the laser frequency is subject to sinusoidal modulation, correlation peaks are generated along the FUT. As the 0th correlation peak is fixed at a zero-optical-path-difference point, i.e., at the FUT open end (S-BOCDR-1) or at the partial reflection point (S-BOCDR-2), its influence needs to be suppressed, for example, by applying some artificial loss near the open end (S-BOCDR-1) or by replacing the nearby fibers with fibers that have different BFS values (S-BOCDR-2). The measurement range in both S-BOCDR schemes is limited to one-half of the FUT length: distal from the open end (S-BOCDR-1) or proximal from the open end (S-BOCDR-2), the latter of which is more convenient for practical applications. When the FUT has a breakage point, the measurement becomes non-feasible in S-BOCDR-1, although the measurement can be

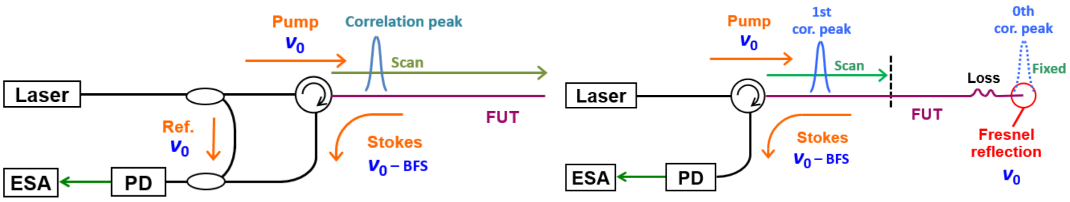

(a) (b)

Fig. 3.2.1. Schematics of (a) basic BOCDR configuration and (b) initial S-BOCDR configuration. ESA, electrical spectrum analyzer;

continued at least to that breakage point. Thus, broadly speaking, S-BOCDR-2 is superior in performance to S-BOCDR-1, from a practical viewpoint.

Schematic presentation of an alternative S-BOCDR setup is shown in Fig. 3.2.2. Similar to the case in S-BOCDR (Fig. 3.2.1(b)), the laser output here is directly injected into the FUT, and the reflected light is guided to a photodiode (PD) followed by an electrical spectrum analyzer (ESA). At the interface between the pigtail of the optical circulator and one end of the FUT, partial reflection is artificially induced, whereas the other end of the FUT is angle-cut to suppress the Fresnel reflection and is kept open. Then, the reflected light consists of the Brillouin-Stokes light and the light that is Fresnel reflected at the partial reflection point, which works as a reference light. When sinusoidal modulation is applied to the laser frequency, correlation peaks appear along the FUT. The 0th correlation peak, generally fixed at a zero-optical-path-difference point, is located at the partial reflection point in this case. As shown in Fig. 3.2.2, the influence of the 0th peak needs to be suppressed by replacing the nearby fibers with fibers that have different BFS values (unless low-temperature measurement is aimed at, lower BFS is preferable because the BFS in silica SMFs increases with increasing applied strain [35] and increasing temperature [36]). As the modulation frequency increases, the 1st correlation peak gradually approaches the 0th peak. While only the 1st peak (except the 0th peak) exists in the FUT, a distributed measurement can be properly performed. When the 1st peak has reached the FUT midpoint, the 2nd peak starts to appear at the FUT open end, resulting in the measurement error. By the same reasoning, the length of the circulator pigtail needs to be sufficiently shorter than half of the FUT length. Thus, the measurement range of the alternative S-BOCDR is limited to half of the FUT length L, i.e., Eq. (3.1) is valid; however, a major difference is that the measurement range is located proximal to the open end, which is more convenient for practical applications. The spatial resolution can be expressed by Eq. (3.2), provided the sensing position l in the FUT is defined as shown in Fig. 3.2.3. Consequently, the theoretical value of the highest resolution, range-

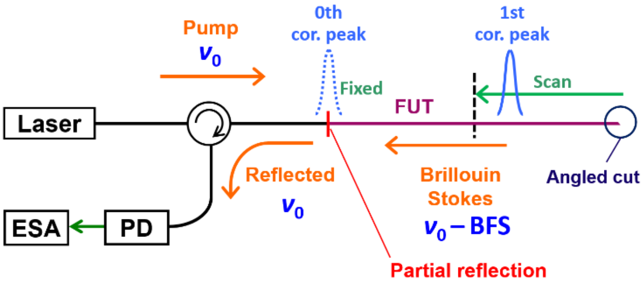

Fig. 3.2.2. Schematic of alternative S-BOCDR.

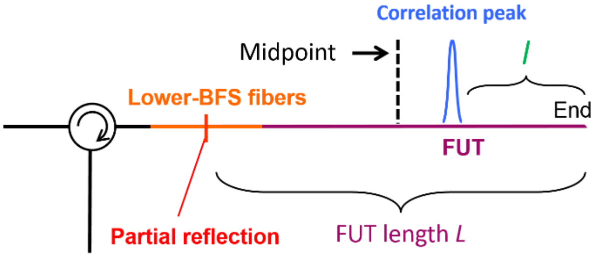

Fig. 3.2.3. Definitions of L and l.

to-resolution ratio, and theoretical value of highest ratio of the alternative S-BOCDR are also expressed by Eqs. (3.3), (3.4), and (3.5), respectively. It should be noted that the range-to-resolution ratio is calculated by using the lowest resolution ($l = 0$), because the resolution dramatically depends on the sensing position l.

However, S-BOCDR-2 suffers from two problems. One is that the Stokes light is not stably returned from the FUT through the partial reflection point, leading to a low measurement stability. For instance, an air gap was used to induce partial reflection, which was susceptible to external disturbance. The other problem is that we need to prepare optical fibers with sufficiently different BFS values and insert them around the partial reflection point to suppress the influence of the 0th correlation peak. Silica multi-mode fibers with BFS values of approximately 10.5 GHz were inserted, though this necessity is undesirable.

Here, we show that these two problems of S-BOCDR-2 can be mitigated by implementing it using a POF as an FUT. Then, a partial reflection point can be automatically created at the butt-coupled interface between the POF and the silica SMF (the pigtail of an optical circulator) [154], at which Fresnel-reflected light with a reflectivity of 0.2% (calculated using n = 1.46 in a silica SMF and 1.35 in a PFGI-POF) is obtained; the Stokes light can stably pass through the interface. The key to the solution of the second problem is the BFS hopping phenomenon, in which the BFS in the POF (BFS: approximately 2.8 GHz) can be irreversibly upshifted by approximately 300 MHz only by applying a large strain of >7.3%. Unless cryogenic sensing is the intended application, the BFS "upshift" is preferable because the BFS in a POF decreases with increasing applied strain and temperature. Thus, instead of inserting different fibers around the butt-coupled part, we have only to pull the POF for a length sufficiently longer than half of the spatial resolution (i.e., the width of the 0th correlation peak). Note that, as the BGS of the silica SMF (BFS: approximately 10.8 GHz) near the butt-coupled part does not overlap with that of the POF, it requires no modification.

3. 2. 3 Experimental results

We present three demonstrations: (i) distributed sensing based on S-BOCDR-1, (ii) distributed sensing based on S-BOCDR-2, and (iii) distributed sensing based on S-BOCDR-2 using a POF.

3. 2. 3. 1 Demonstration 1

The S-BOCDR setup used in the experiment is depicted in Fig. 3.2.3. The pump light was amplified up to approximately 30 dBm with an erbium-doped fiber amplifier (EDFA), and a 10-dB bending loss (experimentally optimized) was applied to the section near the open end. Considering that the Fresnel reflectivity at the open end which is cut vertically to the fiber axis is approximately 4% (= –14 dB), the reference power at the PD was roughly calculated to be –4 dBm. The sinusoidal modulation of the laser frequency was performed by directly modulating the laser driving current.

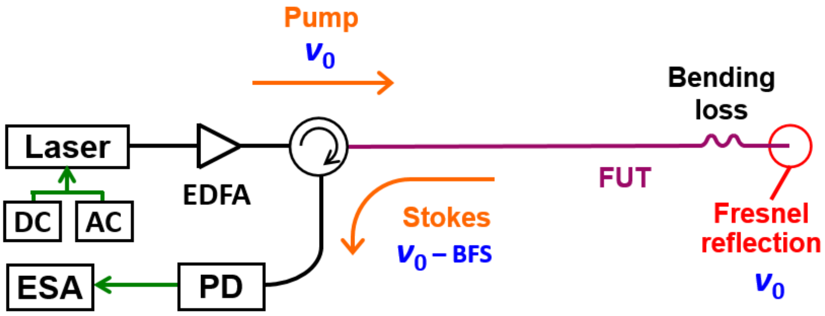

Fig. 3.2.3. Experimental setup of S-BOCDR.

We employed a silica SMF as an FUT, which had a numerical aperture of 0.13, a core refractive index of approximately 1.46, a core diameter of 9 μm, a cladding diameter of 125 μm, and a propagation loss of approximately 0.5 dB/km at 1.55 μm. The FUT length was 8.2 m, leading to the measurement range of 4.1 m. In this paper, to clearly show a distributed measurability with a high SNR, we swept the modulation frequency f_m from 12.370 MHz to 24.445 MHz and fixed the modulation amplitude Δf at 0.82 GHz, corresponding to the spatial resolution of approximately 95 mm at l = 0 m and approximately 48 mm at l = 4.1 m. Using two translation stages, different strains of < 0.6% were applied to a 0.6-m-long section of the FUT (see Fig. 3.2.4 for the detailed FUT structure). The sampling rate at a single sensing point was 3.3 Hz, limited by the data acquisition from the ESA. The number of the sensing points was set to 41, and consequently, the measurement time was approximately 12 s. The operating temperature was kept at 27°C.

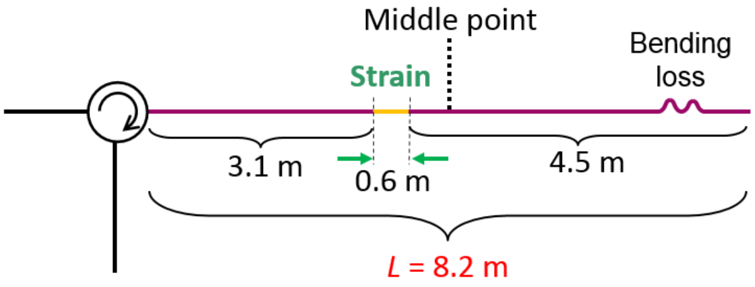

Fig. 3.2.4. Structure of FUT.

The measured BGS distribution with a 0.56-% strain applied is shown in Fig. 3.2.5. A BFS upshift was observed at the strain-applied section with a high SNR. The measured BFS distributions with strains of 0.00, 0.27, 0.40, and 0.56% applied (Fig. 3.2.6) shows that the 0.6-m-long strain-applied section was successfully detected. As shown in the inset of Fig. 3.2.6, the BFS shifted to higher frequencies with increasing strain with a proportionality constant of 491 MHz/% (calculated using the BFS values at the middle point of the strain-applied section). This value is in good agreement with the previously reported value [35]. The BFS changed even along the strain-free sections by about ±2.1 MHz (standard deviation), which indicates that the strain and temperature measurement errors are approximately ±0.004% and approximately ±1.8 °C, respectively. Thus, a distributed measurability based on S-BOCDR was demonstrated.

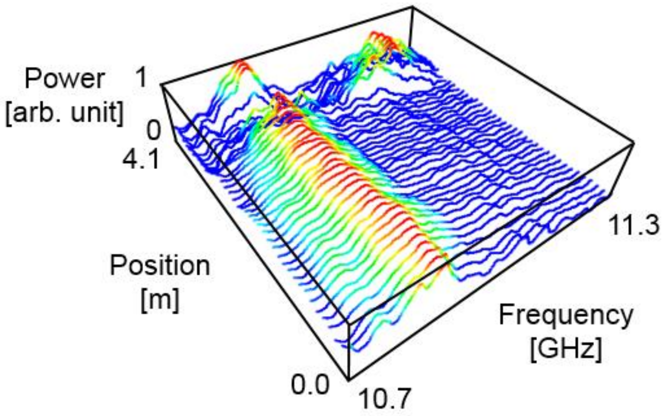

Fig. 3.2.5. Measured BGS distribution when a strain of 0.56% was applied.

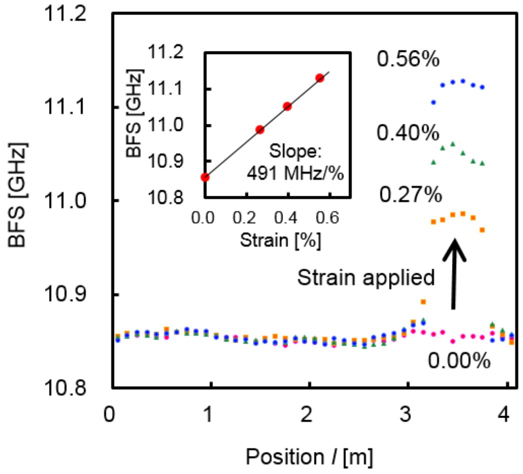

Fig. 3.2.6. Measured BFS distribution when strains of 0.00, 0.27, 0.40, and 0.56% were applied. The inset shows the BFS dependence on applied strain.

3. 2. 3. 2 Demonstration 2

Schematic of the alternative S-BOCDR setup used in the experiment is shown in Fig. 3.2.7. The pump light was amplified up to approximately 30 dBm using an erbium-doped fiber amplifier (EDFA). The sinusoidal modulation of the laser frequency was performed by directly modulating the laser driving current.

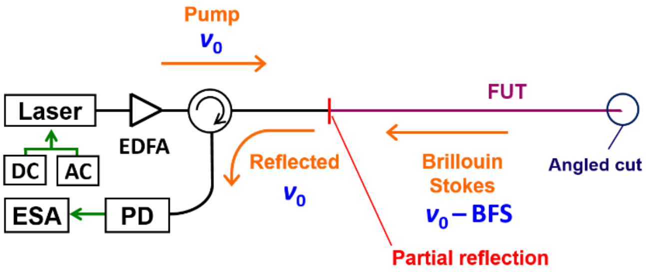

Fig. 3.2.7. Experimental setup of alternative S-BOCDR.

First, a pilot distributed measurement was performed without suppressing the influence of the 0th correlation peak. The FUT structure is shown in Fig. 3.2.8. We employed a silica SMF as an FUT, which had a numerical aperture (NA) of 0.13, a core refractive index of ~1.46, a core diameter of 9 μm, a cladding diameter of 125 μm, and a propagation loss of approximately 0.5 dB/km at 1.55 μm. Partial reflection was induced by forming a small gap (reflectivity approximately 0.05%). The FUT length was 18.00 m, leading to the measurement range of 9.00 m. In this study, to clearly show a distributed measurability with a high SN ratio, we swept the modulation frequency f_m from 5.7038

MHz to 11.408 MHz and fixed the modulation amplitude Δ*f* at 0.50 GHz, corresponding to the spatial resolution of approximately 170 mm at *l* = 0 m and approximately 340 mm at *l* = 9.00 m. Using two translation stages, we applied different strains of <0.7% to a 1.46-m-long section of the FUT. The sampling rate at a single sensing point was 3.3 Hz (limited by the data acquisition from the ESA). There were 45 sensing points, and the measurement lasted for approximately 14 s. The operating temperature was maintained at 28°C.

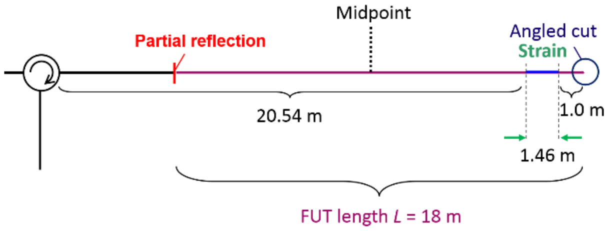

Fig. 3.2.8. Structure of the FUT without 0th peak suppression.

The measured BGS distribution with an applied strain of 0.50% is shown in Fig. 3.2.9(a), and the measured BGSs at *l* = 8.00 m (no strain) and at *l* = 1.40 m (strained) are shown in Fig. 3.2.9(b). Irrespective of the sensing position, the peak frequency of the BGS was 10.86 GHz, corresponding to the BFS of a non-strained silica SMF. Thus, the strained section was not detected, because the measured BGS was constantly overlapped by the BGS of the light that was Brillouin scattered at the 0th correlation peak. This result indicates that suppression of the 0th peak is indispensable for the correct operation of the alternative S-BOCDR.

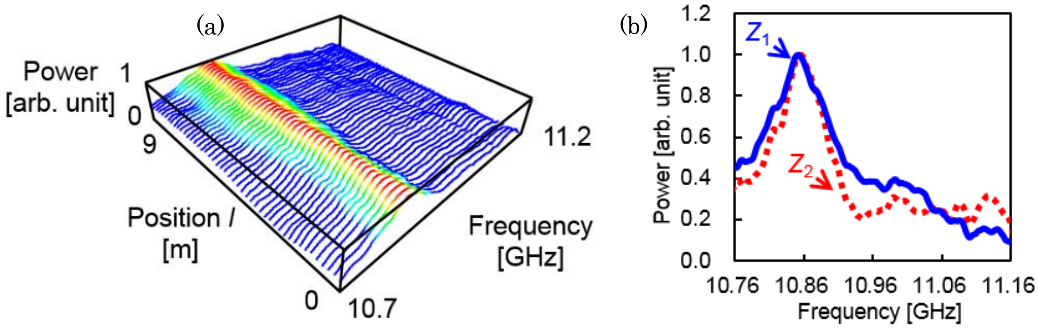

Fig. 3.2.9. (a) Measured BGS distribution without 0th peak suppression. (b) Measured BGSs at *l* = 8.00 m (Z_1; no strain) and at *l* = 1.40 m (Z_2; strained).

Next, the distributed measurement was performed after suppressing the influence of the 0th correlation peak. As shown in Fig. 3.2.10, two 3.00-m-long silica multi-mode fibers (MMFs) with a BFS value of approximately 10.5 GHz [148] were inserted at around the partial reflection point; this frequency serves as the lower limit of the measurable BFS range, corresponding to the BFS of silica SMFs at roughly –330 °C. These MMFs had an NA of 0.20, a core refractive index of approximately 1.46, a core diameter of 50 μm, a cladding diameter of 125 μm, and a propagation loss of approximately 1.0 dB/km at 1.55 μm. The two interfaces of the MMFs and SMFs were connected by adaptors. Other conditions were the same as those in the preceding experiment.

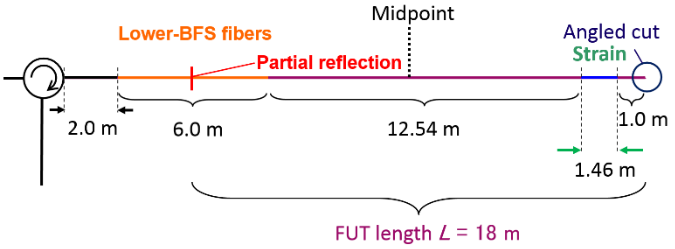

Fig. 3.2.10. Structure of the FUT with 0th peak suppression.

The measured BGS distribution with an applied strain of 0.50% is shown in Fig. 3.2.11(a), and the measured BGSs at l = 8.00 m (no strain) and at l = 1.40 m (strained) are shown in Fig. 3.2.11(b). A BFS upshift was clearly observed at the strained section. In Fig. 8(b), at l = 1.40 m (strained), a smaller undesired peak was observed at approximately 10.86 GHz, which was caused by the sidelobes of the 1st correlation peak. Even with this effect, a distributed measurement can be correctly performed, but the measurable maximal strain (or temperature change) is sometimes limited. This limitation can be mitigated by using an apodization technique based on intensity modulation [84,85]. The measured BFS distributions for applied strains of 0.00, 0.39, 0.50, and 0.63% (Fig. 3.2.9) revealed that the 1.46-m-long strained section was successfully detected. As shown in the inset of Fig. 3.2.12, the BFS shifted to higher frequencies with increasing strain with a proportionality constant of 491 MHz/% (calculated using the BFS values at the midpoint of the strained section), which agrees well with the reported value [35]. The BFS fluctuations at the non-strained sections were approximately ±2.3 MHz (standard deviation), corresponding to the strain and temperature measurement errors of approximately ±0.005% and approximately ±2.3 °C, respectively. Thus, a distributed measurement capability of the alternative S-BOCDR was demonstrated.

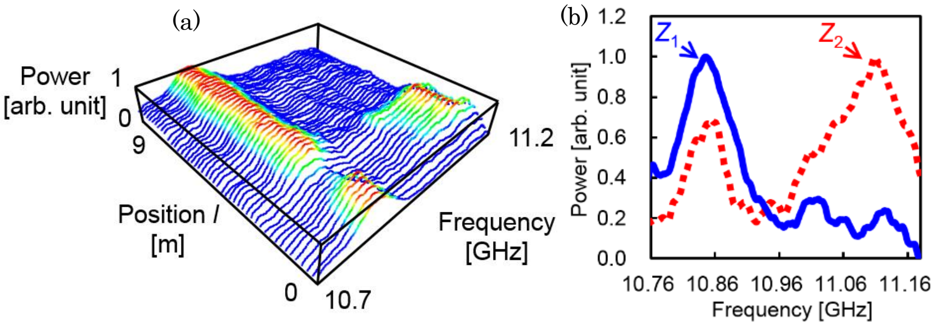

Fig. 3.2.11. (a) Measured BGS distribution with 0th peak suppression. (b) Measured BGSs at *l* = 8.00 m (Z_1; no strain) and at *l* = 1.40 m (Z_2; strained).

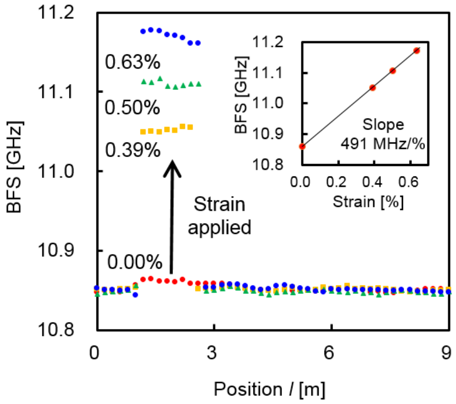

Fig. 3.2.12. Measured BFS distribution when strains of 0.00, 0.39, 0.50, and 0.63% were applied. The inset shows the BFS dependence on the applied strain.

3. 2. 3. 3 Demonstration 3

An S-BOCDR-2 setup using a POF as an FUT is schematically shown in Fig. 3.2.13. The pump light at 1.55 μm was amplified up to approximately 30 dBm using an erbium-doped fiber amplifier (EDFA) and was injected into the POF by an optical circulator. The optical beat signal of the Brillouin Stokes light and the Fresnel-reflected light was converted into an electrical signal using a photo detector (PD) and was observed using an electrical spectrum analyzer (ESA) as a BGS. All the optical paths except the FUT were composed of silica SMFs. The laser output frequency was sinusoidally modulated by direct modulation of the driving current. As an FUT, we employed a 3.39-m-long PFGI-POF with 50 μm core diameter, 70 μm cladding diameter, and 490 μm overcladding

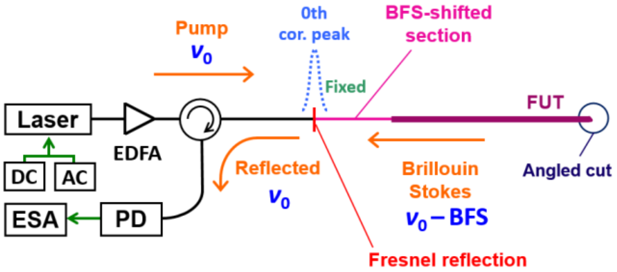

Fig. 3.2.13. Experimental setup of S-BOCDR-2 using a POF.

diameter. The core and cladding layers were composed of doped and undoped polyperfluorobutenylvinyl ether. The refractive index at the core center was 1.35, the numerical aperture was 0.185, and the propagation loss at 1.55 μm was approximately 250 dB/km. The detailed FUT structure is shown in Fig. 3.2.14. One end of the FUT was butt-coupled to a 1.05-m-long silica SMF (the pigtail of a circulator), and the other end was left open and cut with an angle to suppress the Fresnel reflection at that end. In order to suppress the influence of the 0th correlation peak generated at the butt-couple, a 0.32-m-long nearby section of the FUT was elongated and then released, resulting in a length of 0.51 m (corresponding to 59% strain). Consequently, the whole length of the FUT became 3.58 m, leading to a measurement range of 1.79 m. In this experiment, to clearly show the distributed measurability, we swept the modulation frequency f_m from 31.0366 MHz to 62.0732 MHz and fixed the modulation amplitude Δf at 1.33 GHz, corresponding to a spatial resolution of approximately 42 mm at l = 0 m (open end) and approximately 84 mm at l = 1.79 m (midpoint). These values were much smaller than twice the length of the BFS-shifted section. A 0.46-m-long section of the FUT near the open end was heated (<70 °C), as shown in Fig. 3.2.2. The sampling rate at a single sensing point was 3.3 Hz (limited by the data acquisition from the ESA). There were 89 sensing points, and the measurement lasted for approximately 27 s. The operating temperature was maintained at 24 °C.

First, the BGS over the whole length of the FUT was measured (Fig. 3.2.15). The frequency of the laser output was fixed. The vertical axis was normalized so that the maximal power of the BGS was 1. The peak at approximately 2.79 GHz corresponds to the BGS in the unstrained POF section, whereas the peak at approximately 3.11 GHz corresponds to the BGS in the strained (BFS-shifted) POF section. Thus, the BFS in the POF section around the butt-couple was verified to be upshifted.

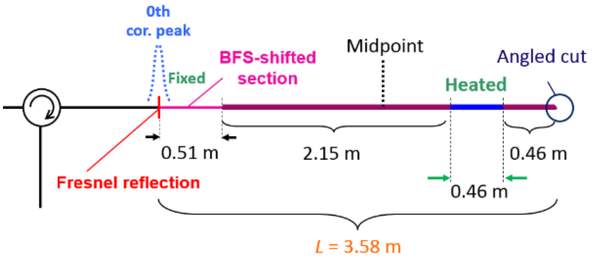

Fig. 3.2.14. Structure of the FUT.

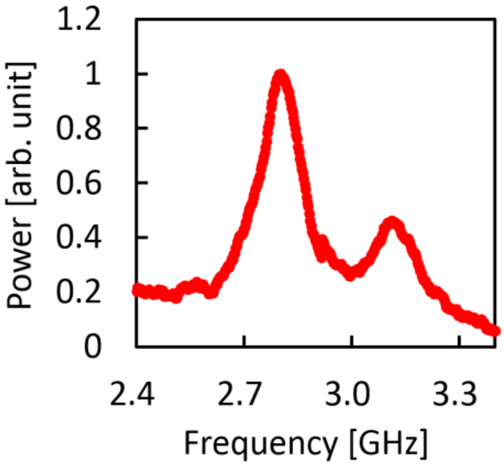

Fig. 3.2.15. Measured BGS in the whole length of the FUT.

Subsequently, the BGS distribution was measured when the FUT was locally (l = 0.46–0.92 m) heated to 60 ºC, as shown in Fig. 3.2.16(a), and the measured BGSs at l = 1.15 m (room temperature) and at l = 0.59 m (heated) are shown in Fig. 3.2.16(b). The vertical axes were normalized so that the maximal powers of all the BGSs were 1, because even the highest Stokes power of -84.68 dBm was extremely close to the noise floor level of -84.78 dBm. A BFS downshift was clearly observed at the heated section. The BFS distributions measured at different temperatures (24, 50, 60, and 70 ºC) are shown in Fig. 3.2.17, where the 0.46-m-long heated section was successfully detected. As shown in the inset of Fig. 3.2.17, the BFS decreased with increasing temperature, with a proportionality constant of –3.2 MHz/K (calculated using the BFS values at the midpoint of the heated section), which agrees well with a previously reported value [160]. The BFS fluctuations along the non-heated sections showed a standard deviation of approximately ±3.0 MHz, corresponding to strain and temperature measurement errors of around ±0.02% and ±0.9 °C, respectively. Thus, a distributed measurement capability of S-BOCDR-2 using a POF was demonstrated.

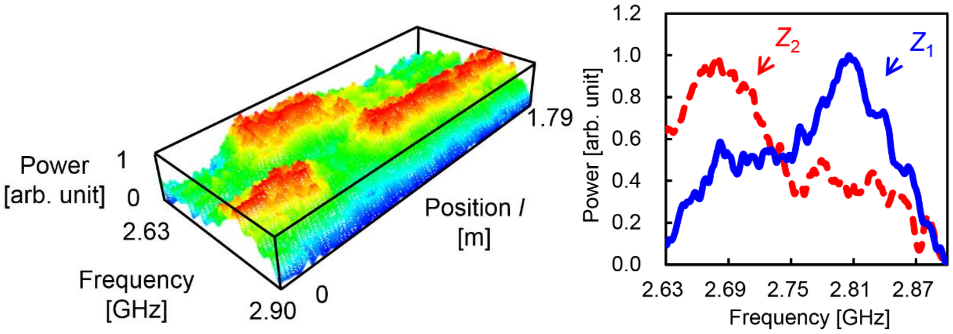

(a) (b)

Fig. 3.2.16. (a) Measured BGS distribution when the FUT was locally heated to 60˚C. (b) Measured BGSs at l = 1.15 m (room temperature; z_1) and at l = 0.59 m (heated; z_2).

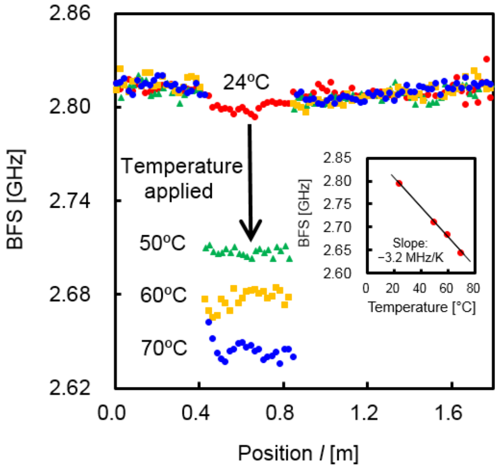

Fig. 3.2.17. Measured BFS distributions when the FUT was locally heated to 24, 50, 60, and 70 °C. The inset shows the measured BFS dependence on temperature change.

3. 2. 4 Discussion

We have to admit that S-BOCDR has the following drawbacks: (1) an FUT with a length of double the measurement range needs to be employed, (2) the range-to-resolution ratio is reduced by half, (3) if the sensing fiber is cut during the operation, the measurement cannot be continued, (4) the polarization state cannot be fully optimized using standard polarization controllers (which does not matter if polarization scrambling [162] is employed to stabilize the measurement), and (5) the system simplification does not necessarily lead to a significant reduction in cost. However, it is of considerable physical interest that a high-resolution distributed measurement can be performed by such a simple setup. Moreover, the successful demonstration of the S-BOCDR operation implies that this principle could in turn be a possible noise source for standard BOCDR systems, providing a useful guideline for improving their SNR. In this Subsection, we experimentally verify this aspect.

All of the BOCDR-based distributed measurements along the whole length of an FUT with polarization scrambling (or diversity) have been performed using a specially-devised open end (i.e. (1) or (2))[162] without any specific reason (if the polarization state is optimized for the desired correlation peak, the measurement can be sometimes correctly performed using the open end even with a physical contact (PC) type connector [116]). Further clarification of this point is extremely important for the optimal system design in future.

Here, we investigate the influence of this “ghost” correlation peak on the BOCDR performance. By measuring the Brillouin spectrum dependence on the bending loss applied near the open end of the FUT, we show that > 5-dB loss should be applied to suppress the influence of the ghost peak in this experiment. We also demonstrate a distributed strain measurement with 6-dB bending loss applied, and present the importance of the ghost-peak suppression.

Basic theory of the BOCDR operation was shown in Chapter 1, Section 3, but we should note here that an undesired “ghost” correlation peak exists at the open end of the FUT, as shown in Fig. 3.2.18. This is because the 0th correlation peak is generally generated at the zero-optical-path-length-difference position, which is the open end of the FUT when the light Fresnel-reflected there acts as the reference light. This ghost peak turns out a noise source and deteriorates the SN ratio of a distributed measurement, because the Brillouin spectrum from the ghost peak constantly overlaps that from the desired peak.

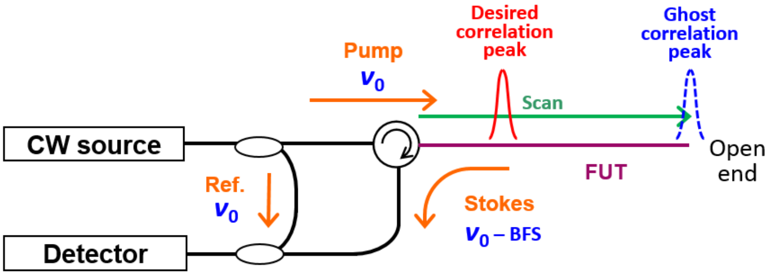

Fig. 3.2.18. Conceptual schematic of a standard BOCDR setup for investigating the influence of a ghost correlation peak.

The experimental setup of BOCDR for investigating the influence of the ghost correlation peak is shown in Fig. 3.2.19. All the optical paths were composed of silica SMFs. A distributed-feedback laser diode at 1.55 μm with 1-MHz linewidth was used as a light source, and the optical frequency of its output was sinusoidally modulated by direct modulation of the driving current. The frequency-modulated output was divided into two beams with a 3-dB coupler. One beam was guided through a 1-km delay line (to adjust the correlation peak order), amplified to approximately 22 dBm with an erbium-doped fiber amplifier (EDFA), and used as the reference light of heterodyne detection. The other beam was polarization-scrambled [162], amplified with another EDFA, and injected into the FUT as the pump light (incident power: 28 dBm). A 99:1 coupler was used to mix the Stokes light and the reference light to obtain their optical beat signal, which was attenuated by 12.8 dB, converted to an electrical signal with a photo detector (PD), and finally monitored with an electrical spectrum analyzer (ESA) with 300-kHz frequency resolution. Here, the attenuation was required to avoid the gain saturation of the PD output.

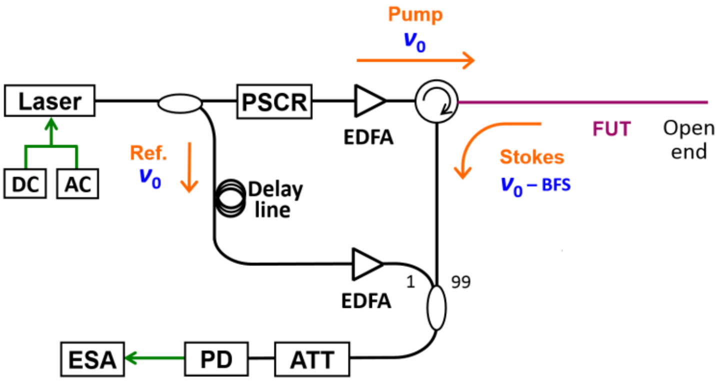

Fig. 3.2.19. Experimental setup of BOCDR containing an optical attenuator (ATT), erbium-doped fiber amplifiers (EDFAs), an electrical spectrum analyzer (ESA), a photo detector (PD), and a polarization scrambler (PSCR).

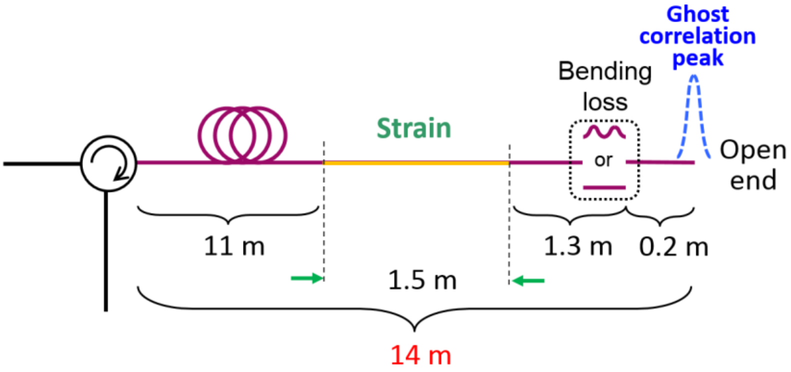

Fig. 3.2.20. Structure of the FUT.

As the FUT, we used a 14-m-long silica SMF with a numerical aperture of 0.13, a core diameter of 9 μm, a cladding diameter of 125 μm, a core refractive index of approximately 1.46, and a propagation loss of approximately 0.5 dB/km at 1.55 μm. The modulation frequency f_m was swept from 2.8557 to 2.9394 MHz, corresponding to the

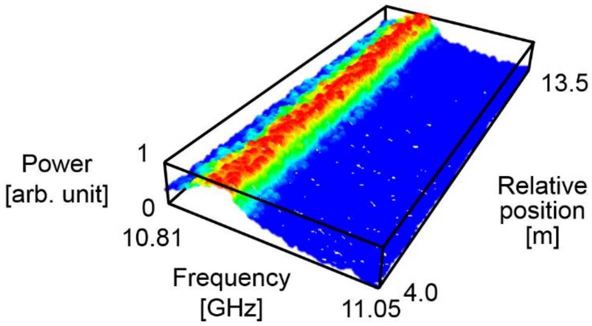

Fig. 3.2.21. BGS distribution measured when the FUT end was simply kept open. A strain of 0.20 % was partially applied to the FUT.

measurement range d_m of 35 m according to Eq. (1.14). The modulation amplitude Δf was set to 0.7 GHz, resulting in the theoretical spatial resolution Δz of 48 cm from Eq. (1.13). The 14th correlation peak was used. The overall sampling rate of a single-location measurement was approximately 3.3 Hz; as the number of the sensing points was 280, the total measurement time was approximately 84 s.

First, we tried a distributed strain measurement without suppressing the ghost correlation peak. The FUT structure is shown in Fig. 3.2.20. A strain of 0.20 % was applied to a 1.5-m-long section of the SMF. The end of the FUT was kept open, which means that a ghost peak exists there. Fig. 3.2.21 shows the measured BGS distribution along the FUT, where the strained section was not detected.

Next, using the same FUT, we applied a variable bending loss near the open end, as shown in Fig. 3.2.20. Fig. 3.2.22(a) shows the BGS dependence on the bending loss measured when the desired correlation peak was fixed at the midpoint of the strained section. Owing to the scrambled polarization state, the spectral power fluctuations were less than ±0.05 dB. Without the bending loss, the BGS peak was observed at approximately 10.87 GHz, which corresponds to the BFS of an unstrained silica SMF near the open end, where the ghost peak was fixed (the shape of the peak was slightly distorted because of the noise floor of the ESA [162]). However, with increasing bending loss, the BGS peak at approximately 10.87 GHz gradually disappeared, and at approximately 6 dB, the BGS peak at approximately 10.98 GHz was clearly observed. This newly appeared peak corresponds to the BFS of the strained silica SMF section, where the desired correlation peak existed. Fig. 3.2.22(b) shows the BGS peak powers at approximately 10.98 GHz (desired) and approximately 10.87 GHz (ghost) plotted as functions of the bending loss. As the loss increased, both the powers decreased; and the power from the desired peak became higher than that from the ghost peak when the bending loss exceeded approximately 5 dB. This suggests that > 5-dB loss needs to be induced near the open end of the FUT to perform a correct distributed strain measurement in this configuration.

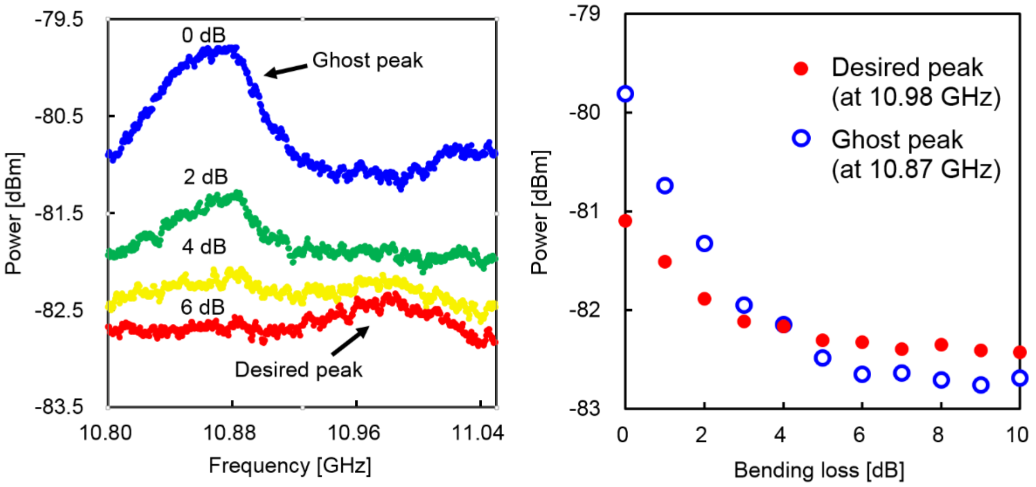

Fig. 3.2.22. (a) BGS dependence on the bending loss measured when the desired correlation peak exists at the midpoint of the strained section (0.20 %). (b) BGS peak powers at ~10.98 GHz (desired) and ~10.87 GHz (ghost) measured as functions of bending loss.

Finally, a distributed measurement was performed when 6-dB bending loss was applied near the FUT end. Other experimental conditions were the same as described above (i.e., those used to obtain Fig. 3.2.21). Fig. 3.2.23(a) shows the BGS distribution measured when the applied strain was 0.20 %; the strained section was correctly detected. Note that the SN ratio of this measurement is lower than those of some of the previously reported results [116,118,162]. This originates from the fact that the optical heterodyne signal was artificially attenuated by 12.8 dB in order to avoid the gain saturation of the PD when high-power light Fresnel-reflected at the FUT end (without the bending loss) was returned. When > 6-dB bending loss is applied, this attenuator can be removed, which will lead to drastic enhancement of the SN ratio. Fig. 3.2.23(b) shows the BFS distributions measured when the applied strains were 0.15, 0.20, and 0.27 %. As shown in the inset, the BFS was linearly dependent on the applied strain with a proportionality coefficient of approximately 491 MHz/%, which was in good agreement with the previous report [35]. Thus, we clarified that the ghost peak needs to be sufficiently suppressed to perform a correct distributed measurement using BOCDR.

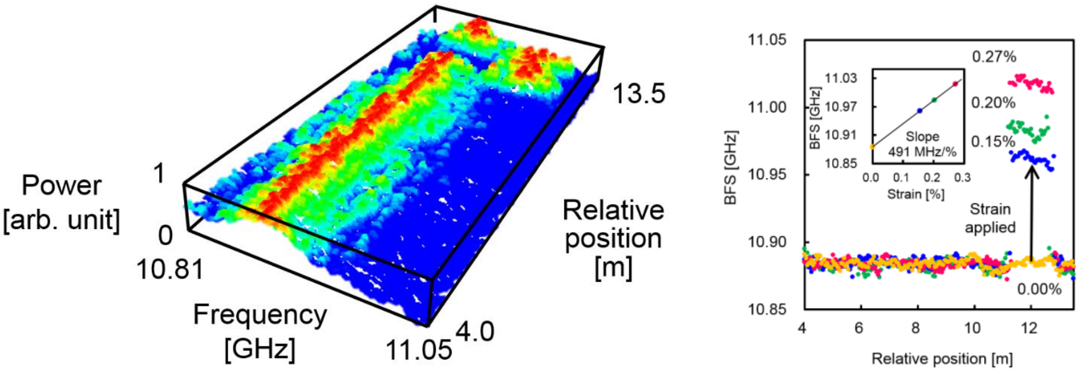

(a) (b)

Fig. 3.2.23. (a) BGS distribution measured when 6-dB bending loss was applied near the FUT end. A strain of 0.20 % was partially applied to the FUT. (b) BFS distributions measured when the applied strains were 0.15, 0.20, and 0.27 %.

3. 2. 5 Conclusion

First, we developed simplified (S-) BOCDR, where the light Fresnel-reflected at a partial reflection point (or the fiber end) was used as reference light and an additional reference path used in standard implementations can be removed. This configuration was useful for practical application and enhancement of SNR in BOCDR. Then, we implemented S-BOCDR using a POF as a fiber under test, which provides the following advantages over S-BOCDR using a standard silica single-mode fiber (SMF): (1) the Fresnel-reflected light can be stably returned at the interface between the POF and an SMF (the pigtail of an optical circulator), and (2) the effect of the 0th correlation peak can be easily and effectively suppressed by exploiting a so-called BFS-hopping phenomenon. We then experimentally demonstrated a distributed measurement and detected a 0.46-m-long heated POF section.

4 Relevant work for performance improvement of POF-based Brillouin sensors

In this chapter, first, we characterized stimulated Brillouin scattering (SBS) in POF. Second, we observed Brillouin gain spectrum (BGS) in tapered POF. Third, we propose a method for fast flaw detection in POF using infrared thermometry. Forth, we estimated Brillouin properties in poly(methyl methacrylate)-based (PMMA-) POFs by acoustic velocity measurement.

4. 1 Characterization of stimulated Brillouin scattering in POFs

In this Section, we observe stimulated Brillouin scattering (SBS) in polymer optical fibers (POFs) using pump-probe technique without lock-in detection, and fully investigate the dependences of the Brillouin gain spectrum on POF length, pump power, probe power, and temperature. Since the POF has relatively high propagation loss of 250 dB/km at 1.55 μm, an optimal POF length exists for SBS observation, which is found to be approximately 3.8 m with 21.1-dBm pump and 22.2-dBm probe waves. As the probe and pump powers are increased, the Stokes power is also raised but nonlinearly. The temperature dependence of the Brillouin frequency shift is –4.02 MHz/K, which agrees well with the previous report. These results indicate that the Brillouin signal in POFs observed with this technique can be directly applied to the development of POF-based Brillouin optical time-domain analysis systems for high-precision temperature sensing.

4. 1. 1 Introduction

In this Section, considering the relatively small Brillouin signal in POFs because of their large core diameter and multimode nature, stimulated Brillouin scattering (SBS)-based analysis systems are preferable to spontaneous Brillouin scattering (SpBS)-based reflectometers. Although each analysis system has its own advantages and disadvantages, here we focus on BOTDA, which is most widely used in the world. SBS in POFs was already observed with so-called pump-probe technique [145], but, since the experimental setup included a lock-in detector, it was not directly applicable to standard BOTDA systems. As is well known, lock-in detection enables us to measure very small alternating-current (AC) signals based on a technique known as phase-sensitive detection to single out the component of the signal at a specific reference frequency and phase. The reason for the difficulty in observing SBS in POFs without lock-in detection has been clarified to originate not from their structural problems (large core diameter etc.) but from their physical problems (high propagation loss etc.) [163]. Here we should note that researchers have tried to detect SBS signals using a 100-m-long PFGI-POF, but to no effect [163].

In this Section, we observe SBS in POFs, for the first time, using the pump-probe technique without lock-in detection, and fully investigate the dependences of the Brillouin gain spectrum (BGS) on POF length, pump power, probe power, and temperature. The optimal POF length for SBS observation is found to be approximately 3.8 m when the probe and pump powers are 21.1 dBm and 22.2 dBm, respectively. The Stokes power is raised nonlinearly with increasing probe and pump powers. The temperature dependence of the BGS is also measured. These results will be significant information in developing POF-based BOTDA systems.

4. 1. 2 Experimental setup

We employed nine kinds of PFGI-POFs with the lengths ranging from 0.3 to 50 m as fiber under tests (FUTs), all of which had numerical aperture (NA) of 0.185, core diameter of 50 μm, cladding diameter of 750 μm, core refractive index of approximately 1.35, and propagation loss of approximately 250 dB/km at 1.55 μm. Both ends of the FUTs were connected to silica SMFs with multimode fiber (MMF)-assisted coupling technique [147], which can mitigate the damage or burning at the POF/SMF interfaces. Two 1-m-long silica MMFs with BFS of approximately 10.4 GHz [163] at room temperature were inserted, which have practically no influence on the observation of the BGS in the POFs.

The experimental setup for observing SBS with the pump-probe technique is schematically shown in Fig. 4.1.1 Two laser diodes (LDs) at 1.55 μm were used as light sources; one (Santec, TSL-210) was for providing a pump wave, and the other (NEC,

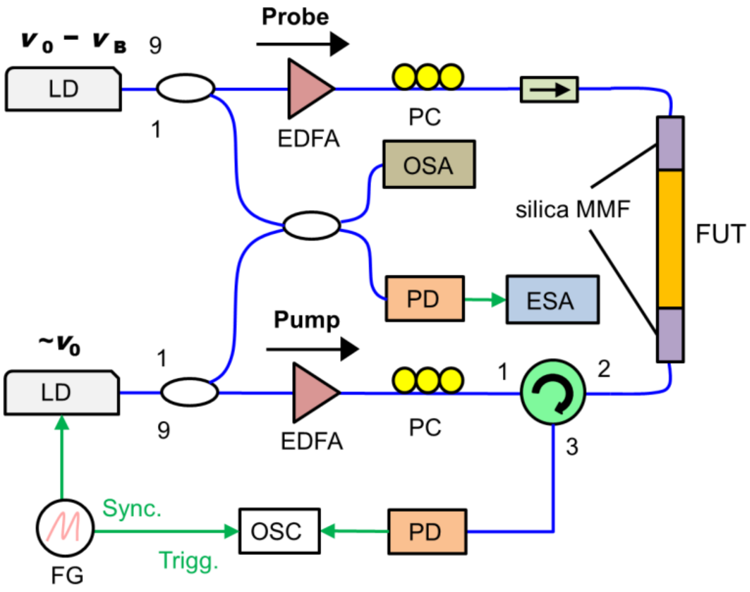

Fig. 4.1.1 Experimental setup for observing SBS in POF with pump-probe technique. EDFA, erbium-doped fiber amplifier; ESA, electrical spectrum analyzer; FG, function generator; FUT, fiber under test; LD, laser diode; OSA, optical spectrum analyzer; OSC, oscilloscope; PC, polarization controller; PD, photo-detector.

NX8562LB) was for a probe wave. The center frequency of the pump wave was swept from $\nu_0 - 1.3$ GHz to $\nu_0 + 1.3$ GHz by modulating the LD driving current with a saw-tooth waveform at 80 Hz (ν_0 is the center frequency with no modulation appied) provided by a function generator (NF Electronic Instruments, 1930A). The center frequency of the probe wave was fixed at ν_0 – BFS. Small fractions (10 %) of the pump and probe waves were coupled, and their beat signal was divided equally and monitored with an optical spectrum analyzer (OSA) (Anritsu, MS9710A) and after the signal was converted into an electrical signal with a photo-detector (PD) (Discovery Semiconductors, DSCR 402; bandwidth, 10 GHz; saturation power, 7 dBm), an electrical spectrum analyzer (ESA) (Anritsu, MS2663C) for rough and precise adjustment of their relative frequency, respectively. The pump wave was amplified with an erbium-doped fiber amplifier (EDFA) (Luxpert, LXI 2000), polarization-adjusted with a polarization controllor (PC), and injected into one end of the FUT. The probe wave was also amplified, polarization-adjusted, and injected into the other end of the FUT. The Stokes wave was directed through an optical circulator to a PD (New Focus, 2053; bandwidth, 10 MHz; saturation power, 10 mW), converted into an electrical signal, and monitored as a BGS with an oscilloscope (OSC) (Tektronix, TDS 3014B) triggered by the LD current modulation.

4. 1. 3 Experimental results

Fig. 4.1.2 shows the measured BGS in a 3.8-m-long POF. The pump and probe powers were 21.1 and 22.2 dBm, respectively. The vertical axis was normalized so that the peak Stokes power was 1.0. Despite the relatively short POF length, a clear BGS was observed even without temporal averaging (sampling rate was 80 Hz in this measurement), which is desirable for future applications to averaging-free BOTDA systems. The BFS was approximately 2.80 GHz, which is slightly lower than the previously reported value of 2.83 GHz [140], probably due to the difference in room temperature [141]. The ripples on the noise floor are probably caused by the interference of the waves Fresnel-reflected at the POF/MMF and MMF/SMF interfaces.

Since SBS in POFs has been shown to be influenced by their physical properties, including high propagation loss [163], the POF length is one of the most important parameters to be optimized to obtain a large SBS signal. Fig. 4.1.3 shows the BGS dependence on POF length with 32-times averaging. The Stokes power was drastically changed according to the POF length. The Stokes power dependence on the POF length is shown in Fig. 4.1.4. The maximum Stokes power was observed at the POF length of 3.8 m. Here, the optimal POF length exists because, as the POF length is longer, the

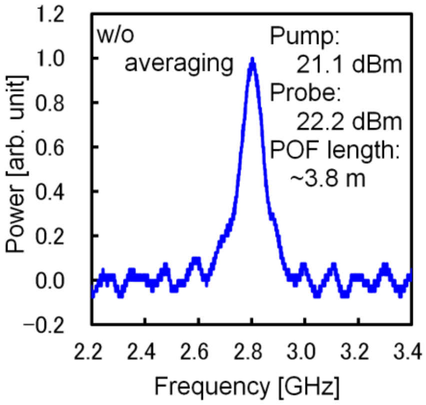

Fig. 4.1.2 Measured BGS in 3.8-m-long POF without averaging.

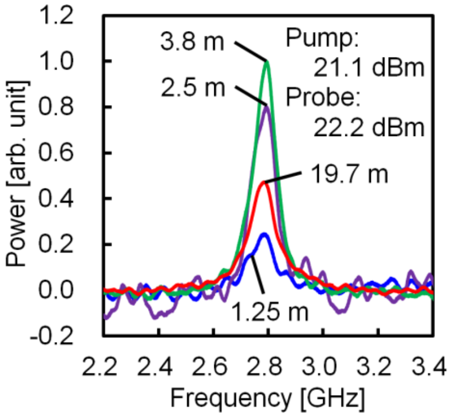

Fig. 4.1.3 Measured BGS dependence on POF length.

Brillouin effective length also becomes longer (leading to higher Stokes power) but the pump and probe waves suffer from more significant attenuation. We predict that the optimal POF length can be elongated by employing the pump and probe waves with much higher powers.

The BGS dependence on probe power in the 10-m-long POF was measured when the pump power was fixed at 21.1 dBm, as shown in Fig. 4.1.5. Averaging was performed 32 times. With increasing probe power, the Stokes power was raised, verifying that this BGS originates from the pump-probe interaction, i.e., SBS. The Stokes power dependence on probe power is shown in Fig. 4.1.6 The Stokes power began to increase rapidly at the probe power of approximately 20 dBm; this behavior seems to be due to the pump

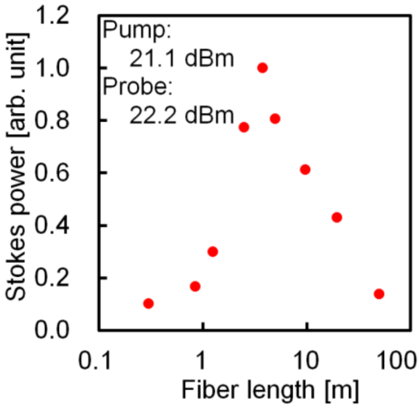

Fig. 4.1.4. Stokes power dependence on POF length.

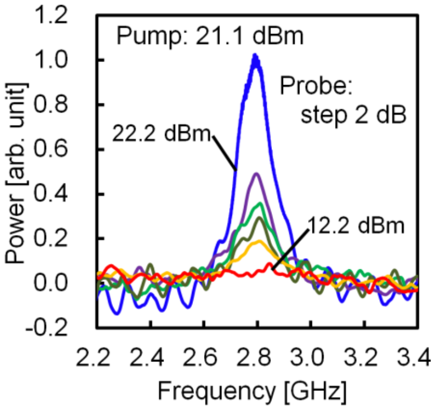

Fig. 4.1.5 Measured BGS dependences on probe power.

depletion [1]. The Stokes power was also measured as a function of pump power as shown in Fig. 4.1.7, where the vertical axis was normalized so that the Stokes power with 24.8-dBm pump was 1.0. The probe power was fixed at 20.5 dBm. With increasing pump power from 0 dBm, the Stokes power was gradually enhanced; and it also began to increase rapidly when the pump power was higher than approximately 20 dBm, which is much lower than the theoretical Brillouin threshold without the pump-probe technique (approximately 53.8 dBm [15]). These results suggest that the pump and probe waves with the powers of higher than approximately 20 dBm should be used to efficiently induce SBS in POFs with this technique.

We also measured the temperature dependence of the BGS in the 10-m-long POF, as

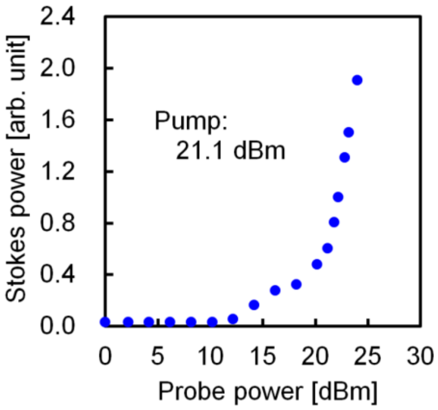

Fig. 4.1.6 Stokes power dependence on probe power.

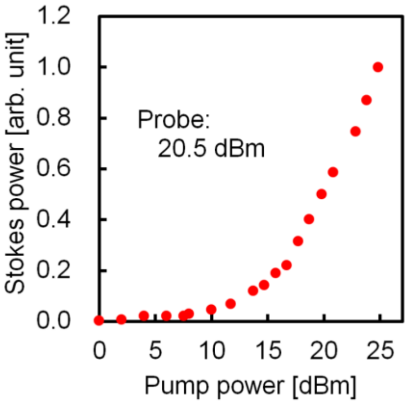

Fig. 4.1.7 Stokes power dependence on pump power.

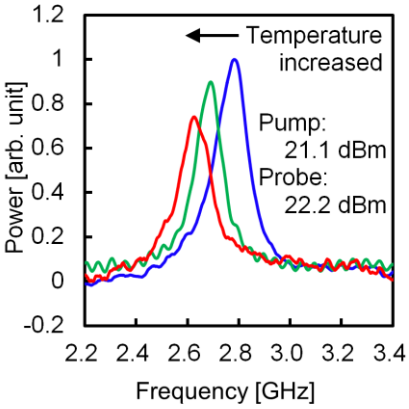

Fig. 4.1.8 Measured BGS dependence on temperature.

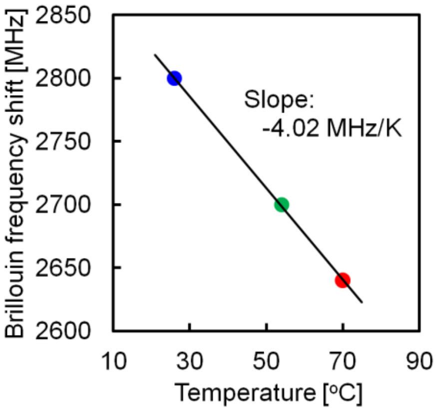

Fig. 4.1.9 BFS dependence on temperature.

shown in Fig. 4.1.8. The temperature was set to 25, 55, and 70°C. Averaging was performed 32 times. With increasing temperature, the BGS shifted toward lower frequency. The Stokes power was decreased most likely due to the polarization fluctuations and the non-uniform temperature distribution along the POF. Fig. 4.1.9 shows the temperature dependence of the BFS. Note that the dependence is well known to be linear in the range from 20 to 80°C [141,145]. The slope of −4.02 MHz/K is in good agreement with the previously reported values [141,145], which means that the BGS in POFs observed with this technique can be directly applied to high-precision temperature sensing.

4. 1. 4 Conclusion

SBS in POFs was observed, for the first time to the best of our knowledge, using the pump-probe technique without lock-in detection, and the dependences of the BGS on POF length, pump/probe powers, and temperature were fully investigated. We clarified that the optimal POF length for SBS observation is 3.8 m when the probe and pump powers are 21.1 dBm and 22.2 dBm, respectively. This length can be, we predict, elongated by the pump and probe waves with much higher powers. We also showed that the Stokes power was raised nonlinearly with increasing probe and pump powers, and that >20-dBm power is required for both pump and probe waves to efficiently induce SBS in POFs. In addition, the BFS dependence on temperature was measured to be −4.02 MHz/K, which was in good agreement with previous experiments. We believe that these results will offer a crucial basis for implementing distributed Brillouin sensors (especially, BOTDA systems) based on POFs with extremely high flexibility.

4. 2 Estimation of Brillouin properties in PMMA-POFs

In this Section, first, in order to confirm the validity of this method, we show that the estimated BFS of a PFGI-POF of approximately 2.9 GHz at 1.55 μm moderately agrees with the actual value previously reported. Then, we measure the acoustic velocity in a poly(methyl methacrylate)-based (PMMA-) POF with a 980 μm core diameter to be 2.8 × 10^3 m/s, from which its BFS is estimated to be approximately 5.4 GHz at 1.55 μm and approximately 13 GHz at 650 nm. We also find that the BFS varies linearly depending on temperature with a coefficient of approximately –17 MHz/K at 650 nm pump. Since this value is –7.1 times larger than that of silica fibers at 650 nm (2.4 MHz/K), and is even 1.7 times larger than that of PFGI-POFs at 650 nm (–10.0 MHz/K), we think that PMMA-

POFs are potentially applicable to high-precision temperature sensing.

4. 2. 1 Introduction

Up to now, the dependences of the BFS on strain and temperature in the PFGI-POF at 1.55 μm have been investigated [140], and it has been found that Brillouin scattering in PFGI-POFs has a big potential for use in the development of high-precision temperature sensors with reduced strain sensitivity [141]. However, Brillouin scattering in standard PMMA-POFs has not been experimentally observed yet for the following two reasons: (1) it is difficult to develop a Brillouin monitoring system including an optical amplifier, optical circulator, etc., at 650 nm, where the propagation loss is minimal, and (2) their core diameter is so large (typically 980 μm) that the Brillouin threshold power is extremely high. We believe that clarification of the Brillouin scattering properties in PMMA-POFs is as significant as that in PFGI-POFs, since PMMA-POFs are much more cost-effective and more widely used in communication applications.

In this Section, first, we measure the acoustic velocity in POFs using ultrasonic pulse-echo technique, and estimate their BFSs. First, in order to confirm the validity of this method, we show that the estimated BFS of a PFGI-POF of approximately 2.9 GHz at 1.55 μm moderately agrees with the actual value previously reported. Then, we measure the acoustic velocity in a PMMA-POF with a 980 μm core diameter to be 2.8×10^3 m/s, from which its BFS is estimated to be approximately 5.4 GHz at 1.55 μm and approximately 13 GHz at 650 nm. We also find that the BFS varies linearly depending on temperature with a coefficient of approximately –17 MHz/K at 650 nm pump. Since this value is –7.1 times larger than that of silica fibers at 650 nm (2.4 MHz/K), and is even 1.7 times larger than that of PFGI-POFs at 650 nm (–10.0 MHz/K), we think that PMMA-POFs are potentially applicable to high-precision temperature sensing. Finally, we find that the BFS varies nonlinearly depending on strain, which seems to be caused by the elastic-to-plastic transition of PMMA.

4. 2. 2 Experimental setup

First, we employed two kinds of POF samples. One was a PFGI-POF with numerical aperture (NA) of 0.185, core diameter of 120 μm, cladding diameter of 490 μm, core refractive index of approximately 1.35, and propagation losses of approximately 150 dB/km at 1.55 μm and approximately 100 dB/km at 650 nm. The other sample was a PMMA-POF with NA of 0.5, core diameter of 980 μm, cladding diameter of 1000 μm, core refractive index of approximately 1.49, and propagation loss of approximately 150 dB/km at 650 nm (extremely high loss at 1.55 μm) and tolerable temperature range from −55 to 70°C. The lengths of the PFGI-POF and PMMA-POF were 4.2 and 3.9 mm as shown in Figs. 4.2.1(a) and (b), respectively.

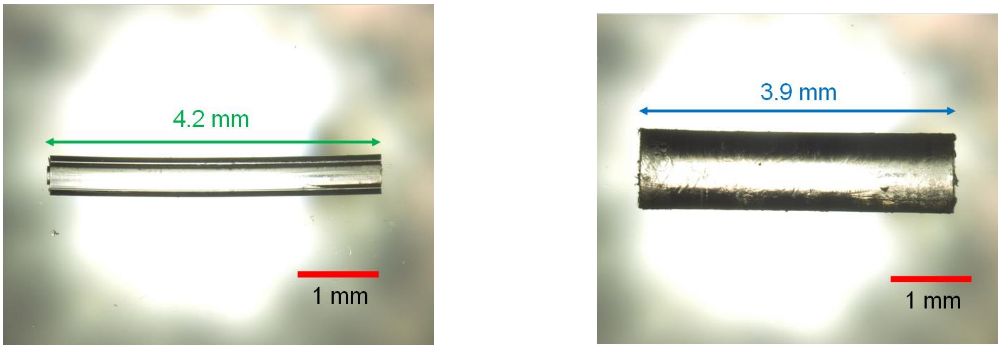

(a) (b)

Fig. 4.2.1 Microscope images of (a) the PFGI-POF sample and (b) the PFGI-POF sample.

The entire measurement setup is depicted in Fig. 4.2.2. The ultrasonic pulse generated with an unfocused transducer (Panametrics M316) connected to a pulser-receiver (Panametrics 5900PR) was directed to the POF samples fixed in degassed water, and the reflected wave was received with the same transducer. The center frequency of the pulse was 10.0 MHz, and the diameter of the ultrasonic beam was 3.2 mm.

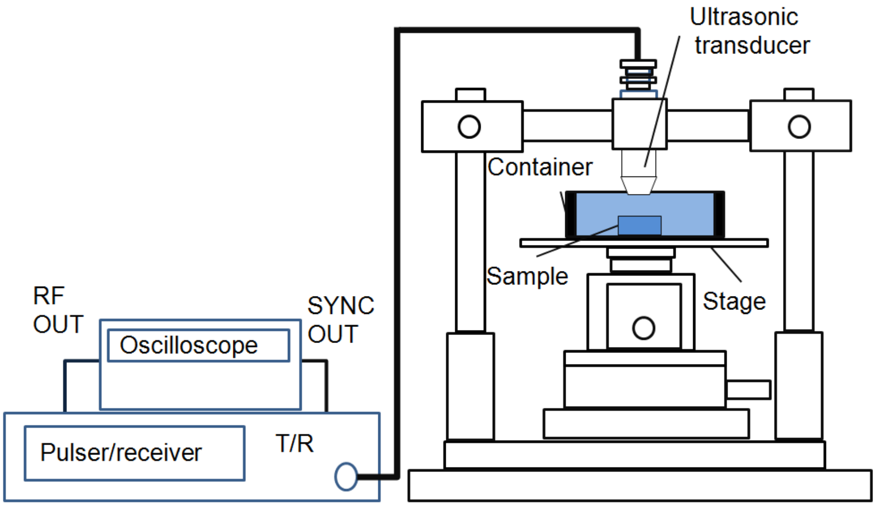

Fig. 4.2.2 Entire experimental setup
for measuring the acoustic velocity in POFs.

The magnified view around the transducer when the POF samples were not employed is schematically shown in Fig. 4.2.3. The aluminum (Al) plate had a hole of approximately 1 mm diameter to fix the PMMA-POF. The magnified views with the PFGI- and PMMA-POF samples employed are depicted in Figs. 4.2.4(a) and (b), respectively. The PFGI-POF was perpendicularly placed on the Al plate, while the PMMA-POF was fixed perpendicularly to the Al plate by making use of the hole.

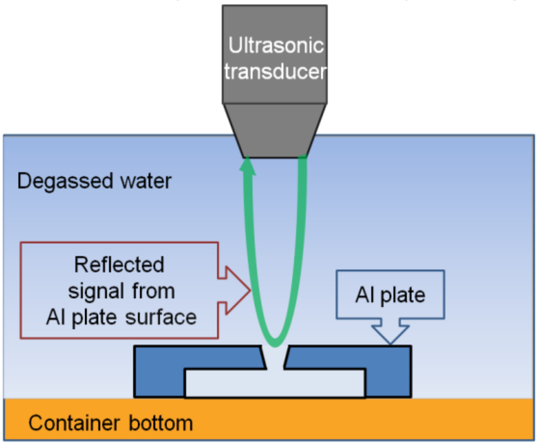

Fig. 4.2.3 Schematic setup without the POF samples.

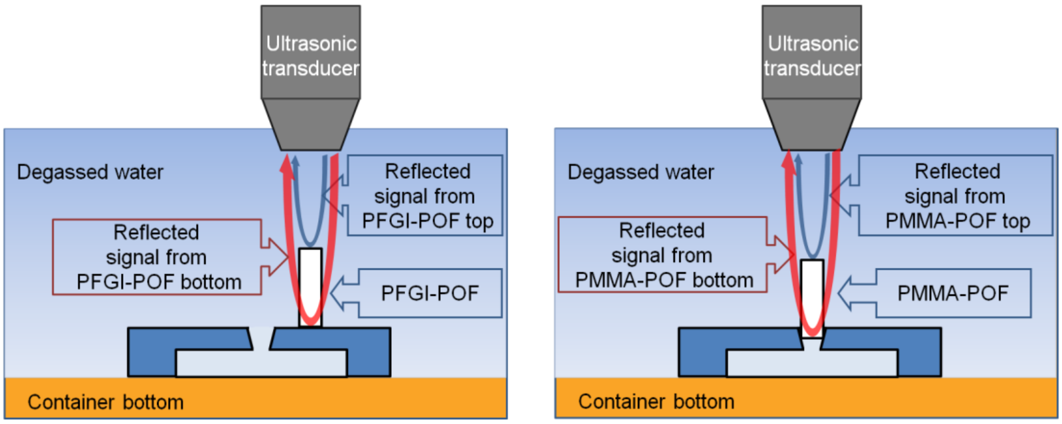

(a) (b)

Fig. 4.2.4 Schematic setups (a) with the PFGI-POF sample and (b) with the PMMA-POF sample.

Then, the POF samples used to measure the strain dependence were fabricated using the following procedure: (1) measure the stress-strain curve of the POFs and obtain their fracture strain ε_f, (2) keep strains of 2-40% ($<\varepsilon_f$) applied to the POFs for 15 min so that they do not relax to the initial length [126], and (3) cut the elongated POFs into samples of several mm length.

4. 2. 3 Experimental results

First, Fig. 4.2.5(a) shows the measured echo waveform without the POF sample. The first signal, where the time delay t was defined as 0 μs, represents the launched wave. Several large peaks observed at $t > 11.8$ μs are due to the reflection from the Al plate. The first peak (A) at t approximately 11.8 μs and the second peak (B) at t approximately 12.4 μs correspond to the reflected waves at the surface and bottom of the Al plate, respectively. Other peaks (C) following them at $t > 13.0$ μs are due to the multiple reflection in the Al plate. Fig. 4.2.5(b) shows the measured echo waveform with the 4.2 mm PFGI-POF sample employed. By comparing Figs. 4.2.5(a) and 4.2.5(b), we know that the two peaks at t approximately 6.4 μs and at t approximately 11.4 μs correspond to the reflected waves at the surface and bottom of the PFGI-POF, respectively. The peak at t approximately

11.4 μs was much smaller than the peak (A) at *t* approximately 11.8 μs because of the small core area and low acoustic reflectivity of the PFGI-POF/water boundary compared with those of the water/Al boundary. From the magnified view around these two peaks, the exact time delay was found to be 4.98 μs, and the acoustic velocity v_A was calculated to be approximately 1.7×10^3 m/s. By substituting this value in eq. (1.1), with the pump wavelength of 1.55 μm, its BFS was estimated to be approximately 2.9 GHz, which is in moderate agreement with the previously reported value of 2.83 GHz [140]. Though this discrepancy seems to be caused by the insufficient resolution in calculating v_A, it was shown that this method can be used to roughly estimate the BFS. When the pump wavelength was 650 nm, where the propagation loss in PMMA-POFs is minimal, the BFS in the PFGI-POF was estimated to be approximately 7.0 GHz.

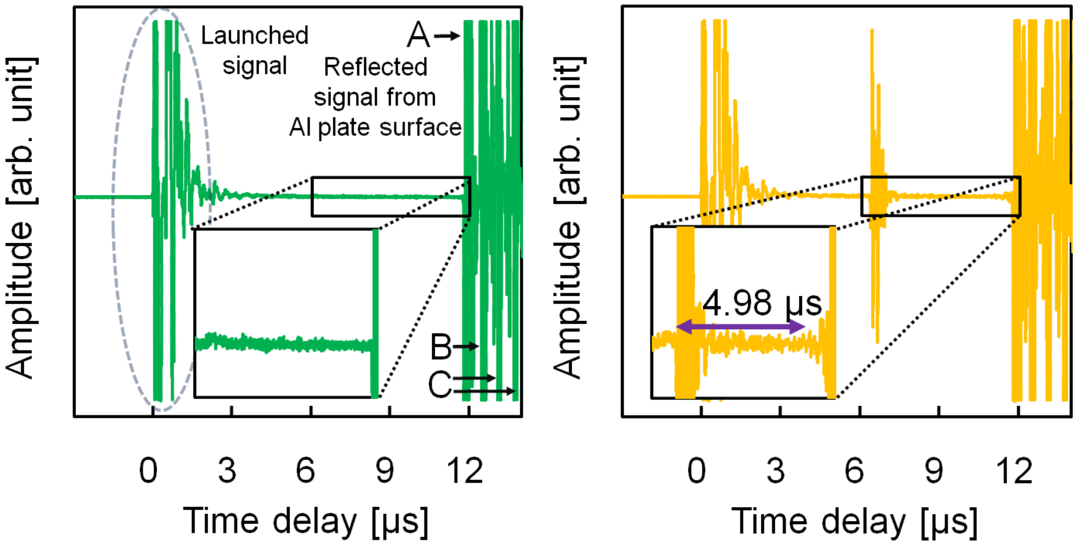

(a) (b)

Fig. 4.2.5 Measured echo waveforms (a) without and (b) with the PFGI-POF sample.

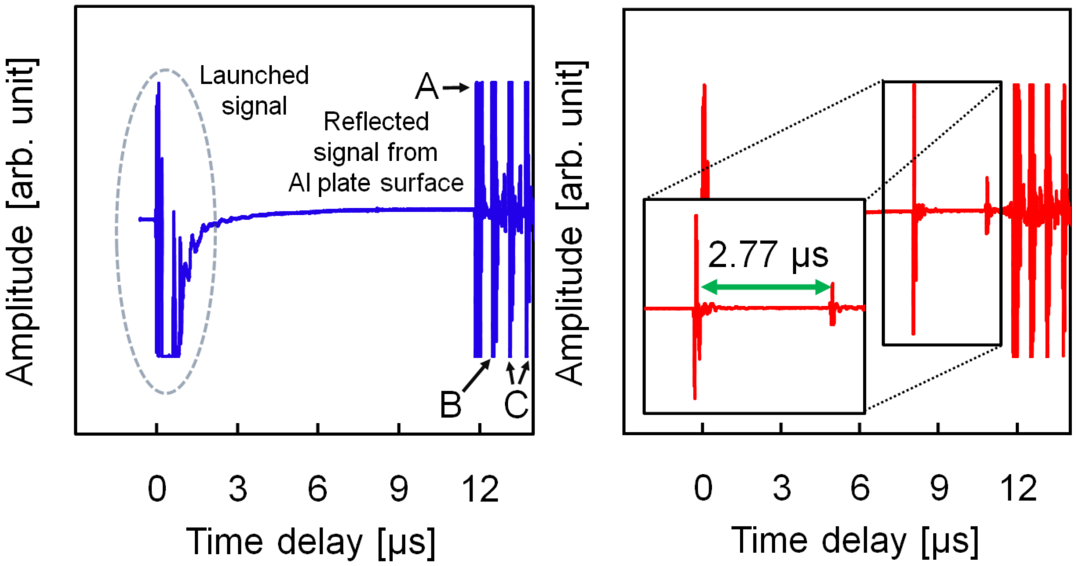

(a) (b)

Fig. 4.2.6 Measured echo waveforms (a) without and (b) with the PMMA-POF sample.

Next, we measured the acoustic velocity in the PMMA-POF and estimated its BFS. Fig. 4.2.6(a) shows the measured echo waveform without the PMMA-POF sample, which can be interpreted in the same way as Fig. 4.2.5(a). The positions of the peaks (A, B, and C) differed from those in Fig. 4.2.6(a), because the vertical position of the transducer was slightly lower. The measured echo waveform with the 3.9 mm PMMA-POF sample employed is shown in Fig. 4.2.1 (b). By comparing Figs. 4.2.6(a) and 4.2.6(b), it is clear that the two peaks at *t* approximately 8 µs and at *t* approximately 11 µs correspond to the reflected waves at the surface and bottom of the PMMA-POF, respectively. The exact time delay was measured to be 2.77 µs, and the acoustic velocity v_A in the PMMA-POF was calculated to be 2.8×10^3 m/s, which is nearly comparable to the acoustic velocity of 2644 (+/– 25) m/s in bulk PMMA [164]. Its BFS at 650 nm was also estimated to be approximately 13 GHz, which is close to approximately 11 GHz of silica fibers at 1.55 µm [34]. In contrast, its BFS at 1.55 µm was estimated to be approximately 5.4 GHz, which is about twice of 2.83 GHz in PFGI-POFs at 1.55 µm.

The estimated BFS dependence on temperature in the PMMA-POF at 650 nm pump is shown in Fig. 4.2.7. The temperature was increased from 26 to 60°C. We did not take into account the refractive-index dependence on temperature, because its coefficient in bulk PMMA is reported to be as small as -1.2×10^{-4} K^{-1} [164]. The BFS was estimated to vary linearly depending on temperature with a coefficient of –17 MHz/K within this temperature range, which is –7.1 times larger than that of silica fibers at 650 nm (2.38 MHz/K) [35] and is even 1.7 times larger than that of PFGI-POFs at 650 nm (−10.0 MHz/K) [127]. Therefore, compared with silica fibers and PFGI-POFs, PMMA-POFs can be potentially applied to high-precision temperature sensing.

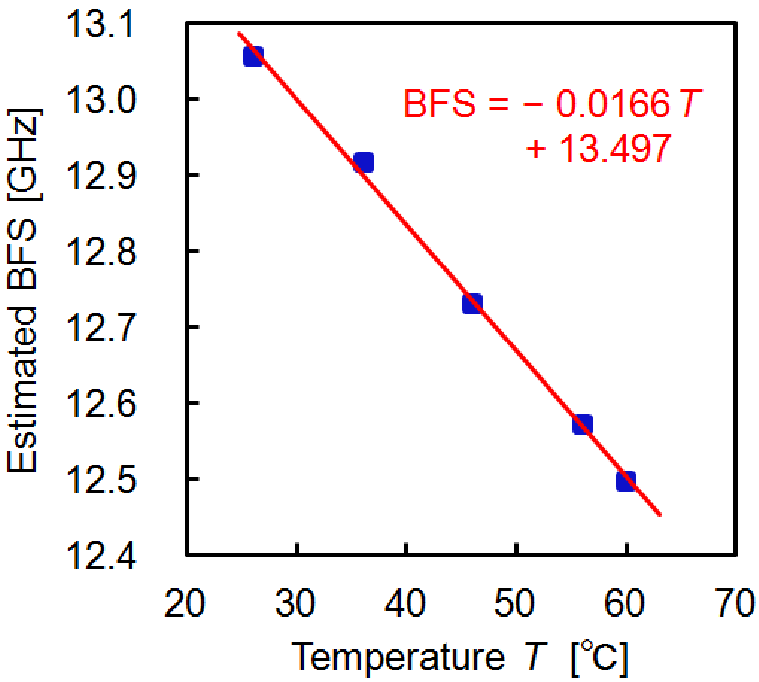

Fig. 4.2.7. Estimated BFS dependence on temperature in the PMMA-POF at 650 nm.

Then, Fig. 4.2.8 shows the stress-strain curve of one of the PMMA-POFs. Upper and lower yield points were observed at 4.5 and 22%, respectively, and the fracture strain was 55%. This stress-strain curve indicates that the elastic-plastic transition of the PMMA-

POF is induced at several % strain. Such stress-strain curves were also measured while each POF sample was being fabricated, as shown in Fig. 4.2.9. It is clear that, for each POF sample, residual strain exists even after it is released. Since the residual strain is slightly lower than the target strain, we define, for clarity, the residual strain as the "applied strain" in the next experiment.

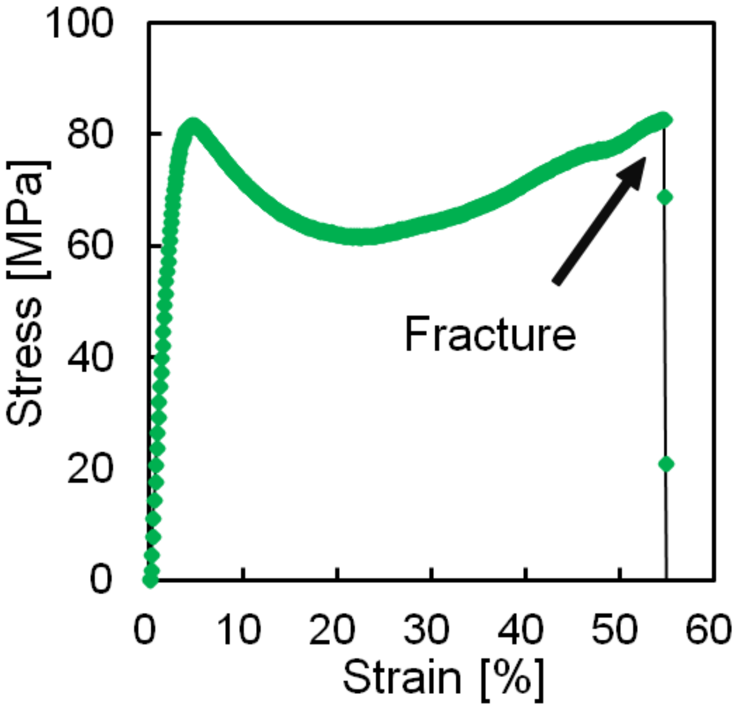

Fig. 4.2.8 Stress-strain curve in the PMMA-POF.

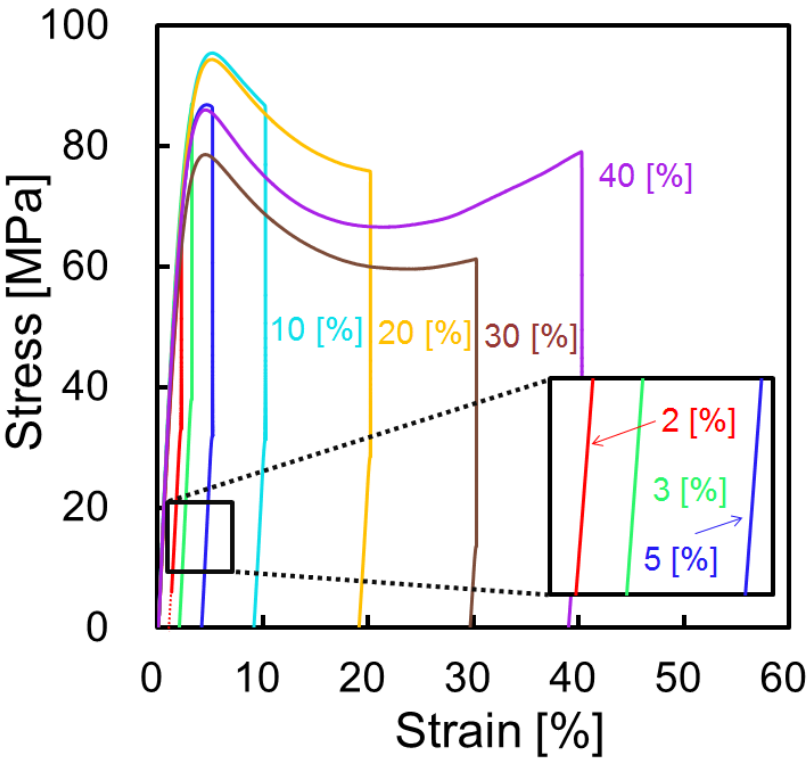

Fig. 4.2.9 Stress-strain curve for the fabrication of each POF sample. The inset shows a magnified view.

Finally, Fig. 4.2.10 shows the estimated BFS dependence on applied strain in the PMMA-POFs at 650 nm pump. The refractive index *n* was assumed to be constant (1.49), and the temperature was kept at 19°C. The BFS dependence on applied strain showed a nonlinear behavior; its coefficient was positive within the strain ranges of 0-approximately 10% and approximately 20-approximately 40%, but was negative within the range of approximately 10-approximately 20%. This feature is similar to that of the stress-strain curve shown in Fig. 4.2.8, probably originating from the transition of PMMA from the elastic to the plastic regime. Further study is, however, needed to clarify this point. While the sign of the strain coefficient of the PMMA-POFs around 0% applied strain was positive, that of PFGI-POFs is reported to be negative [141]. This difference indicates that the strain coefficient of POFs for small strain can be controlled, including its sign, by fluorine doping; thus, we can expect that high-precision temperature sensing with zero strain sensitivity can be achieved by optimizing the fluorine doping concentration.

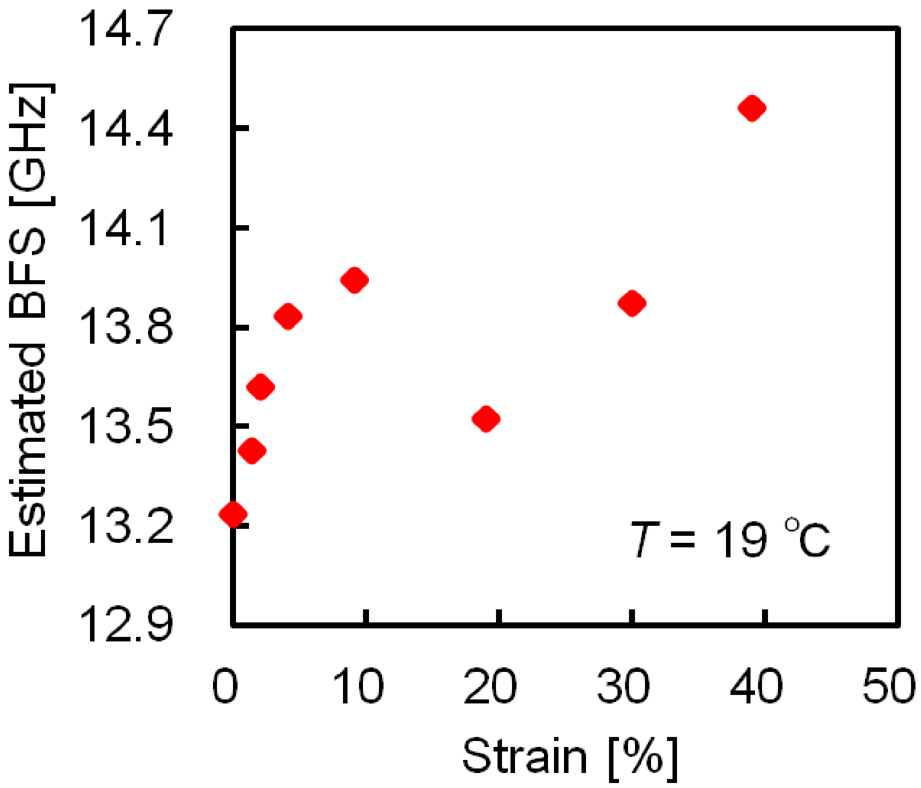

Fig. 4.2.10 Estimated BFS dependence on strain in the PMMA-POF at 650 nm.

4. 2. 4 Conclusions

First, the acoustic velocities in POFs were measured based on the ultrasonic pulse-echo technique for the estimation of their BFS. First, the BFS of a PFGI-POF at 1.55 μm was estimated to be approximately 2.9 GHz. This value moderately agreed with the actual value previously reported, indicating that this method can be used to roughly estimate the BFS. Then, the acoustic velocity in a PMMA-POF with 980 μm core diameter was measured to be 2.8 × 10^3 m/s, from which its BFS was estimated to be approximately 13 GHz at 650 nm and approximately 5.4 GHz at 1.55 μm. Next, the BFS dependences on temperature and strain in PMMA-POFs were estimated using ultrasonic pulse-echo technique. We found that the BFS varies linearly depending on temperature with a coefficient of approximately –17 MHz/K at 650 nm pump. Since this value is –7.1 times larger than that of silica fibers at 650 nm, and is even 1.7 times larger than that of PFGI-POFs at 650 nm, PMMA-POFs appear to be a good candidate for Brillouin-based temperature sensing with high precision. We also found that, in contrast, the BFS varied nonlinearly depending on applied strain, which seems to be related to the elastic-to-plastic transition of PMMA. More accurate estimation will be feasible by taking the refractive-index dependence on strain into consideration. We believe that this information will be useful in developing temperature/strain sensors based on Brillouin scattering in POFs with high flexibility, low cost, easy connection, high safety, and memory effect.

4. 3. Fast flaw detection in POF using infrared thermometry

In this Section, we demonstrate a fast and cost-effective method of detecting flaws in polymer optical fibers (POFs) using an infrared thermometer. The optical loss dependence of the measured temperature at the flaw is found to be linear with a proportionality constant of approximately 0.74 °C/dB when the propagating light is 24.5 dBm (282 mW) at 1.55 μm. The propagating optical power dependence of the measured temperature at the flaw with a fixed loss also shows a linear behavior, which predicts that a high optical input power is preferable to precise estimation of the loss.

4. 3. 1 Introduction

The fabrication technology of widely used silica single-mode optical fibers (SMFs) has matured sufficiently to keep their quality extremely high and stable; and as a result, km-order-long silica SMFs with a propagation loss of as low as 0.2 dB/km at 1.55 μm are common [7]. In contrast, the fabrication technology of polymer optical fibers (POFs) is relatively new. Currently, polymethyl methacrylate (PMMA)-based POFs can be fabricated with a stable propagation loss owing to their large core diameters of up to 980 μm [124]. However, the propagation loss of perfluorinated graded-index (PFGI-) POFs with core diameters of as small as 50 μm, which have become commercially available only recently, is largely influenced by the flaw in the core induced during the fabrication process, resulting in the difficulty in producing long PFGI-POFs with stable quality [144]. Such PFGI-POFs with a length of one hundred meters or longer are now highly demanded not only in POF-based high-capacity transmission systems but also in next-generation distributed sensors exploiting nonlinear effects in POFs. Thus, to develop an effective method of detecting flaws in PFGI-POFs is of substantial significance.

Conventional methods for detecting flaws in optical fibers include optical time-domain reflectometry (OTDR) [165,166], optical low-coherence reflectometry (OLCR) [167,168], and optical frequency-domain reflectometry (OFDR) [169,170]. They can measure the accurate loss distribution along the POFs with a high spatial resolution, but suffer from some drawbacks, such as high installation cost required for the devices (photodetectors, specially configured lasers, etc.), long measurement time for signal processing, and the inability to resolve the flaw location at a glance in long POFs.

In this Section, a fast and cost-effective method of detecting flaws in POFs using an infrared thermometer (IRT) is demonstrated, which can overcome the disadvantages of the conventional techniques. Since an optical loss at a flaw in a POF induces the rise in temperature, the loss distribution along a POF can be detected with the IRT as a temperature distribution. First, we show that the locations of the flaws in POFs can be detected, whether the POFs are jacketed or bare. Then, we find the optical loss dependence of the measured temperature at the flaw to be linear with a proportionality constant of approximately 0.74 °C/dB with the propagating light of 24.5 dBm (282 mW) at 1.55 μm. We also show that, when the loss is fixed, the propagating optical power dependence of the measured temperature at the flaw is linear, predicting that high-power optical power is desirable to estimate the loss precisely.

4. 3. 2 Principle

A blackbody, i.e., a perfect absorber of any radiation incident on it, is capable of emitting radiation [171]. When heated to a uniform temperature, it generates blackbody radiation, the characteristics of which are determined solely by the temperature. The total radiant emittance W of an object (both blackbody and non-blackbody) is known to be given by Stefan-Boltzmann's law as

$$W = \varepsilon \sigma T^4 \ , \tag{1}$$

where ε is the emissivity of the object (1 for a blackbody), σ is the proportionality constant, and T is the surface temperature of the object [172]. The surface temperature of an object including a POF can thus be measured with an IRT. The IRT-based method for detecting a flaw, which exploits the rise in temperature induced by an optical loss at the flaw, has such advantages as (1) cost efficiency, (2) real-time measurement, and (3) visual display of the flaw location.

4. 3. 3 Experimental setup

We employed two PFGI-POFs as fibers under test (FUTs), which had a numerical aperture of 0.185, a core/cladding diameter of 50/100 μm, a core refractive index of approximately 1.35, and a propagation loss of approximately 250 dB/km at 1.55 μm. One FUT, denoted by FUT 1, was a long jacketed PFGI-POF with an inner jacket diameter of 750 μm and an outer jacket diameter of 2.8 mm, in which a flaw had been caused probably during the fabrication process. Both of the jackets were composed of polyvinyl chloride (PVC). The other FUT, denoted by FUT 2, was a 60-cm-long bare PFGI-POF, at the middle point of which a flaw was artificially induced by repeating bending and releasing. The loss at the flaw was moderately variable from 2.5 to 20 dB. An IRT (i7; FLIR System, Inc.) was used to detect the flaws, which had a spectral range from 7.5 to 13 μm, and an image frequency of 9 Hz. The emissivity ε was set as follows: for the jacketed POF, ε = 0.98 (value for PVC [173]); for the bare POF, ε = 0.95 (value for PMMA [174,175]). The room temperature was 24°C. Note that the optical power and/or the loss at the flaw were estimated considering the optical loss caused during the light propagation from one end of the POF to the flaw.

4. 3. 4 Experimental results

First, we detected the flaw in the FUT 1 wound on a reel of 20 cm diameter. The incident optical power was 24.5 dBm (282 mW). Fig. 4.3.1(a) shows its photograph, from which no information on the flaw was derived. In its IR image shown in Fig. 4.3.1(b), however, the location of the flaw was roughly but clearly detected despite the thick jackets, which is not feasible only by detecting the scattered visible light with our naked eyes. The maximum temperature was 24.4 °C, and the high-temperature region had a tail extending toward the left. To clarify this tailing effect, we injected 21.3 dBm (135 mW) light into both ends of the FUT 2, one by one, as shown in Figs. 4.3.2(a)–(c). The optical loss of the flaw at the midpoint of the FUT 2 was fixed at 4.9 dB in this measurement. When the light was injected from the right-hand side, the high-temperature region had a tail

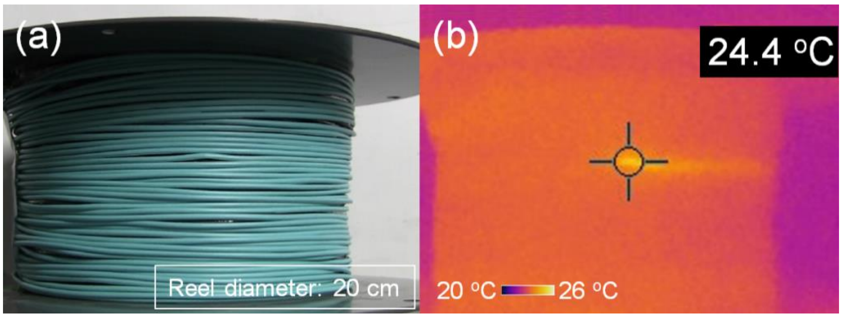

Fig. 4.3.1 (a) Photograph and (b) IR image of the jacketed POF with a flaw wound on a reel.

extending for approximately 5 cm toward the left, as shown in Fig. 4.3.2(b), and vice versa, as shown in Fig. 4.3.2(c). This phenomenon can be exploited to identify the unknown direction of the propagating light through the POF. Since the measured maximum temperature of approximately 28°C was almost the same in both configurations, the light injection only from one end of the POF appears to be sufficient for rough estimation of the optical loss at the flaw.

Next, we measured the dependence of temperature on the optical loss at the flaw when the incident optical power was fixed at 24.5 dBm (282 mW), as shown in Fig. 4.3.3. The error bars calculated from the signal fluctuations for 5 min were +/– 0.8 °C. As the loss was raised, the temperature was increased linearly with a slope of approximately 0.74 °C/dB, which is of practical use for the rough estimation of the loss using the measured temperature. We also measured the dependence of temperature on the optical power of the propagating light when the optical loss at the flaw was fixed at 20 dB, as shown in Fig. 4.3.4. As the incident power was raised, the temperature was increased almost linearly, which indicates that, by employing high-power light, the measured temperature for a certain loss can be increased. This leads to the enhancement of the proportionality constant between the measured temperature and the loss (see Fig. 4.3.3), resulting in a more precise estimation of the loss. The slight decrease in the slope observed

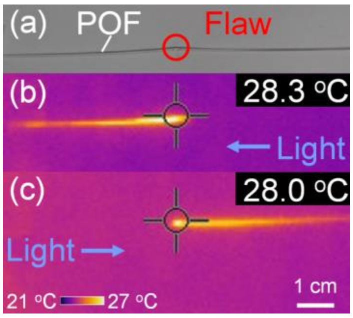

Fig. 4.3.2 (a) Photograph of the bare POF with a flaw, and its IR images with light propagating from (b) right to left, and (c) left to right.

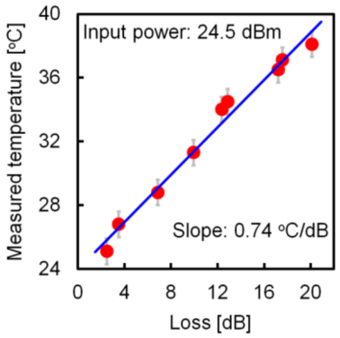

Fig. 4.3.3 Measured temperature dependence
on optical loss at the flaw.

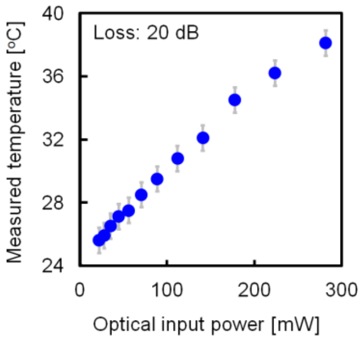

Fig. 4.3.4 Measured temperature dependence on optical power of the
propagating light at the flaw.

in the range of the optical power of >200 mW seems to be caused by the heat dissipation effect.

4. 3. 5 Conclusion

We demonstrated a fast and low-cost detection of the flaws in POFs using an IRT, which can overcome the drawbacks of the conventional techniques. The locations of the flaws were successfully detected, even when the POF was protected by thick jackets. The optical loss dependence of the temperature at the flaw was linear with a coefficient of approximately 0.74 °C/dB when the optical power was 24.5 dBm (282 mW) at 1.55 μm.

The optical power dependence of the measured temperature at the flaw with a fixed loss was also linear, which predicts that a higher optical power is desirable for the loss estimation with more precision. We hope that this method will be of common use, with its fast measurement capability, ease of handling, and cost efficiency, in examining the quality of POFs at the final stage of their fabrication process in the near future.

4. 4. Observation of BGS in tapered POF

In this Section, we report on the first observation of the Brillouin gain spectrum in a PFGI-POF tapered by a heat-and-pull technique. The Stokes power was slightly enhanced by tapering probably on account of higher optical power density in the core. In addition, the Brillouin frequency shift was decreased by approximately 40 MHz, which was experimentally verified to be partially caused by high heating temperature applied to the POF during the taper fabrication process. We anticipate that our findings will provide a basic principle of temperature sensing with “memory” function.

4. 4. 1 Introduction

Recently, Zou *et al.* [176] have investigated the BGSs in tapered SMFs at 1.55 μm, and found that the BFS in the taper waist (outer diameter: 5 μm) is higher than that of the untapered silica SMF by approximately 270 MHz. This report implies that the BFS in optical fibers can be controlled by adjusting the tapering conditions, which will increase the freedom in designing the above-mentioned fiber-optic Brillouin devices. Meanwhile, polymer optical fibers (POFs) have attracted a lot of attention because of their high flexibility, ease of handling, low-cost connection, and high safety; and tapered POFs have also been extensively studied for a variety of applications [177-182]. However, no report has been provided on the observation of Brillouin scattering in a tapered POF yet, though the Brillouin properties in untapered POFs have already been characterized. Thus, observing Brillouin scattering in a tapered POF is an important technological step toward the development of POF-based Brillouin devices with higher design freedom.

In this Session, we observe the BGS in a PFGI-POF tapered by a heat-and-pull technique for the first time. The Stokes power and the BFS in the waist (outer diameter: 223 μm) were higher and lower (by approximately 40 MHz) than those in an untapered POF, respectively. The Stokes power was enhanced because of higher optical power density in the core; whereas the BFS downshift was experimentally proved to be partially caused by the heat applied to the POF during the taper fabrication.

4. 4. 2 Experimental setup

As a POF to be tapered in the experiment, we employed not a standard PMMA-POF but a PFGI-POF. This is because Brillouin scattering has been successfully observed only in PFGI-POFs, which have a relatively low propagation loss of 250 dB/km even at

Table I. Physical properties of the POF sample

Numerical aperture	**Core diameter [μm]**	**Outer diameter [μm]**	**Core refractive index**	**Propagation loss [dB/km]**
0.185	120	490	~1.35	~250

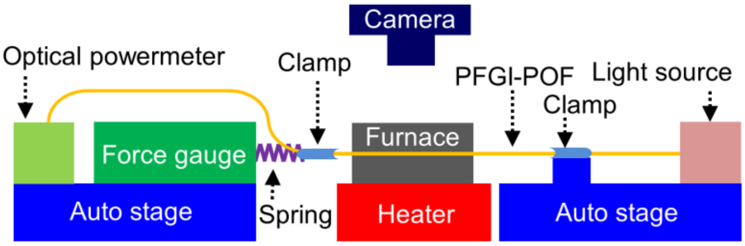

Fig. 4.4.1. Schematic setup for POF tapering by heat-and-pull technique.

telecom wavelength, where mature optical devices for Brillouin detection such as amplifiers and circulators are available. The length of the POF sample was 1.0 m, and the other physical properties are summarized in Table I. The core/cladding layers and the overcladding layer were, respectively, composed of doped/undoped amorphous perfluorinated polymers (polyperfluorobutenylvinyl ether) and polycarbonate.

A so-called heat-and-pull technique [177-181] was used to taper the POF. A chemical etching technique [182] is another well-known tapering method, but was not effective in tapering this type of POF because of the high chemical tolerance of its core material. Although the core/cladding layers and the overcladding layer were different in glass-transition temperature (< 108°C and 144°C, respectively), the heat-and-pull technique was available on account of the relatively thin overcladding layer (see Table I). Fig. 4.4.1 shows a schematic setup for tapering the POF, which contained an 80-mm-long furnace made of a U-shaped aluminum block fixed on a heater. One end of the POF was connected to a 1.55-μm light source, and the other end was to an optical powermeter. Two regions of the POF were clamped; one was fixed to a motorized stage, and the other was connected via a spring to a force gauge fixed to another stage, with which the pulling force was monitored. A digital camera was mounted on the system to measure the waist diameter of the tapered POF. After the POF was tapered, its BGS was observed based on self-heterodyne detection detailed in Ref. 140, where the polarization state was optimized with a polarization controller.

4. 4. 3 Experimental results

The furnace temperature was set to approximately 105°C, which is almost the same as the glass-transition temperature of the core. The pulling velocity was approximately 0.2 mm/s, which was adaptively controlled so that the pulling force might be constantly lower than 30 mg. The tapering process was run for approximately 9 min. Fig. 4.4.2

illustrates a schematic diagram of the tapered POF, including three microscopic images (untapered, intermediate, and waist zones). The outer diameter of the waist was 223 μm, corresponding to the core diameter of 54.6 μm, which was estimated under the assumption that the ratio of the core diameter to the outer diameter remains unaltered by tapering. The elongated POF length was 102 mm (tapered length: 182 mm), and the taper ratio [177] was calculated to be 0.46. The total optical loss of the tapered region (excluding the propagation loss) was approximately 0.8 dB, which is close to the previous report [177].

Next, we cut the tapered POF at two points indicated in Fig. 4.4.2, and used the portion

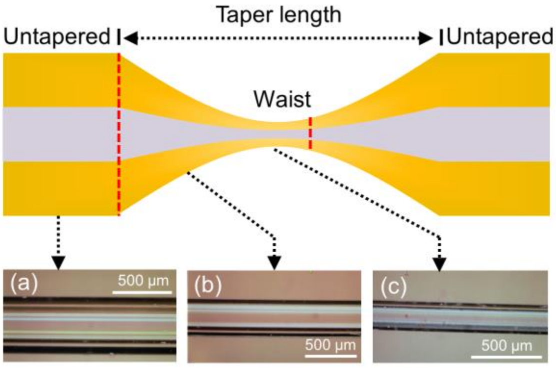

Fig. 4.4.2. Schematic structure of the tapered POF, along with the photographs of (a) untarpered, (b) intermediate, and (c) waist zones. The red dotted lines indicate the positions at which the sample was cut for Brillouin measurement.

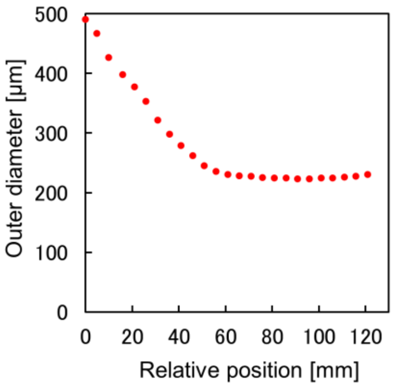

Fig. 4.4.3. Measured outer diameter as a function of relative position along the tapered POF.

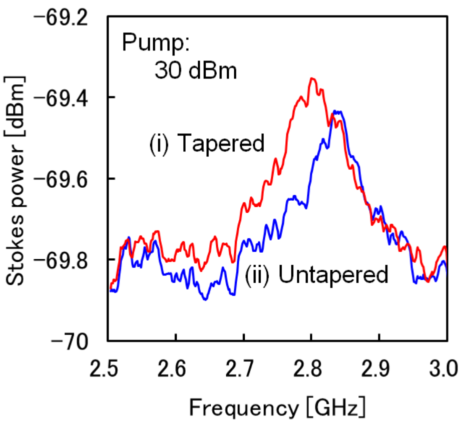

Fig. 4.4.4 Measured BGSs in POFs:
(i) tapered and (ii) untapered.

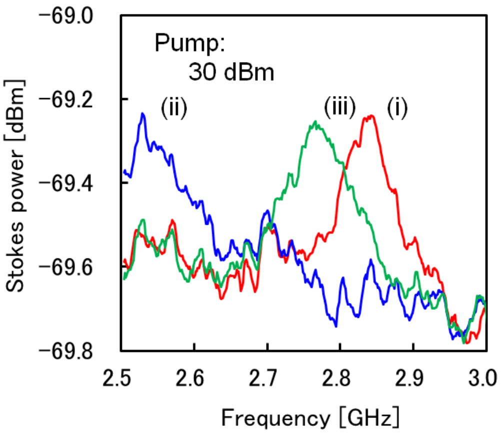

Fig. 4.4.5 Measured BGSs in POF: (i) at room temperature (15 °C), before heating; (ii) heated at 112 °C, kept for 5 min; and (iii) cooled at room temperature (15 °C), kept for 5 min.

containing the waist zone as a sample for Brillouin measurement. The length was 121 mm, and the distribution of the outer diameter along the length measured with an optical microscope is shown in Fig. 4.4.3. The outer diameter in the approximately 60-mm-long waist zone was almost constant (approximately 225 μm). One end of the sample (relative position = 0 mm in Fig. 4.4.3) was flatly polished, and butt-coupled to a silica SMF.

Fig. 4.4.4 shows the BGS of the tapered POF measured at 17 °C, in which that of the untapered POF (same length, i.e., 121 mm) is also displayed for comparison. The incident optical power was set to as high as 30 dBm (= 1 W), because the Brillouin scattering signal from such a short POF is extremely small [140]. The Stokes power of the tapered POF was only slightly (approximately 0.1 dB) higher than that of the untapered POF, which does not agree with our calculation (> 4-dB enhancement) taking optical power density into consideration; this is because the Stokes power is so small that the influence of the noise floor and the polarization-dependent fluctuations are extremely large. The BFS of the tapered POF was downshifted from that of the untapered POF by approximately 40 MHz. The sign and absolute value of this BFS shift were opposite to and smaller than that of the tapered silica SMF (approximately 270 MHz), respectively [176].

Finally, to study the origin of the BFS shift caused by tapering, we measured the BGSs in the same untapered POF sample (used as a reference in the preceding experiment) in the following three sequential conditions: (i) at room temperature (15ºC), before heating; (ii) heated at 112ºC, kept for 5 min; and (iii) cooled at room temperature (15°C), kept for 5 min. As shown in Fig. 4.4.5, the BFSs were approximately 2.84 GHz for (i), 2.53 GHz for (ii), and 2.76 GHz for (iii). As the POF sample was untapered, the approximately 80-MHz downshift of the BFS from (i) to (iii) appears to be caused not by the pulling process but by the applied high heating temperature comparable to the glass-transition temperature of the core material, which may induce polymer transformation as well as dopant diffusion. Note that such BFS shifts have not been observed in previous reports that investigate the BFS dependence on temperature ranging up to 80ºC. However, since the BFS was downshifted in this experiment by twice the amount in the tapered POF, we speculate that the amount of the BFS shift after tapering is dependent not only on the heating temperature and duration but also on mechanical deformation, on which further detailed study is required. We might control the BFS in POFs by properly adjusting these conditions in future.

4. 4. 4 Conclusion

By the heat-and-pull technique, we fabricated the PFGI-POF taper with an outer diameter of the waist of 223 μm, and successfully observed its BGS for the first time. The Stokes power was slightly enhanced by tapering probably because of higher optical power density in the core. The BFS was downshifted by approximately 40 MHz, which was experimentally shown to originate partially from the heat applied to the POF. By using the enhanced Brillouin signal in a much longer tapered POF, the signal-to-noise ratio of the POF-based distributed sensing systems could be improved. In addition, the BFS shift induced by high heating temperature might be actively utilized as a principle of the "temperature memory effect". We believe that, along with the previously-reported "strain memory effect"[126], this novel function could be of great use in implementing POF-based Brillouin devices and systems including distributed strain and temperature sensors.

4. 5. Observation of POF fuse

In this Section, we report on the observation of POF fuse phenomenon. Although optical fibers with a high transmission capacity are in demand, the problem of the fiber fuse phenomenon needs to be resolved to prevent the destruction of fibers. Here, we experimentally demonstrate a fuse propagation velocity of 21.9 mm/s, which is 1–2 orders of magnitude slower than that in standard silica fibers. The achieved threshold power density and proportionality constant between the propagation velocity and the power density are 1/180 of and 170 times the values for silica fibers, respectively. An oscillatory continuous curve instead of periodic voids is formed after the passage of the fuse. An easy fuse termination method is also presented. These results provide a useful guideline for the performance limitation of POF-based Brillouin sensors from the aspect of highest incident power.

4. 5. 1 Introduction

Just over a quarter century ago, Kashyap and Blow [183,184] published their influential paper on the observation of the optical fiber fuse phenomenon: the continuous self-destruction of a fiber by propagating light. High-power light propagating through the fiber results in local heating and the creation of an optical discharge that is then captured in the fiber core and travels back along the fiber toward the light source, consuming the light energy and leaving a train of voids [185]. While fiber fuse propagation is stunningly beautiful [186], the fiber cannot be used after the passage of the fuse. This effect, along with the Shannon limit [187-189], nonlinear effects [190,191], and the optical amplifier bandwidth [191], is now regarded as a critical factor limiting the maximal optical power that can be delivered [192,193]. The fuse properties must be well characterized so that all possible measures are taken to avoid the creation of a fiber fuse.

The fuse properties in various glass fibers including standard silica-based single-mode fibers (SMFs) [183-186, 194-196], microstructured fibers [197], fluoride fibers [198], chalcogenide fibers [198], erbium-doped fibers [199], photonic crystal fibers [200], and hole-assisted fibers [200] are well documented. The fiber fuse is reported to be typically induced at an input optical power of one to several watts (one to several megawatts per square centimeter) and to have a propagation velocity of one to several meters per second. These properties differ according to the type of glass fiber; the threshold power, for instance, is reported to be much higher in photonic crystal and hole-assisted fibers than in silica SMFs [200], and nonlinear saturation of the fuse velocity has been observed in erbium-doped fibers [199]. To date, reports detailing similar properties of non-glass fibers such as polymer optical fibers (POFs) have not been published. Several special POFs with relatively low propagation losses and broadband transmission capabilities have recently become commercially available [201,202] and extensive studies have investigated the implementation of POF-based high-capacity communication systems [201,202] and possible engineering applications of nonlinear effects in POFs [140,141]. Therefore, there is a pressing need to clarify the fuse properties of POFs.

In this Letter, we characterize the POF fuse and discuss its unique properties. The propagation velocity of the bright spot is one to two orders of magnitude slower than that in standard silica SMFs. The threshold power density is 1/180 of the reported value for silica SMFs. We find that, after the passage of the fuse, an oscillatory continuous curve is formed in the POF. We also show that the POF fuse can be easily terminated by local elastic deformation of the waveguide structure.

4. 5. 2 Experimental setup

The perfluorinated graded-index POF [201] employed in this experiment consists of a core (50 μm diameter), cladding (100 μm diameter), and overcladding (750 μm diameter) encased in polyvinyl chloride. The core and cladding layers are composed of doped and undoped polyperfluorobutenylvinyl ether, respectively. The refractive index at the center of the core is 1.356, whereas that of the cladding layer is 1.342 [203]; these values do not depend strongly on the optical wavelength [123]. The polycarbonate reinforcement overcladding reduces microbending losses and increases the load-bearing capability. The propagation loss is relatively low (approximately 250 dB/km) even at 1.55 μm, and inexpensive optical amplifiers (EDFAs) can be used to boost the optical power (the standard polymethyl methacrylate POF is optimized for visible light transmission, and its propagation loss at 1.55 μm is higher than 1 × 10^5 dB/km).

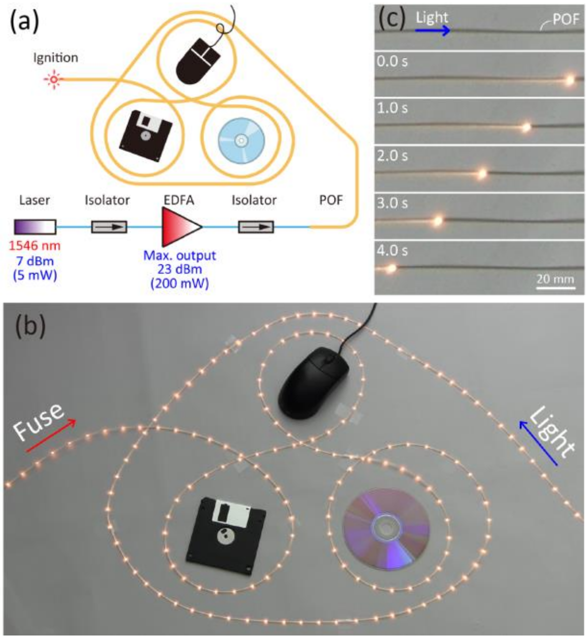

Fig. 4.5.1 (a) Schematic of the experimental setup. The silica SMFs are indicated by blue lines. (b) Composite photograph of the fiber fuse propagating along the POF; photographs were taken at 1-second intervals. The light was injected from the right-hand side, while the fuse propagated from the left-hand side. The fiber arrangement was that of Todoroki [186] to allow a direct comparison between the POF and silica SMF. (c) Magnified view of the propagating fuse. The light was injected from the left-hand side.

Fig. 1(a) depicts the experimental setup, in which 7-dBm (5-mW) output light from a

1546-nm distributed-feedback laser diode (NX8562LB; NEC; approximately 1-MHz linewidth) was amplified by an EDFA (LXM-S-21; Luxpert Technologies) to up to 23 dBm (200 mW) and injected into a 15-m-long POF. Two optical isolators were inserted to protect the laser and EDFA from reflected or backscattered light. The end of the silica SMF fitted with an 'FC' connector was connected to one end of the POF fitted with an 'SC' connector via an FC/SC adaptor (coupling loss approximately 0.3 dB) [140,141]. We confirmed that the fiber fuse can be initiated in the same way as in glass fibers [183-186, 194-200] by external stimuli such as heating, bending, or bringing the fiber output end into contact with an absorbent material. For the demonstration discussed here, we used a POF end surface polished roughly with 0.5-μm alumina powder.

4. 5. 3 Experimental results

From observations of the propagation of the fuse along the POF (Fig. 4.5.1(b)), the propagation velocity was calculated to be approximately 24 mm/s, which is extremely slow in comparison to Todoroki's [186] result for a silica SMF. The optical power of the propagating light was calculated using the measured power of the injected light, the coupling loss at the SMF/POF interface, and the propagation loss in the POF to be approximately 75 mW, corresponding to a maximal power density of 7.6 kW/cm^2 (Refer to the next paragraph for calculation method). A magnified view of the fuse propagation along a straight portion of the POF is shown in Fig. 4.5.1(c) (70.5 mW, 22.8 mm/s).

Here, we derive an equation for the maximal power density I in the core when light with a certain power P is injected into the graded-index POF. We consider a refractive index in the core that takes a parabolic profile [201]. Under the assumption that all modes propagate with equal attenuation without coupling, the optical power profile is given, in the same way as the refractive index profile, by [204]

$$p(r) = p(0)\left(1-\left(\frac{r}{R}\right)^{g}\right), \qquad (1)$$

where r is the radial distance from the core center, R is the core radius, and g is the refractive index profile coefficient. Consequently, the maximal power density I can be calculated as

$$I = \lim_{r \to 0} \frac{P}{\pi r^2} \frac{\int_0^{2\pi} d\theta \int_0^{r} \left(1 - \left(\frac{r}{R} \right)^g \right) r dr}{\int_0^{2\pi} d\theta \int_0^{R} \left(1 - \left(\frac{r}{R} \right)^g \right) r dr}$$

$$= \frac{P}{\pi R^2} \frac{g+2}{g} \quad . \tag{2}$$

By assuming g ≈ 2 in the graded-index POF [201], Eq. (2) can be further simplified as

$$I = \frac{2P}{\pi R^2} \quad , \tag{3}$$

which indicates that the maximal power density in the graded-index POF with an incident power P is equal to the average power density in a step-index POF of the same core diameter with twice the incident power. For instance, for P = 75 mW and R = 25 μm, I is calculated to be 7.6 kW/cm^2.

We found that the fuse propagation velocity in the POF, measured at 1.55 μm, had an almost linear dependence on the maximal power density with a slope of 1.59 × 10^6 mm·s^{-1}·MW^{-1}·cm^{-2} (Fig. 4.5.2(a)). The power density at which the fuse ceased, i.e. the threshold power density, was 6.6 kW/cm^2 at a propagation velocity of 21.9 mm/s. Comparing these results with those of silica SMFs (Fig. 4.5.2(b); results [194] at 1.48 μm and the theoretical line [195] at 1.55 μm) revealed that at 1.55 μm the slope in the POF data (corresponding to the efficiency of the velocity control) was 17 times as steep as that in the silica SMF (9.41 × 10^4 mm·s^{-1}·MW^{-1}·cm^{-2}), and the threshold power density of the POF was 180 times lower than that of the silica SMF (approximately 1.2 MW/cm^2). The minimal propagation velocity achieved at 1.55 μm was 11 times as low as that experimentally obtained in a silica SMF at 1.48 μm (250 mm/s) [196].

Digital micrographs taken after the passage of the fuse disclose the extent of the damage to the fiber. The fuse was initially triggered by exploiting the rough surface at the end of the POF (Fig. 4.5.3(a)) and was verified to be induced at the center of the core, which supports the assumption in our calculation that the maximal power density in the fiber cross section affects the fuse induction and can be used to determine the threshold power density. The passage of the fuse (Fig. 4.5.3(b)) appeared as a continuous black carbonized curve that oscillated periodically along the length of the POF, which is considerably different from the bullet-shaped voids observed in glass SMFs. The oscillation period was approximately 1300 μm, which is in general agreement with the theoretical oscillation period of the ray [9]. Fig. 4.5.3(c) shows the position where the fuse ceased after the incident optical power was reduced to that below the threshold; since the fuse remained at this point for several seconds, it melted a relatively large area of the POF, which resulted in the observed bending.

Optical propagation loss in the POF after the passage of the fuse was measured for incremental cutbacks from 30 cm to 20 cm (Fig. 4.5.3(d)) and a fixed input power of 10 dBm (10 mW) at 1.55 μm. A loss of 1.4 dB/cm indicates that, unlike silica SMFs [183-186, 194-196], light can propagate through the POF for several tens of centimeters after the passage of the fuse. We believe this is because undamaged regions remain in the core and cladding layers as these diameters are relatively large, which is a unique characteristic of POFs. Yet this propagation loss is somewhat significant for communication applications, and so once the fuse is induced, it is crucial to stop the propagation as soon as possible.

Several methods for terminating fiber fuses have been developed for glass fibers [200, 205-207], which are in principle also applicable to POFs. One method is to thin the outer diameter of the fiber at a certain position while maintaining the core diameter [206]; this can reduce the internal pressure and arrest the propagating fuse via deformation. In silica SMFs, this structure is fabricated using hydrofluoric acid as an etchant [206], but in a POF, chloroform could be used to etch the overcladding layer [177]. An even easier method, which we present here, is to pressure-bond a small metal ring around the fiber; this method is only applicable to POFs with an extremely high flexibility [155]. The optical power of the particular propagating mode that provides the bright spot with energy is decreased below the threshold by deformation, and the propagating fuse is thus terminated. The resulting induced optical loss is negligibly low, and an image of the fuse termination at the position of the ring (Fig. 4.5.3(e)) shows that bending did not occur. Once the ring is detached, the polymer material will return to the original configuration (elastic deformation).

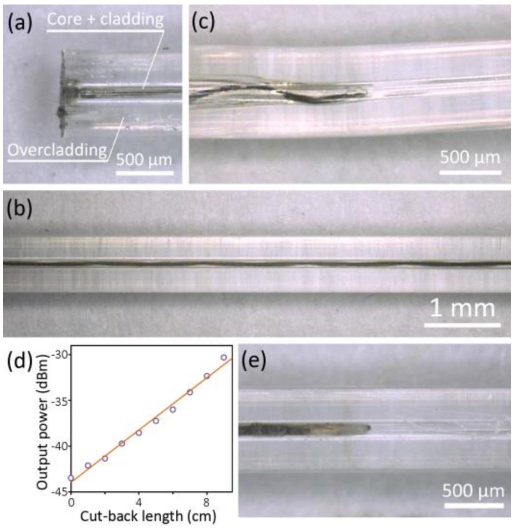

Fig. 4.5.3 (a) Digital micrograph of the POF end at which the fuse was initiated by exploiting the rough surface. (b) The path of the fuse in the POF. (c) The point at which the fuse was terminated by decreasing the input optical power. (d) The dependence of the output power on the cut-back length. The open circles are measured points, and the solid line is a linear fit. The slope of the line is 1.4 dB/cm. (e) Image of the fuse termination in the POF at the position of a nickel ring.

4. 5. 4 Conclusion

we have experimentally demonstrated a POF fuse propagation velocity of 21.9 mm/s, which is 1–2 orders of magnitude slower than that in standard silica fibers. The achieved threshold power density and proportionality constant between the propagation velocity and the power density are 1/180 of and 170 times the values for silica fibers, respectively. We have found that a unique oscillatory continuous carbonized curve is formed after the passage of the fuse, which can be terminated easily. Future work will focus on understanding the detailed mechanism of the initiation and propagation of the POF fuse. We believe that these results serve not only as a valuable guideline for the development of POF-based high-capacity transmission systems and engineering applications of nonlinear effects in POFs but also as a strong impetus for the on-going research relating to fiber fuses and material sciences.

5 Conclusions

In this dissertation, we studied on distributed strain and temperature sensing based on Brillouin scattering in polymer/plastic optical fibers (POFs). To begin with, we clarified the unique Brillouin properties in POFs. We then provided the first demonstration of distributed sensing. Besides, we conducted some research related to its performance improvement.

In Chapter 1: “Introduction,” the concept of fiber-optic nerve systems for smart materials and structures, the principle of Brillouin scattering, and the conventional distributed sensing techniques based on Brillouin scattering were reviewed as the background of this work. Then, the history, physical properties, and Brillouin properties of POFs were explained.

In Chapter 2: “Brillouin properties in large-strain applied POFs,” in Section 1: “Brillouin gain spectrum (BGS) dependence on large strain,” first, by applying large strain of up to 20%, the strain dependence of BGS in the PFGI-POF was measured in detail. The BFS exhibited a non-monotonic nature, with which temperature sensing even with zero strain sensitivity will be feasible. The Stokes power drastically dropped when the applied strain was larger than approximately 10%. This behavior is probably caused by the large-strain dependence of the propagation loss. The identification of the applied strain is sometimes difficult only by BFS due to its non-monotonic nature; in that case, using the Stokes power dependence will be one of the solutions. Since this nature may vary depending on the time of applying strain or the types of the POFs (PMMA-POFs, partially-chlorinated POF, etc.), further investigation is required on this point. We believe that these results are of great significance in developing large-strain sensors based on Brillouin scattering in POFs.

In Chapter 2, Section 2: “Brillouin frequency shift hopping,” The BGS dependence on large strain of up to 60 % in a PFGI-POF was investigated at 1.55 μm, and an abrupt change in BFS from approximately 2.7 GHz to approximately 3.2 GHz was observed. We showed that this “BFS hopping” is probably caused by the varied acoustic velocity induced by the stepwise change in the core diameter (because of the yield of polycarbonate-based overcladding layer). We also discussed the use of the Stokes power ratio to determine the large strain applied to the POF. Subsequently, strain- and temperature-dependence coefficients of the BFS in the slimmed-down POF were −65.6 MHz/% and −4.04 MHz/K respectively, which indicates the possibility of further higher-precision temperature sensing with lower strain sensitivity. We believe that the physical aspects of these results are interesting and will be of great significance in developing POF-based large-strain sensing systems in the near future.

In Chapter 3: “Distributed strain and temperature sensing using POFs,” in Section 1: “First demonstration based on BOCDR,” distributed strain and temperature sensing with a centimeter-order spatial resolution in a POF was demonstrated for the first time using a cost-effective BOCDR technique. A 10-cm-long heated section of a 1.3-m-long POF was successfully detected with a theoretical spatial resolution of 7.4 cm and a sampling rate of 3.3 Hz (per measured point). The limitation of the sensing performances was discussed. We believe that our results have overcome a stereotype of perceiving POF-based Brillouin distributed sensing with a high resolution and/or a high SNR as almost infeasible.

In Chapter 3, Section 2: “Simplification of experimental setup,” first, we developed simplified (S-) BOCDR, where the light Fresnel-reflected at a partial reflection point (or the fiber end) was used as reference light and an additional reference path used in standard implementations can be removed. This configuration was useful for practical application and enhancement of SNR in BOCDR. Then, we implemented S-BOCDR using a POF as a fiber under test, which provides the following advantages over S-BOCDR using a standard silica single-mode fiber (SMF): (1) the Fresnel-reflected light can be stably returned at the interface between the POF and an SMF (the pigtail of an optical circulator), and (2) the effect of the 0th correlation peak can be easily and effectively suppressed by exploiting a so-called BFS-hopping phenomenon. We then experimentally demonstrated a distributed measurement and detected a 0.46-m-long heated POF section.

In Chapter 4: "Relevant work for improvement of POF-based Brillouin sensors," in Section 1: "Characterization of stimulated Brillouin scattering in POFs," Stimulated Brillouin scattering (SBS) in POFs was observed, for the first time to the best of our knowledge, using the pump-probe technique without lock-in detection, and the dependences of the BGS on POF length, pump/probe powers, and temperature were fully investigated. We clarified that the optimal POF length for SBS observation is 3.8 m when the probe and pump powers are 21.1 dBm and 22.2 dBm, respectively. This length can be, we predict, elongated by the pump and probe waves with much higher powers. We also showed that the Stokes power was raised nonlinearly with increasing probe and pump powers, and that >20-dBm power is required for both pump and probe waves to efficiently induce SBS in POFs. In addition, the BFS dependence on temperature was measured to be −4.02 MHz/K, which was in good agreement with previous experiments. We believe that these results will offer a crucial basis for implementing distributed Brillouin sensors (especially, Brillouin optical time-domain analysis (BOTDA) systems) based on POFs with extremely high flexibility.

In Chapter 4, Section 2: "Estimation of Brillouin properties in PMMA-POFs," first, the acoustic velocities in POFs were measured based on the ultrasonic pulse-echo technique for the estimation of their BFS. First, the BFS of a PFGI-POF at 1.55 μm was estimated to be approximately 2.9 GHz. This value moderately agreed with the actual value previously reported, indicating that this method can be used to roughly estimate the BFS. Then, the acoustic velocity in a PMMA-POF with 980 μm core diameter was measured to be 2.8×10^3 m/s, from which its BFS was estimated to be approximately 13 GHz at 650 nm and approximately 5.4 GHz at 1.55 μm. Next, the BFS dependences on temperature and strain in PMMA-POFs were estimated using ultrasonic pulse-echo technique. We found that the BFS varies linearly depending on temperature with a coefficient of approximately –17 MHz/K at 650 nm pump. Since this value is –7.1 times larger than that of silica fibers at 650 nm, and is even 1.7 times larger than that of PFGI-POFs at 650 nm, PMMA-POFs appear to be a good candidate for Brillouin-based temperature sensing with high precision. We also found that, in contrast, the BFS varied nonlinearly depending on applied strain, which seems to be related to the elastic-to-plastic transition of PMMA. More accurate estimation will be feasible by taking the refractive-index dependence on strain into consideration. We believe that this information will be useful in developing temperature/strain sensors based on Brillouin scattering in POFs with high flexibility, low cost, easy connection, high safety, and memory effect.

In Chapter 4, Section 3: “Fast flaw detection in POFs using infrared thermometry,” we demonstrated a fast and low-cost detection of the flaws in POFs using an IRT, which can overcome the drawbacks of the conventional techniques. The locations of the flaws were successfully detected, even when the POF was protected by thick jackets. The optical loss dependence of the temperature at the flaw was linear with a coefficient of approximately 0.74 °C/dB when the optical power was 24.5 dBm (282 mW) at 1.55 μm. The optical power dependence of the measured temperature at the flaw with a fixed loss was also linear, which predicts that a higher optical power is desirable for the loss estimation with more precision. We hope that this method will be of common use, with its fast measurement capability, ease of handling, and cost efficiency, in examining the quality of POFs at the final stage of their fabrication process in the near future.

In Chapter 4, Section 4: “Observation of BGS in tapered POF,” By the heat-and-pull technique, we fabricated the PFGI-POF taper with an outer diameter of the waist of 223 μm, and successfully observed its BGS for the first time. The Stokes power was slightly enhanced by tapering probably because of higher optical power density in the core. The BFS was downshifted by approximately 40 MHz, which was experimentally shown to originate partially from the heat applied to the POF. By using the enhanced Brillouin signal in a much longer tapered POF, the signal-to-noise ratio of the POF-based distributed sensing systems could be improved. In addition, the BFS shift induced by high heating temperature might be actively utilized as a principle of the "temperature memory effect". We believe that, along with the previously-reported "strain memory effect", this novel function could be of great use in implementing POF-based Brillouin devices and systems including distributed strain and temperature sensors.

In Chapter 4, Section 5: "Observation of POF fuse," we reported on the observation of POF fuse phenomenon. Although optical fibers with a high transmission capacity were in demand, the problem of the fiber fuse phenomenon needs to be resolved to prevent the destruction of fibers. Here, we experimentally demonstrated a fuse propagation velocity of 21.9 mm/s, which was 1–2 orders of magnitude slower than that in standard silica fibers. The achieved threshold power density and proportionality constant between the propagation velocity and the power density were 1/180 of and 170 times the values for silica fibers, respectively. An oscillatory continuous curve instead of periodic voids was formed after the passage of the fuse. An easy fuse termination method was also presented. These results provided a useful guideline for the performance limitation of POF-based Brillouin sensors from the aspect of highest incident power.

Thus, in this dissertation, we investigated for the first time the following two Brillouin properties of POFs: (a) BGS dependence on large strain in POFs, and (b) BFS hopping. Next, we succeeded in demonstrating distributed stain and temperature sensing using POFs based on BOCDR and S-BOCDR. We also performed the following six experiments to improve the performance of the POF-based distributed sensors: (i) clarification of the SBS properties in POFs for SNR enhancement, (ii) estimation of the Brillouin properties in PMMA-POFs toward higher-sensitivity temperature sensing, (iii) fast flaw detection in

POFs using infrared thermometry for efficient selection of high-quality POFs to be used as sensor heads, (iv) observation of BGS in tapered POFs toward implementation of a memory function regarding temperature, and (v) observation of a fiber fuse phenomenon in POFs toward understanding of the performance limitation of POF-based Brillouin sensors. We believe that these results are a key technological step toward the development of next-generation distributed temperature/strain sensing systems based on Brillouin scattering in POFs with high flexibility and memory function.

Acknowledgements

First, I would like to express my deepest gratitude to my supervisor, Prof. Kentaro Nakamura, for his specific education of ultrasonic and optical technology. I also express my sincere appreciation to Asst. Prof. Yosuke Mizuno for his continuous guidance, encouragement, and help throughout the course of this work. Especially I appreciate his instruction related to logical thinking, paper writing skills, presentation techniques, and knowledge on nonlinear optics. My appreciation also goes to Assoc. Prof. Marie Tabaru.

I am profoundly grateful to Assoc. Prof. D. Koyama, Doshisha University, for his insightful comments and suggestions on the measurement technique of acoustic velocity. I am also thankful to Prof. K. Hotate and M. Kishi, the University of Tokyo, for their experimental assistance related to Brillouin optical correlation-domain analysis using polymer/plastic optical fibers (POFs). I express my thanks also to Prof. H. Hosoda for their instruction concerning the use of the tension tester (used in Chapters 3 and 4) and to the staff of the Technical Department, Tokyo Institute of Technology, Japan, for providing several fixtures—Al plates (used in Chapters 4).

As for the experiments on POF fuse observation, I would like to express my deep appreciation to Dr. S. Todoroki (National Institute for Materials Science) for his theoretical advice, Dr. H. Yoshida (Sekisui Chemical Co. Ltd.) for his helpful discussions, R. Nedelcov (Tokyo University of the Arts) for his English editing, and Prof. A. Okino, T. Iwai, K. Kakegawa, Y. Watanabe, Y. Ishihara, Y. Utsunomiya, Dr. T. Inamura, Dr. M. Tahara, T. Aoki, H. Shim, and M. Ii (Tokyo Institute of Technology) for their experimental assistance.

Of course, I am grateful to S. Kondo, Dr. Y. Wada, Dr. K. S. Kim, Dr. X. Guo, W. Qiu, K. Minakawa, M. Ding, H. Tanaka, S. Ohara, Y. Kato, T. Ishii, R. Nakamura, J. Chen, G. Numata, S. Ito, H. Ujihara, and all the other members. Furthermore, I am greatly indebted to the secretaries of the laboratory, M. Ito and M. Azuma, for their kind help and personal advice in various aspects.

Finally, I would like to express my indebtedness to my brothers and mother for their understanding and support during the entire period of my study.

References

[1] K. C. Kao and G. A. Hockham, “Dielectric-fibre surface waveguides for optical frequencies,” IEE Proc. **113**, 1151 (1966).

[2] H. Lamm, “Biegsame optische gerate,” Z. Instrumenten. **50**, 579 (1930).

[3] A. C. S. van Heel, “A new method of transporting optical images without aberrations,” Nature **173**, 39 (1954).

[4] H. H. Hopkins and N. S. Kapany, “Transparent fibres for the transmission of optical images,” Opt. Acta **1**, 164 (1955).

[5] F. P. Kapron, D. B. Keck, and R. D. Maurer, “Radiation losses in glass optical fibers,” Appl. Phys. Lett. **17**, 423 (1970).

[6] W. G. French, J. B. MacChesney, P. B. O’Connor, and G. W. Tasker, “Optical waveguides with very low loss,” Bell Syst. Tech. J. **53**, 951 (1974).

[7] T. Miya, Y. Terunuma, T, Hosaka, and T, Miyashita, “Ultimate low-loss single-mode fiber at 1.55 pm,” Electron. Lett. **15**, 106 (1979).

[8] R. Ramaswani and K. Sivarajan, Optical Networks: A Practical Perspective, 2nd ed. (Morgan Kaufmann Publishers, San Francisco, 2002).

[9] G. P. Agrawal, Fiber-Optic Communication Systems, 3rd ed. (Wiley, New York, 2002).

[10] I. P. Kaminow and T. Li, Eds., Optical Fiber Telecommunications, Vols. 4A and 4B (Academic Press, Boston, 2002).

[11] G. P. Agrawal, Lightwave Technology: Telecommunication System (Wiley, Hoboken, NJ, 2005).

[12] D. Davies and S. A. Kingsley, “The use of optical fibers as instrumentation transducers,” Proc. CLEO’76, 24, 1976.

[13] V. Vali and R. W. Shorthill, “Fiber ring interferometer,” Appl. Opt. **15**, 1099 (1976).

[14] E. Udd, Fiber Sensors (Wiley, New York, 1991).

[15] C. Menadier, C. Kissinger, and H. Adkins, “The fotonic sensor,” Instrum. & Control Syst. **40**, 114 (1967).

[16] B. Culshaw, Optical Fiber Sensing and Signal Processing (Peter Pereginus, London, 1984).

[17] T. G. Giallorezi, J. A. Bucaro, A. Dandridge, G. H. Sigel, J. H. Cole, S. C. Rashleigh, and R. C. Priest, “Optical fiber sensor technology,” IEEE J. Quantum Electron. **18**, 624 (1982).

[18] K. Hotate, “Application of synthesized coherence function to distributed optical sensing,” Meas. Sci. Technol. **13**, 1746 (2002).

[19] T. Horiguchi, A. Rogers, W. C. Michie, G. Stewart, and B. Culshaw, in Optical Fiber Sensors, ed. J. Dakin and B. Culshaw (Artech House, Boston, 1997), Vol. IV, Chap. 14, 309.

[20] A. D. Kersey, in Optical Fiber Sensors, ed. J. Dakin and B. Culshaw (Artech House, Boston, 1997), Vol. IV, Chap. 15, 369.

[21] L. Thevenaz, in Trends in Optical Non-Destructive Testing and Inspection, ed. P. Rastogi and D. Inaudi (Elsevier, Amsterdam, 2000), Chap. 29, 447.

[22] K. Hotate, “Fiber sensor technology today,” Jpn. J. Appl. Phys. **45**, 6616 (2006).

[23] D. Inaudi, A. Ruefenacht, B. von Arx, H. P. Noher, S. Vurpillot, and B. Glisic, “Monitoring of a concrete arch bridge during construction,” Proc. SPIE **4696**, 146 (2002).

[24] S. Katz, “Factors affecting strain gauge selection for smart structure application,” Proc. SPIE **3330**, 20 (1998).

[25] E. Udd, “The emergence of fiber optic sensor technology,” in Fiber Optic Sensors – An Introduction for Engineers and Scientists (John Wiley & Sons, USA, 1991).

[26] W. Morey, G. Meltz, and W. Glenn, “Fiber optic Bragg grating sensors,” Proc. SPIE **1169**, 98 (1989).

[27] C. Lee and H. Taylor, “Interferometric optical fibre sensors using internal mirrors,” Electron. Lett. **24**, 193 (1988).

[28] E. Udd, “The emergence of fiber optic sensor technology,” in Fiber Optic Sensors – An Introduction for Engineers and Scientists (John Wiley & Sons, USA, 1991).

[29] H. Lefevre, The Fiber-Optic Gyroscope (Artech House, Boston, 1993).

[30] K. Hotate, in Optical Fiber Sensors, ed. J. Dakin and B. Culshaw (Artech House, Boston, 1997), Vol. IV, Chap. 11, 167.

[31] T. Mori, M. Nakajima, K. Iwano, M. Tanaka, S. Kikuyama, and Y. Machijima,

"Application of the fiber optical oscillation sensor to AE measurement at the rock compression test," 11th Congress of the International Society for Rock Mechanics pp. 1101-1104 (2007).

[32] W. Wang, N. Wu, Y. Tian, C. Niezrecki, and X. Wang, "Miniature all-silica optical fiber pressure sensor with an ultrathin uniform diaphragm," Opt. Express **18**, 9006 (2010).

[33] L. Xu, J.C. Fanguy, K. Soni, and S. Tao, "Optical fiber humidity sensor based on evanescent-wave scattering," Opt. let. **29**, 1191 (2004).

[34] G. P. Agrawal, Nonlinear Fiber Optics, 2nd ed. (Academic Press, New York, 1995).

[35] T. Horiguchi, T. Kurashima, and M. Tateda, "Tensile strain dependence of Brillouin frequency shift in silica optical fibers," IEEE Photon. Technol. Lett. **1**, 107 (1989).

[36] T. Kurashima, T. Horiguchi, and M. Tateda, "Thermal effects of Brillouin gain spectra in single-mode fibers," IEEE Photon. Technol. Lett. **2**, 718 (1990).

[37] M. Nikles. L. Thevenaz, and P. A. Robert, "Brillouin gain spectrum characterization in single-mode optical fibers," OSA/IEEE J. Lightwave Technol. **15**, 1842 (1997).

[38] D. Cotter, "Stimulated Brillouin scattering in optical fibers," J. Opt. Commun. **4**, 10 (1982).

[39] N. Shibata, K. Okamoto, and Y. Azuma, "Longitudinal acoustic modes and Brillouin-gain spectra for GeO_2-doped-core single-mode fibers," J. Opt. Soc. Amer. B **6**, 1167 (1989).

[40] R. G. Smith, "Optical power handling capacity of low loss optical fibers as determined by stimulated Raman and Brillouin scattering," Appl. Opt. **11**, 11, 2489 (1972).

[41] D. Cotter, "Observation of stimulated Brillouin scattering in low-loss silica fibre at 1.3 μm," Electron. Lett. **18**, 12, 495 (1982).

[42] A. Zadok, E. Zilka, A. Eyal, L. Thevenaz, and M. Tur, "Vector analysis of stimulated Brillouin scattering amplification in standard single-mode fibers," Opt. Express **16**, 26, 21692 (2008).

[43] T. Horiguchi and M. Tateda, "BOTDA – nondestructive measurement of single-mode optical fiber attenuation characteristics using Brillouin interaction: theory", OSA/IEEE J. Lightwave Technol. **7**, 1170 (1989).

[44] T. Horiguchi, T. Kurashima, and M. Tateda, "A technique to measure distributed strain in optical fiber", IEEE Photon. Technol. Lett. **2**, 352 (1990).

[45] T. Kurashima, T. Horiguchi, and M. Tateda, "Distributed-temperature sensing using

stimulated Brillouin scattering in optical silica fibers," Opt. Lett. **15**, 1038 (1990).

[46] T. Horiguchi, T. Kurashima, and Y. Koyamada, "1 m spatial resolution measurement of distributed Brillouin frequency shift by single-mode fibers," Tech. Dig. Opt. Fiber Meas. **2**, 73 (1994).

[47] T. Horiguchi, K. Shimizu, T. Kurashima, M. Tateda, and Y. Koyamada, "Development of a distributed sensing technique using Brillouin scattering", OSA/IEEE J. Lightwave Technol. **13**, 1296 (1995).

[48] A. Fellay, L. Thevenez, M. Facchini, M. Nikles, and P. Robert, "Distributed sensing using stimulated Brillouin scattering: towards ultimate resolution," Tech. Dig. Opt. Fiber Sens. **16**, 324 (1997).

[49] H. Naruse and M. Tateda, "Trade-off between the spatial and the frequency resolutions in measuring the power spectrum of the Brillouin backscattered light in an optical fiber," Appl. Opt. **38**, 6516 (1999).

[50] X. Bao, D. J. Webb, and D. A. Jackson, "32-km distributed temperature sensor using Brillouin loss in optical fiber," Opt. Lett. **18**, 1561 (1993).

[51] A. Vedadi, D. Alasia, E. Lantz, H. Maillotte, L. Thevenaz, M. Gonzalez-Herraez, and T. Sylvestre, "Brillouin optical time-domain analysis of fiber-optic parametric amplifiers," IEEE Photon. Technol. Lett. **19**, 179 (2007).

[52] W. Li, X. Bao, Y. Li, and L. Chen, "Differential pulse-width pair BOTDA for high spatial resolution sensing," Opt. Express **16**, 21616 (2008).

[53] M. Nikles, L. Thevenaz, and P. A. Robert, "Simple distributed fiber sensor based on Brillouin gain spectrum analysis," Opt. Lett. **21**, 758 (1996).

[54] X. Bao, J. Dhliwayo, N. Heron, D. J. Webb, and D. A. Jackson, "Experimental and theoretical studies on a distributed temperature sensor based on Brillouin scattering," OSA/IEEE J. Lightwave Technol. **13**, 1340 (1995).

[55] A. W. Brown, M. DeMerchant, X. Bao, and T. W. Bremmer, "Spatial resolution enhancement of a Brillouin-distributed sensor using a novel signal processing method," OSA/IEEE J. Lightwave Technol. **17**, 1179 (1999).

[56] K. Kishida, C. H. Li, S. Lin, and K. Nishiguchi, "Pulsed pre-pump method to achieve cm-order spatial resolution in Brillouin distributed measuring technique," IEIC Tech. Rep. **104**, 15 (2004).

[57] K. Kishida, C. H. Li, and K. Nishiguchi, "Pulse pre-pump method for cm-order spatial resolution of BOTDA," Proc. SPIE **5855**, 559 (2005).

[58] A. W. Brown, B. G. Colpitts, and K. Brown, "Distributed sensor based on dark-

pulse Brillouin scattering," IEEE Photon. Technol. Lett. **17**, 1501 (2005).

[59] A. W. Brown, B. G. Colpitts, and K. Brown, "Dark-pulse Brillouin optical time-domain sensor with 20-mm spatial resolution," OSA/IEEE J. Lightwave Technol. **25**, 381 (2007).

[60] K. Y. Song, S. Chin, N. Primerov, and L. Thevenaz, "Time-domain distributed fiber sensor with 1 cm spatial resolution based on Brillouin dynamic grating," J. Lightwave Technol. **28**, 2062 (2010).

[61] M. A. Soto, X. Angulo-Vinuesa, S. Martin-Lopez, S.-H. Chin, J. D. Ania-Castañon, P. Corredera, E. Rochat, M. Gonzalez-Herraez, and L. Thevenaz, "Extending the real remoteness of long-range Brillouin optical time-domain fiber analyzers," J. Lightwave Technol. **32**, 152 (2014).

[62] Y. Dong, L. Chen, and X. Bao, "Extending the sensing range of Brillouin optical time-domain analysis combining frequency-division multiplexing and in-line EDFAs," J. Lightwave. Technol. **30**, 1161 (2012).

[63] T. Kurashima, T. Horiguchi, H. Izumita, S. Furukawa, and Y. Koyamada, "Brillouin optical-fiber time domain reflectometry," IEICE Trans. Commun. **E76-B**, 382 (1993).

[64] K. Shimizu, T. Horiguchi, Y. Koyamada, and T. Kurashima, "Coherent self-heterodyne Brillouin OTDR for measurement of Brillouin frequency shift distribution in optical fibers," OSA/IEEE J. Lightwave Technol. **12**, 730 (1994).

[65] H. Izumita, T. Sato, M. Tateda, and Y. Koyamada, "Brillouin OTDR employing optical frequency shifter using side-band generation technique with high-speed LN phase-modulator," IEEE Photon. Technol. Lett. **12**, 1674 (1996).

[66] Y. Koyamada, "Proposal and simulation of double-pulse Brillouin optical time-domain reflectometry," IEIC Tech. Rep. **106**, 35 (2007).

[67] Y. Koyamada, Y. Sakairi, N. Takeuchi, and S. Adachi, "Novel technique to improve spatial resolution in Brillouin optical time-domain reflectometry," IEEE Photon. Technol. Lett. **23**, 1910 (2007).

[68] Y. Sakairi, S. Matsuura, S. Adachi, and Y. Koyamada, "Prototype double-pulse BOTDR for measuring distributed strain with 20-cm spatial resolution," SICE Annual Conf. 2008, 1106 (2008).

[69] F. Wang, W. Zhan, X. Zhang, and Y. Lu, "Improvement of spatial resolution for BOTDR by iterative subdivision method," J. Lightw. Technol., **31**, 3663 (2013).

[70] M. N. Alahbabi, Y. T. Cho, and T. P. Newson, "150-km-range distributed

temperature sensor based on coherent detection of spontaneous Brillouin backscatter and in-line Raman amplification," J. Opt. Soc. Amer. B **22**, 1321 (2005).

[71] M. A. Soto, P. K. Sahu, G. Bolognini, and F. D. Pasquale, "Brillouin-based distributed temperature sensor employing pulse coding," IEEE Sens. J. **8**, 225 (2008).

[72] M. A. Soto, G. Bolognini, and F. D. Pasquale, "Analysis of optical pulse coding in spontaneous Brillouin-based distributed temperature sensors," Opt. Express **16**, 19097 (2008).

[73] D. Garus, K. Krebber, F. Schliep, and T. Gogolla, "Distributed sensing technique based on Brillouin optical-fiber frequency-domain analysis," Opt. Lett. **21**, 1402 (1996).

[74] D. Garus, K. Krebber, F. Schliep, and T. Gogolla, "Brillouin optical-fiber frequency-domain analysis for distributed temperature and strain measurements," OSA/IEEE J. Lightwave Technol. **15**, 654 (1997).

[75] R. Bernini, L. Crocco, A. Minardo, F. Soldovieri, and L. Zeni, "Frequency-domain approach to distributed fiber-optic Brillouin sensing," Meas. Sci. Technol. **27**, 288 (2002).

[76] R. Bernini, A. Minardo, and L. Zeni, "Stimulated Brillouin scattering frequency-domain analysis in a single-mode optical fiber for distributed sensing," Opt. Lett. **29**, 1977 (2004).

[77] R. Bernini, A. Minardo, and L. Zeni, "Distributed sensing at centimeter-scale spatial resolution by BOFDA: measurements and signal processing," IEEE Photon. J., **4**, 48 (2012).

[78] T. Hasegawa, Dissertation for master degree, The University of Tokyo, 1999.

[79] K. Hotate and T. Hasegawa, "Measurement of Brillouin gain spectrum distribution along an optical fiber using a correlation-based technique – proposal, experiment and simulation," IEICE Trans. Electron. **E83-C**, 405 (2000).

[80] K. Hotate and M. Tanaka, "Distributed fiber Brillouin strain sensing with 1-cm spatial resolution by correlation-based continuous-wave technique," IEEE Photon. Technol. Lett. **14**, 197 (2002).

[81] K. Hotate and M. Tanaka, "Correlation-based continuous-wave technique for optical fiber distributed strain measurement using Brillouin scattering with cm-order spatial resolution – Applications to smart materials –," IEICE Trans. Electron. **E84-C**, 1823 (2001).

[82] K. Hotate and S. S. L. Ong, “Distributed dynamic strain measurement using a correlation-based Brillouin sensing system,” IEEE Photon. Technol. Lett. **15**, 272 (2003).

[83] K. Hotate, K. Abe, and K. Y. Song, “Suppression of signal fluctuation in Brillouin optical correlation domain analysis system using polarization diversity scheme,” IEEE Photon. Technol. Lett. **18**, 2653 (2006).

[84] K. Y. Song, Z. He, and K. Hotate, “Optimization of Brillouin optical correlation domain analysis system based on intensity modulation scheme,” Opt. Express **14**, 4256 (2006).

[85] K. Y. Song, Z. He, and K. Hotate, “Effects of intensity modulation of light source on Brillouin optical correlation domain analysis,” OSA/IEEE J. Lightwave Technol. **25**, 1238 (2007).

[86] K. Hotate, W. M. Goh, Y. Mizuno, and Z. He, “Brillouin optical correlation- domain analysis based on simultaneous utilization of sinusoidal and noise modulation,” Proc. IEICE General Conf. 2008, 469 (2008).

[87] K. Hotate, K. Chigusa, Y. Mizuno, M. Kishi, and Z. He, “Improvement on S/N ratio of low-coherence BOCDA,” Proc. IEICE General Conf. 2009, 242 (2009).

[88] M. Kannou, S. Adachi, and K. Hotate, “Temporal gating scheme for enlargement of measurement range of Brillouin optical correlation domain analysis for optical fiber distributed strain measurement,” Proc. OFS-16, 454, 2003.

[89] K. Hotate, H. Arai, and K. Y. Song, “Range-enlargement of simplified Brillouin optical correlation domain analysis based on a temporal gating scheme,” SICE J. Cont. Meas. Syst. Int. **1**, 271 (2008).

[90] K. Y. Song and K. Hotate, “Enlargement of measurement range in a Brillouin optical correlation domain analysis system using double lock-in amplifiers and a single-sideband modulator,” IEEE Photon. Technol. Lett. **18**, 499 (2006).

[91] K. Y. Song, Z. He, and K. Hotate, “Distributed strain measurement with millimeter-order spatial resolution based on Brillouin optical correlation domain analysis,” Opt. Lett. **31**, 2526 (2006).

[92] K. Hotate and T. Yamauchi, “Fiber-optic distributed strain sensing system by Brillouin optical correlation domain analysis with a simple and accurate time-division pump-probe generation scheme,” Jpn. J. Appl. Phys. **44**, L1030 (2005).

[93] K. Y. Song and K. Hotate, “Distributed fiber strain sensor with 1-kHz sampling rate based on Brillouin optical correlation domain analysis,” IEEE Photon. Technol. Lett. **19**, 1928 (2007).

[94] W. Zou, Dissertation for doctoral degree, The University of Tokyo, 2007.

[95] W. Zou, Z. He, and K. Hotate, “Complete discrimination of strain and temperature using Brillouin frequency shift and birefringence in a polarization-maintaining fiber,” Opt. Express **17**, 1248 (2009).

[96] K. Y. Song and K. Hotate, “Brillouin optical correlation domain analysis in linear configuration,” IEEE Photon. Technol. Lett. **20**, 2150 (2008).

[97] T. Yari, K. Nagai, M. Ishioka, K. Hotate, and Y. Koshioka, “Aircraft structural health monitoring using on-board BOCDA system,” Proc. SPIE **6933**, 69330S (2008).

[98] Y. Kumagai, S. Matsuura, S. Adachi, and K. Hotate, “Enhancement of BOCDA system for aircraft health monitoring,” SICE Annual Conf. 2008, 2184 (2008).

[99] M. Imai, S. Miura, and K. Hotate, “Health monitoring of a full scale tunnel model using BOCDA-based fiber-optic distributed sensor,” Int. Conf. on Struc. Health Mon. & Int. Infra. 2005, 385 (2005).

[100] S. S. Ong, H. Kumagai, H. Iwaki, and K. Hotate, “Crack detection in concrete using a Brillouin optical correlation domain analysis based fiber optic sensor,” IEIC Tech. Rep. **102**, 49 (2003).

[101] Z. He, Dissertation for doctoral degree, The University of Tokyo, 1999.

[102] K. Hotate and Z. He, “Synthesis of optical coherence function and its applications in distributed and multiplexed optical sensing,” OSA/IEEE J. Lightwave Technol. **24**, 2541 (2006).

[103] K. Hotate, M. Enyama, S. Yamashita, and Y. Nasu, “A multiplexing technique of fiber Bragg grating sensors with the same reflection wavelength by the synthesis of optical coherence function,” Meas. Sci. Technol. **15**, 148 (2004).

[104] M. Enyama, Z. He, and K. Hotate, “Expansion of spatial measurement range by use of vernier effect in multiplexed fibre Bragg grating strain sensor with synthesis of optical coherence function,” Meas. Sci. Technol. **16**, 977 (2005).

[105] K. Hotate and K. Kajiwara, “Proposal and experimental verification of Bragg wavelength distribution measurement within a long-length FBG by synthesis of optical coherence function,” Opt. Express **16**, 7881 (2008).

[106] Z. He and K. Hotate, “Synthesized optical coherence tomography for imaging of scattering objects by use of a stepwise frequency-modulated tunable laser diode,” Opt. Lett. **24**, 1502 (1999).

[107] K. Hotate, Z. He, and T. Kitazume, “Surface shape measurement for multi-layered

object by synthesis of optical coherence function," IEEE J. Sel. Topics Quantum Electron. **6**, 723 (2000).

[108] B. Zhu, T. Saida and K. Hotate, "Variable optical filter using dynamic grating in Er-doped fiber controlled by synthesis of optical coherence function: proposal and experimental verification," IEICE Trans. Electron. **E86-C**, 97 (2003).

[109] X. Fan, Z. He, Y. Mizuno, and K. Hotate, "Bandwidth-adjustable dynamic grating in erbium-doped fiber by synthesis of optical coherence function," Opt. Express **13**, 5756 (2005).

[110] X. Fan, Z. He, and K. Hotate, "Novel strain- and temperature-sensing mechanism based on dynamic grating in polarization-maintaining erbium-doped fiber," Opt. Express **14**, 556 (2005).

[111] T. Saida and K. Hotate, "Distributed fiber-optic stress sensor by synthesis of the optical coherence function," IEEE Photon. Technol. Lett. **9**, 484 (1997).

[112] Z. He and K. Hotate, "Distributed fiber-optic stress-location measurement by arbitrary shaping of optical coherence function," OSA/IEEE J. Lightwave Technol. **20**, 1715 (2002).

[113] M. Kashiwagi and K. Hotate, "Elongation of measurement range by successively shifting measurement window in a high spatial resolution reflectometry for optical subscriber networks by synthesis of optical coherence function," Meas. Sci. Technol. **15**, 1512 (2004).

[114] Z. He, T. Tomizawa, and K. Hotate, "High-speed high-reflectance-resolution reflectometry by synthesis of optical coherence function," IEICE Electron. Express **3**, 122 (2006).

[115] W. Zou, C. Jin, and J. Chen, "Distributed strain sensing based on combination of Brillouin gain and loss effects in Brillouin optical correlation domain analysis," Appl. Phys. Express **5**, 082503 (2012).

[116] Y. Mizuno, W. Zou, Z. He, and K. Hotate, "Proposal of Brillouin optical correlation-domain reflectometry (BOCDR)," Opt. Express **16**, 12148 (2008).

[117] Y. Mizuno, W. Zou, Z. He, and K. Hotate, "Operation of Brillouin optical correlation-domain reflectometry: theoretical analysis and experimental validation," J. Lightwave Technol., **28**, 3300 (2010).

[118] Y Mizuno, Z. He, and K. Hotate, "One-end-access high-speed distributed strain measurement with 13-mm spatial resolution based on Brillouin optical correlation-domain reflectometry," IEEE Photon. Technol. Lett. **21**, 474 (2009).

[119] Y. Mizuno, Z. He, and K. Hotate, “Distributed strain measurement using a tellurite glass fiber with Brillouin optical correlation-domain reflectometry,” Opt. Commun. **283**, 2438 (2010).

[120] Y. Mizuno, Z. He, and K. Hotate, “Measurement range enlargement in Brillouin optical correlation-domain reflectometry based on temporal gating scheme,” Opt. Express **17**, 9040 (2009).

[121] Y. Mizuno, Z. He, and K. Hotate, “Measurement range enlargement in Brillouin optical correlation-domain reflectometry based on double-modulation scheme,” Opt. Exp., vol. 18, pp. 5926–5933, 2010.

[122] R. Yoshida, Optical fiber of broadband error: The POF, 1st ed. (POF consortium, Tokyo, Japan, 2004).

[123] T. Ishigure, Y. Koike and J. W. Fleming, “Optimum index profile of the perfluorinated polymer based GI polymer optical fiber and its dispersion properties,” J. Lightw. Technol. **18**, 178 (2000).

[124] M.G. Kuzyk, Polymer Fiber Optics: Materials, Physics, and Applications, 1st ed. (CRC Press, Boca Raton, FL, USA, 2006).

[125] Y. Koike, T. Ishigure, and E. Nihei, “High-bandwidth graded-index polymer optical fiber,” J. Lightwave Technol. **13**, 1475 (1995).

[126] K. Nakamura, I. R. Husdi, and S. Ueha, “A distributed strain sensor with the memory effect based on the POF OTDR,” Proc. SPIE **5855**, 807 (2005).

[127] I. Mollers, D. Jager, R. Gaudino, A. Nocivelli, H. Kragl, O. Ziemann, N. Weber, T. Koonen, C. Lezzi, A. Bluschke, and S. Randel, “Plastic optical fiber technology for reliable home networking: overview and results of the EU project pof-all,” Commun. Magazine, IEEE **47**, 58 (2009).

[128] S. Liehr, P. Lenke, M. Wendt, K. Krebber, M. Seeger, E. Thiele, H. Metschies, B. Gebreselassie, and J.C. Munich, “Polymer Optical Fiber Sensors for Distributed Strain Measurement and Application in Structural Health Monitoring,” Sensors Journal, IEEE **9**, 1330 (2009).

[129] C. Lethien, C. Loyez, J.P. Vilcot, N. Rolland, and P.A. Rolland, “Exploit the bandwidth capacities of the perfluorinated graded index polymer optical fiber for multi-services distribution,” Polymers **3**, 1006 (2011).

[130] J. Arrue, J. Zubia, G. Fuster, and D. Kalymnios, “Light power behavior when bending plastic optical fibers,” Optoelectronics IEEE Proc. **145**, 313 (1998).

[131] K. Nakamura, T. Okada and S. Ueha, “Measuring the optical path length of a plastic

optical fibre using the sing-around method and its sensor applications” J. Opt. A: Pure Appl. Opt. **3**, L17 (2001).

[132] L. Rovati, P. Fabbri, L. Ferrari, and F. Pilati, “Construction and evaluation of a disposable pH sensor based on large core plastic optical fiber,” Rev. Sci. Instrum. **82**, 023106 (2011).

[133] J. Nagata, S. Honma, M. Morisawa, and S. Muto, “Deveolpment of Polymer Waveguide-Type Alcohol Sensor,” In Proceedings of the Conference on Advanced Materials and Devices for Sensing and Imaging III, Beijing, China, 5 February 2008.

[134] C. Beres, F. Nazaré, N. Chagas de Souza, M. Miguel, M. M. Werneck, “Tapered plastic optical fiber based biosensor—Tests and application,” Biosens. Bioelectron., **30**, 328 (2011).

[135] Z. Xiong, G. D. Peng, B. Wu, P. L. Chu, “Highly tunable Bragg gratings in single-mode polymer optical fibers,” IEEE Photon. Technol. Lett. **11**, 352 (1999).

[136] G. Numata, N. Hayashi, M. Tabaru, Y. Mizuno, and K. Nakamura, “Ultra-sensitive strain and temperature sensing based on modal interference in perfluorinated polymer optical fibers,” IEEE Photon. J. **6**, 6802306 (2014).

[137] S. Liehr, M. Wendt, and K. Krebber “Distributed strain measurement in perfluorinated polymer optical fibres using optical frequency domain reflectometry,” Meas. Sci. and Technol. **21**, 094023 (2010).

[138] P. Lenke and N. Nother, “Stimulated Brillouin scattering in graded index multimode optical fiber by excitation of the fundamental mode only,” Proc. SPIE **6582**, 658213 (2007).

[139] M. Dossou, P. Szriftgiser, and A. Goffin, “Theoretical study of stimulated Brillouin scattering (SBS) in polymer optical fibres,” Proc. Symposium IEEE/LEOS Ben. **27**, 175 (2008).

[140] Y. Mizuno and K. Nakamura, “Experimental study of Brillouin scattering in perfluorinated polymer optical fiber at telecommunication wavelength,” Appl. Phys. Lett. **97**, 2, 021103 (2010).

[141] Y. Mizuno and K. Nakamura, “Potential of Brillouin scattering in polymer optical

fiber for strain-insensitive high-accuracy temperature sensing," Opt. Lett. **35**, 23, 3985 (2010).

[142] Y. Mizuno, W. Zou, and K. Nakamura, "Fresnel reflection spectra at multimode optical fiber ends with heterodyne detection," Appl. Phys. Express **4**, 012501 (2011).

[143] Y. Mizuno, T. Ishigure, and K. Nakamura, "Brillouin gain spectrum characterization in perfluorinated graded-index polymer optical fiber with 62.5-μm core diameter," IEEE Photon. Technol. Lett. **23**, 1863 (2011).

[144] Y. Mizuno, P. Lenke, K. Krebber, and K. Nakamura, "Characterization of Brillouin gain spectra in polymer optical fibers fabricated by different manufacturers at 1.32 and 1.55 μm," IEEE Photon. Technol. Lett. **24**, 1496 (2012).

[145] Y. Mizuno, M. Kishi, K. Hotate, T. Ishigure, and K. Nakamura, "Observation of stimulated Brillouin scattering in polymer optical fiber with pump-probe technique," Opt. Lett. **36**, 2378 (2011).

[146] Y. Mizuno and K. Nakamura, "Enhancement of Brillouin scattering signal in optical fibers by use of pulsed pump light," Appl. Phys. Express **5**, 032501 (2012).

[147] Y. Mizuno, N. Hayashi, and K. Nakamura, "Simple coupling method for enhancing Brillouin scattering signal in polymer optical fibres," Electron. Lett. **48**, 1300 (2012).

[148] Y. Mizuno and K. Nakamura, "Core alignment of butt-coupling between single-mode and multi-mode optical fibers by monitoring Brillouin scattering signal," J. Lightwave Technol. **29**, 2616 (2011).

[149] Y. Mizuno, N. Hayashi, and K. Nakamura, "Fresnel-assisted self-heterodyne detection for Brillouin gain spectrum characterisation in polymer optical fibres," Electron. Lett. **50**, 1153 (2014).

[150] Y. Mizuno, N. Hayashi, and K. Nakamura, "Fiber-optic interferometry using narrowband light source and electrical spectrum analyzer: influence on Brillouin measurement," J. Lightwave Technol. **32**, 4132 (2014).

[151] Y. Mizuno and K. Nakamura, "Brillouin scattering in polymer optical fibers: fundamental properties and potential use in sensors," Polymers, **3**, 886 (2011).

[152] O. Frank and J. Lehmann, "Determination of various deformation processes in impact-modified PMMA at strain rates up to 105 %/min," Colloid Polym. Sci. **264**, 473 (1986).

[153] R. Hill, The mathematical theory of plasticity (Oxford U. Press, New York, 1950).

[154] Y. Mizuno, N. Hayashi, and K. Nakamura, "Fresnel-assisted self-heterodyne detection for Brillouin gain spectrum characterisation in polymer optical fibres," Electron. Lett. **50**, 1153 (2014).

[155] N. Hayashi, Y. Mizuno, and K. Nakamura, "Brillouin gain spectrum dependence on large strain in perfluorinated graded-index polymer optical fiber," Opt. Express **20**, 21101 (2012).

[156] S. Sarva and M.C. Boyce, "Mechanics of Polycarbonate During High Rate Tension," J. Mech. Mater. Struct. **2**, 1853 (2007).

[157] K. Minakawa, N. Hayashi, Y. Shinohara, M. Tahara, H. Hosoda, Y. Mizuno, and K. Nakamura, "Wide-range temperature dependences of Brillouin scattering properties in polymer optical fiber," Jpn. J. Appl. Phys. **53**, 042502 (2014).

[158] A. Minardo, R. Bernini, and L. Zeni, "Distributed temperature sensing in polymer optical fiber by BOFDA," IEEE Photon. Technol. Lett. **24**, 387, 2014.

[159] Y. Mizuno, N. Hayashi, and K. Nakamura, "Polarisation state optimisation in observing Brillouin scattering signal in polymer optical fibres," Electron. Lett. **49**, 56 (2013).

[160] K. Minakawa, N. Hayashi, Y. Shinohara, M. Tahara, H. Hosoda, Y. Mizuno, and K. Nakamura, "Wide-range temperature dependences of Brillouin scattering properties in polymer optical fiber," Jpn. J. Appl. Phys. **53**, 042502 (2014).

[161] W. Zou, Z. He, and K. Hotate, "One-laser-based generation/detection of Brillouin dynamic grating and its application to distributed discrimination of strain and temperature," Opt. Exp. **19**, 2363 (2011).

[162] Y. Mizuno, Z. He, and K. Hotate, "Stable entire-length measurement of fiber strain distribution by Brillouin optical correlation-domain reflectometry with polarization scrambling and noise-floor compensation," Appl. Phys. Express **2**, 062403 (2009).

[163] N. Hayashi, Y. Mizuno, and K. Nakamura, "Observation of stimulated Brillouin scattering in silica graded-index multimode optical fibre based on pump-probe

technique," Electron. Lett. **49**, 366 (2013).

[164] J. Saneyoshi, Y. Kikuchi, and O. Nomoto, Cho-onpa Gijutsu Binran (Handbook of Ultrasonic Technology) (Nikkan Kogyo, Tokyo, 1978).

[165] P. Healey, "Review of long wavelength single-mode optical fiber reflectometry techniques," J. Lightwave Technol. **3**, 876 (1985).

[166] I. R. Husdi, K. Nakamura, and S. Ueha "Sensing characteristics of plastic optical fibres measured by optical time-domain reflectometry," Meas. Sci. Technol. **15**, 1553 (2004).

[167] K. Takada, I. Yokohama, K. Chida, and J. Noda, "New measurement system for fault location in optical waveguide devices based on an interferometric technique,"Appl. Opt. **26**, 1603 (1987).

[168] R. C. Youngquist, S. Carr, and D. E. N. Davies, "Optical coherence-domain reflectometry: a new optical evaluation technique," Opt. Lett. **12**, 158 (1987).

[169] J. P. von der Weid, R. Passy, and N. Gisin, "Mid-range coherent optical frequency domain reflectometry with a DFB laser diode coupled to an external cavity," J. Lightwave Technol. **13**, 954 (1995).

[170] K. Takada, "Fiber-optic frequency encoder for high-resolution OFDR," IEEE Photon. Technol. Lett. **4**, 1174 (1992).

[171] H. Krips, "Atomism, Poincaré and Planck," Stud. Hist. Philos. Sci. **17**, 43 (1986).

[172] S.-Y. Ye, S. Tanaka, M. Esashi, S. Hamakawa, T. Hanaoka, and F. Mizukami, "Thin palladium membrane microreactors with oxidized porous silicon support and their application," J. Micromech. Microeng. **15**, 2011 (2005).

[173] G. S. Weaving and J. Filshie, "A solarimeter utilizing silicon semiconductor diodes," J. Agric. Eng. Res. **22**, 113 (1977).

[174] T. Vietoris, J. L. Ellzey, P. Joulain, S. N. Mehta, and J. L. Torero "Laminar diffusion flame in microgravity: The results of the minitexus 6 sounding rocket experiment," Proc. Combust. Inst. **28**, 2883 (2000).

[175] X. Wang, X. Wang, J. Cui, X. Wang, and J. Zhang "Theoretical Calculation on the Piloted Ignition of PMMA," J. Macromol. Sci. B **46**, 475 (2007).

[176] W. Zou, W. Jiang, and J. Chen, "Characterized Brillouin scattering in silica optical fiber tapers based on Brillouin optical correlation domain analysis," Opt. Express **21**, 6497 (2013).

[177] R. Gravina, G. Testa, and R. Bernini, "Perfluorinated Plastic Optical Fiber Tapers for Evanescent Wave Sensing," Sensors **9**, 10423 (2009).

[178] C. Pulido and O. Esteban, "Multiple fluorescence sensing with side-pumped tapered polymer fiber," Sens. Actuat. B Chem. **157**, 560 (2011).

[179] C. Beres, F. V. B. de Nazare, N. C. C. Souza, M. A. L. Miguel, and M. M. Werneck, "Tapered plastic optical fiber-based biosensor–Tests and application," Biosens. Bioelectron. **30**, 328 (2011).

[180] Y. M. Wong, P. J. Scully, R. J. Bartlett, K. S. C. Kuang, and W. J. Cantwell, "Plastic optical fibre sensors for environmental monitoring: biofouling and strain applications," Strain **39**, 115 (2003).

[181] A. Brockmeyer, J. Coutandin, W. Groh, T. F. Stehlin, and J. Theis, "Passive optical fiber star coupler," Appl. Opt. **31**, 746 (1992).

[182] D. F. Merchant, P. J. Scully and N. F. Schmitt, "Chemical tapering of polymer optical fibre," Sens. Actuat. A: Phys. 76, 365 (1999).

[183] R. Kashyap and K. J. Blow, "Observation of catastrophic self-propelled self-focusing in optical fibres," Electron. Lett. **24**, 47 (1988).

[184] R. Kashyap, "The Fiber Fuse - from a curious effect to a critical issue: A 25th year retrospective," Opt. Express **21**, 6422 (2013).

[185] S. Todoroki, "Fiber Fuse Propagation Behavior," Selected Topics on Optical Fiber Technology (InTech, Croatia, 2012), pp. 551–570.

[186] S. Todoroki, "Origin of periodic void formation during fiber fuse," Opt. Express **13**, 6381 (2005).

[187] C. E. Shannon, “A mathematical theory of communication,” Bell Syst. Tech. J. **27**, 379 (1948).

[188] F. Poletti, N. V. Wheeler, M. N. Petrovich, N. Baddela, E. N. Fokoua, J. R. Hayes, D. R. Gray, Z. Li, R. Slavik, and D. J. Richardson, “Towards high-capacity fibre-optic communications at the speed of light in vacuum,” Nat. Photonics **7**, 279 (2013).

[189] G. Smith and J. Yard, “Quantum Communication with Zero-Capacity Channels,” Science **321**, 1812 (2008).

[190] J. M. Kahn and K. P. Ho, “Communications technology: A bottleneck for optical fibres,” Nature **411**, 1007 (2001).

[191] P. P. Mitra and J. B. Stark, “Nonlinear limits to the information capacity of optical fibre communications,” Nature **411**, 1027 (2001).

[192] T. Morioka, Y. Awaji, R. Ryf, P. Winzer, D. Richardson, and F. Poletti, “Enhancing optical communications with brand new fibers,” IEEE Commun. Mag. **50**, s31 (2012).

[193] M. Jinno, Y. Miyamoto, and Y. Hibino, “Networks: Optical-transport networks in 2015,” Nat. Photonics **1**, 157 (2007).

[194] R. M. Atkins, P. G. Simpkins, and A. D. Yablon, “Track of a fiber fuse: a Rayleigh instability in optical waveguides,” Opt. Lett. **28**, 974 (2003).

[195] Y. Shuto, S. Yanagi, S. Asakawa, M. Kobayashi, and R. Nagase, “Fiber fuse phenomenon in step-index single-mode optical fibers,” IEEE J. Quantum. Electron. **40**, 1113 (2004).

[196] S. Todoroki, “Fiber Fuse Propagation Modes in Typical Single-mode Fibers,” in Proceedings of Optical Fiber Communication/National Fiber Optic Engineers Conference, Anaheim, USA, 2013, paper No. JW2A.11.

[197] E. M. Dianov, A. A. Frolov, I. A. Bufetov, Y. K. Chamorovsky, G. A. Ivanov, and I. L. Vorobjev, "Fiber fuse effect in microstructured fibers," IEEE Photonics Technol. Lett. **16**, 180 (2004).

[198] E. M. Dianov, I. A. Bufetov, A. A. Frolov, V. M. Mashinsky, V. G. Plotnichenko, M. F. Churbanov, and G. E. Snopatin, "Catastrophic destruction of fluoride and chalcogenide optical fibres," Electron. Lett. **38**, 783 (2002).

[199] F. Domingues, A. R. Frias, P. Antunes, A. O. P. Sousa, R. A. S. Ferreira, and P. S. Andre, "Observation of fuse effect discharge zone nonlinear velocity regime in erbium-doped fibres," Electron. Lett. 48, 1295 (2012).

[200] N. Hanzawa, K. Kurokawa, K. Tsujikawa, T. Matsui, K. Nakajima, S. Tomita, and M. Tsubokawa, "Suppression of Fiber Fuse Propagation in Hole Assisted Fiber and Photonic Crystal Fiber," J. Lightwave Technol. **28**, 2115 (2010).

[201] Y. Koike and M. Asai, "The future of plastic optical fiber," NPG Asia Mater. **1**, 22 (2009).

[202] J. Clark and G. Lanzani, "Organic photonics for communications," Nat. Photonics **4**, 438 (2010).

[203] M. Naritomi, H. Murofushi, and N. Nakashima, "Dopants for a Perfluorinated Graded Index Polymer Optical Fiber," Bull. Chem. Soc. Jpn. **77**, 2121 (2004).

[204] D. Gloge and E. A. J. Marcatili, "Multimode theory of graded-core fibers," Bell Syst. Tech. J. **52**, 1563 (1973).

[205] D. P. Hand and T. A. Birks, "Single-mode tapers as 'fibre fuse' damage circuit-breakers," Electron. Lett. **25**, 33 (1989).

[206] E. M. Dianov, I. A. Bufetov, and A. A. Frolov, "Destruction of silica fiber cladding by the fuse effect," Opt. Lett. **29**, 1852 (2004).

[207] K. S. Abedin, M. Nakazawa, and T. Miyazaki, "Backreflected radiation due to a propagating fiber fuse," Opt. Express **17**, 6525 (2009).

Publications related to this dissertation

A. Journal papers

[1] N. Hayashi, Y. Mizuno, and K. Nakamura, “Simplified Brillouin optical correlation-domain reflectometry using polymer optical fiber,” IEEE Photon. J., vol. 7, no. 1, 6800407 (2015).

[2] G. Numata, N. Hayashi, M. Tabaru, Y. Mizuno, and K. Nakamura, “Strain and temperature sensing based on multimode interference in partially chlorinated polymer optical fibers,” IEICE Electron. Express, vol. 12, no. 2, 20141173 (2015).

[3] Y. Mizuno, N. Hayashi, and K. Nakamura, “Fiber-optic interferometry using narrowband light source and electrical spectrum analyzer: influence on Brillouin measurement,” J. Lightwave Technol., vol. 32, no. 24, pp. 4132-4138 (2014).

[4] N. Hayashi, Y. Mizuno, and K. Nakamura, “Alternative implementation of simplified Brillouin optical correlation-domain reflectometry,” IEEE Photon. J., vol. 6, no. 6, 6803108 (2014).

[5] N. Hayashi, Y. Mizuno, and K. Nakamura, “Suppression of ghost correlation peak in Brillouin optical correlation-domain reflectometry,” Appl. Phys. Express, vol. 7, no. 11, 112501 (2014).

[6] N. Hayashi, Y. Mizuno, and K. Nakamura, “Simplified configuration of Brillouin optical correlation-domain reflectometry,” IEEE Photon. J., vol. 6, no. 5, 6802807 (2014).

[7] N. Hayashi, K. Minakawa, Y. Mizuno, and K. Nakamura, “Brillouin frequency shift hopping in polymer optical fiber,” Appl. Phys. Lett., vol. 105, no. 9, 091113

(2014).

[8] Y. Mizuno, S. Ohara, N. Hayashi, and K. Nakamura, “Ultrasonic splicing of polymer optical fibres,” Electron. Lett., vol. 50, no. 19, pp. 1384-1386 (2014).

[9] M. Ding, N. Hayashi, Y. Mizuno, and K. Nakamura, “Brillouin signal amplification in pumped erbium-doped optical fiber,” IEICE Electron. Express, vol. 11, no. 18, 20140627 (2014).

[10] G. Numata, N. Hayashi, M. Tabaru, Y. Mizuno, and K. Nakamura, “Ultra-sensitive strain and temperature sensing based on modal interference in perfluorinated polymer optical fibers,” IEEE Photon. J., vol. 6, no. 5, 6802306 (2014).

[11] H. Ujihara, N. Hayashi, M. Tabaru, Y. Mizuno, and K. Nakamura, “Measurement of large-strain dependence of optical propagation loss in perfluorinated polymer fibers for use in seismic diagnosis,” IEICE Electron. Express, vol. 11, no. 17, 20140707 (2014).

[12] A. A. Jasim, N. Hayashi, S. W. Harun, H. Ahmad, R. Penny, Y. Mizuno, and K. Nakamura, “Refractive index and strain sensing using inline Mach-Zehnder interferometer comprising perfluorinated graded-index plastic optical fiber,” Sens. Actuat. A, vol. 219, pp. 94-99 (2014).

[13] N. Hayashi, Y. Mizuno, and K. Nakamura, “Distributed Brillouin sensing with centimeter-order spatial resolution in polymer optical fibers,” J. Lightwave Technol., vol. 32, no. 21, pp. 3397-3401 (2014).

[14] Y. Mizuno, N. Hayashi, and K. Nakamura, “Fresnel-assisted self-heterodyne detection for Brillouin gain spectrum characterisation in polymer optical fibres,” Electron. Lett., vol. 50, no. 16, pp. 1153-1155 (2014).

[15] Y. Mizuno, N. Hayashi, H. Tanaka, and K. Nakamura, “Spiral propagation of polymer optical fiber fuse accompanied by spontaneous burst and its real-time monitoring using Brillouin scattering,” IEEE Photon. J., vol. 6, no. 3, 6600307

(2014).

[16] N. Hayashi, H. Fukuda, Y. Mizuno, and K. Nakamura, "Observation of Brillouin gain spectrum in tapered polymer optical fiber," J. Appl. Phys., vol. 115, no. 17, 173108 (2014).

[17] Y. Mizuno, N. Hayashi, H. Tanaka, K. Nakamura, and S. Todoroki, "Propagation mechanism of polymer optical fiber fuse," Sci. Rep., vol. 4, 4800 (2014).

[18] K. Minakawa, N. Hayashi, Y. Shinohara, M. Tahara, H. Hosoda, Y. Mizuno, and K. Nakamura, "Wide-range temperature dependences of Brillouin scattering properties in polymer optical fiber," Jpn. J. Appl. Phys., vol. 53, no. 4, 042502 (2014).

[19] Y. Mizuno, N. Hayashi, H. Tanaka, K. Nakamura, and S. Todoroki, "Observation of polymer optical fiber fuse," Appl. Phys. Lett., vol. 104, no. 4, 043302 (2014).

[20] N. Hayashi, Y. Mizuno, and K. Nakamura, "Improved technique for etching overcladding layer of perfluorinated polymer optical fibre by chloroform and water," Electron. Lett., vol. 49, no. 25, pp. 1630-1632 (2013).

[21] N. Hayashi, Y. Mizuno, and K. Nakamura, "Characterization of stimulated Brillouin scattering in polymer optical fibers based on lock-in-free pump-probe technique," J. Lightwave Technol., vol. 31, no. 19, pp. 3162-3166 (2013).

[22] N. Hayashi, Y. Mizuno, and K. Nakamura, "Fast flaw detection in polymer optical fibers with infrared thermometer," Appl. Phys. Express, vol. 6, no. 7, 076601 (2013).

[23] M. Ding, N. Hayashi, Y. Mizuno, and K. Nakamura, "Brillouin gain spectrum dependences on temperature and strain in erbium-doped optical fibers with different erbium concentrations," Appl. Phys. Lett., vol. 102, no. 19, 191906 (2013).

[24] Y. Mizuno, N. Hayashi, and K. Nakamura, "Brillouin scattering signal in polymer

optical fiber enhanced by exploiting pulsed pump with multimode-fiber-assisted coupling technique," Opt. Lett., vol. 38, no. 9, pp. 1467-1469 (2013).

[25] K. Minakawa, N. Hayashi, Y. Mizuno, and K. Nakamura, "Potential applicability of Brillouin scattering in partially chlorinated polymer optical fibers to high-precision temperature sensing," Appl. Phys. Express, vol. 6, no. 5, 052501 (2013).

[26] Y. Mizuno, N. Hayashi, and K. Nakamura, "Broad and flat Brillouin gain spectrum in optical fiber obtained by modulating driving current of laser diode," Jpn. J. Appl. Phys., vol. 52, no. 5R, 058003 (2013).

[27] N. Hayashi, Y. Mizuno, and K. Nakamura, "Observation of stimulated Brillouin scattering in silica graded-index multimode optical fibre based on pump-probe technique," Electron. Lett., vol. 49, no. 5, pp. 366-367 (2013).

[28] Y. Mizuno, N. Hayashi, and K. Nakamura, "Polarisation state optimisation in observing Brillouin scattering signal in polymer optical fibres," Electron. Lett., vol. 49, no. 1, pp. 56-57 (2013).

[29] Y. Mizuno, N. Hayashi, and K. Nakamura, "Simple coupling method for enhancing Brillouin scattering signal in polymer optical fibres," Electron. Lett., vol. 48, no. 20, pp. 1300-1301 (2012).

[30] N. Hayashi, Y. Mizuno, and K. Nakamura, "Brillouin gain spectrum dependence on large strain in perfluorinated graded-index polymer optical fiber," Opt. Express, vol. 20, no. 19, pp. 21101-21106 (2012).

[31] Y. Mizuno, N. Hayashi, and K. Nakamura, "Dependences of Brillouin frequency shift on strain and temperature in optical fibers doped with rare-earth ions," J. Appl. Phys., vol. 112, no. 4, 043109 (2012).

[32] N. Hayashi, Y. Mizuno, D. Koyama, and K. Nakamura, "Dependence of Brillouin frequency shift on temperature and strain in poly(methyl methacrylate)-based polymer optical fibers estimated by acoustic velocity measurement," Appl. Phys.

Express, vol. 5, no. 3, 032502 (2012).

[33] N. Hayashi, Y. Mizuno, D. Koyama, and K. Nakamura, “Measurement of acoustic velocity in poly(methyl methacrylate)-based polymer optical fiber for Brillouin frequency shift estimation,” Appl. Phys. Express, vol. 4, no. 10, 102501 (2011).

[34] Y. Mizuno, N. Hayashi, H. Tanaka, Y. Wada, and K. Nakamura, “Brillouin scattering in multi-core optical fibers for sensing applications,” Sci. Rep., submitted.

[35] H. Ujihara, N. Hayashi, K. Minakawa, M. Tabaru, Y. Mizuno, and K. Nakamura, “Pilot demonstration of polymer optical fiber tapering with no use of external heat source,” IEEE Photon. Technol. Lett., submitted.

[36] K. Minakawa, N. Hayashi, Y. Mizuno, and K. Nakamura, “Thermal memory effect in polymer optical fibers,” IEEE Photon. Technol. Lett., submitted.

[37] G. Numata, N. Hayashi, M. Tabaru, Y. Mizuno, and K. Nakamura, “Drastic sensitivity enhancement of temperature sensing based on modal interference in polymer optical fibers,” Appl. Phys. Lett., to be submitted.

[38] N. Hayashi, K. Minakawa, Y. Mizuno, and K. Nakamura, “Enhanced long-term stability of Brillouin optical correlation-domain reflectometry using polymer optical fibers based on polarization scrambling,” IEEE Photon. Technol. Lett., to be submitted.

B. International conference papers

[39] Y. Mizuno, N. Hayashi, and K. Nakamura, “Brillouin light scattering in plastic fibers,” Asia Communications and Photonics Conference 2014 (ACP 2014), paper AW4D.2, Shanghai, China, November 11-14, 2014.

[40] N. Hayashi, Y. Mizuno, and K. Nakamura, “Ultra-simple setup for distributed Brillouin sensing,” Asia Communications and Photonics Conference 2014 (ACP 2014), paper AW4D.4, Shanghai, China, November 11-14, 2014.

[41] G. Numata, N. Hayashi, M. Tabaru, Y. Mizuno, and K. Nakamura, “Ultra-sensitive

strain and temperature sensing based on single-mode-multimode-single-mode structure comprising perfluorinated plastic optical fibers," Asia Communications and Photonics Conference 2014 (ACP 2014), paper ATh1I.2, Shanghai, China, November 11-14, 2014.

[42] Y. Mizuno, N. Hayashi, and K. Nakamura, "POF-based distributed Brillouin sensing," 23rd International Conference on Plastic Optical Fibers (POF 2014), paper 10-0930, Yokohama, Japan, October 8-10, 2014.

[43] H. Ujihara, N. Hayashi, M. Tabaru, Y. Mizuno, and K. Nakamura, "Giant-strain dependence of propagation loss in perfluorinated plastic optical fibers," 23rd International Conference on Plastic Optical Fibers (POF 2014), paper P-7, Yokohama, Japan, October 8-10, 2014.

[44] N. Hayashi, K. Minakawa, Y. Mizuno, and K. Nakamura, "Brillouin frequency shift hopping in plastic optical fiber," 23rd International Conference on Plastic Optical Fibers (POF 2014), paper P-22, Yokohama, Japan, October 8-10, 2014.

[45] K. Minakawa, K. Koike, Q. Du, N. Hayashi, Y. Koike, Y. Mizuno, and K. Nakamura, "Brillouin properties influenced by glass transition in plastic optical fibers," 23rd International Conference on Plastic Optical Fibers (POF 2014), paper P-23, Yokohama, Japan, October 8-10, 2014.

[46] G. Numata, N. Hayashi, M. Tabaru, Y. Mizuno, and K. Nakamura, "Strain and temperature sensing based on multimode interference in perfluorinated plastic optical fibers," 23rd International Conference on Plastic Optical Fibers (POF 2014), paper P-24, Yokohama, Japan, October 8-10, 2014.

[47] Y. Mizuno, N. Hayashi, H. Tanaka, and K. Nakamura, "Plastic optical fiber fuse: characterization and real-time monitoring," 23rd International Conference on Plastic Optical Fibers (POF 2014), paper P-25, Yokohama, Japan, October 8-10, 2014.

[48] Y. Mizuno, N. Hayashi, H. Tanaka, K. Nakamura, and S. Todoroki, "Understanding the propagation mechanism of plastic optical fiber fuse," OptoElectronics and

Communication Conference and Australian Conference on Optical Fibre Technology 2014 (OECC/ACOFT 2014), paper WE8F-4, Melbourne, Australia, July 6-10, 2014.

[49] N. Hayashi, Y. Mizuno, and K. Nakamura, “First demonstration of distributed Brillouin measurement with centimeter-order resolution based on plastic optical fibers,” OptoElectronics and Communication Conference and Australian Conference on Optical Fibre Technology 2014 (OECC/ACOFT 2014), paper TU6C-1, Melbourne, Australia, July 6-10, 2014.

[50] Y. Mizuno, N. Hayashi, and K. Nakamura, “Distributed strain and temperature sensing based on Brillouin scattering in plastic optical fibers,” 23rd International Conference on Optical Fibre Sensors (OFS-23), paper 9157-678, Santander, Spain, June 2-6, 2014.

[51] Y. Mizuno, N. Hayashi, H. Tanaka, K. Nakamura, and S. Todoroki, “First observation of fiber fuse phenomenon in polymer optical fibers,” 23rd International Conference on Optical Fibre Sensors (OFS-23), paper 9157-173, Santander, Spain, June 2-6, 2014.

[52] N. Hayashi, H. Fukuda, Y. Mizuno, and K. Nakamura, “First observation of Brillouin scattering in tapered plastic optical fiber,” 23rd International Conference on Optical Fibre Sensors (OFS-23), paper 9157-216, Santander, Spain, June 2-6, 2014.

[53] K. Minakawa, K. Koike, N. Hayashi, Y. Koike, Y. Mizuno, and K. Nakamura, “Evaluation of Brillouin frequency shift and its temperature dependence in poly(pentafluorostyrene)-based polymer optical fibers by ultrasonic pulse-echo technique,” 23rd International Conference on Optical Fibre Sensors (OFS-23), paper 9157-386, Santander, Spain, June 2-6, 2014.

[54] N. Hayashi, Y. Mizuno, and K. Nakamura, “Infrared thermometry for detecting flaws in large-core polymer optical fibers”, 18th International Microoptics Conference (MOC’13), paper K-2, Tokyo, Japan, October 27-30, 2013.

[55] M. Ding, N. Hayashi, Y. Mizuno, and K. Nakamura, “Brillouin scattering in erbium-doped optical fibers: fundamental properties and pumping effect”, 18th International Microoptics Conference (MOC’13), paper H-45, Tokyo, Japan, October 27-30, 2013.

[56] K. Minakawa, N. Hayashi, Y. Shinohara, M. Tahara, H. Hosoda, Y. Mizuno, and K. Nakamura, “Evaluation of Brillouin scattering properties in plastic optical fibers for wide-range temperature sensing”, 18th International Microoptics Conference (MOC’13), paper H-43, Tokyo, Japan, October 27-30, 2013.

[57] M. Ding, N. Hayashi, Y. Mizuno, and K. Nakamura, “Enhancement of Brillouin scattering signal in pumped erbium-doped optical fiber”, 4th Asia-Pacific Optical Sensors Conference 2013 (APOS 2013), paper PI-19, Wuhan, China, October 15-18, 2013.

[58] Y. Mizuno, N. Hayashi, and K. Nakamura, “MMF-assisted POF-to-SMF coupling technique for high-power light injection”, 22nd International Conference on Plastic Optical Fibers (POF 2013), paper 27, Buzios, Brazil, September 11-13, 2013.

[59] N. Hayashi, Y. Mizuno, and K. Nakamura, “Fast flaw detection in plastic optical fibers with infrared thermometer”, 22nd International Conference on Plastic Optical Fibers (POF 2013), paper 25, Buzios, Brazil, September 11-13, 2013.

[60] K. Minakawa, N. Hayashi, Y. Shinohara, M. Tahara, H. Hosoda, Y. Mizuno, and K. Nakamura, “Wide-range temperature dependence of Brillouin frequency shift in plastic optical fiber”, 22nd International Conference on Plastic Optical Fibers (POF 2013), paper 42, Buzios, Brazil, September 11-13, 2013.

[61] S. Ohara, N. Hayashi, Y. Mizuno, and K. Nakamura, “Ultrasonic splicing of plastic optical fibers”, 22nd International Conference on Plastic Optical Fibers (POF 2013), paper 33, Buzios, Brazil, September 11-13, 2013.

[62] Y. Mizuno, N. Hayashi, and K. Nakamura, "Optimized polarization state for self-heterodyne-based Brillouin measurement in plastic optical fibers", 10th Conference on Lasers and Electro-Optics Pacific Rim, and the 18th

OptoElectronics and Communications Conference / Photonics in Switching 2013 (CLEO-PR & OECC/PS 2013), paper MS2-4, Kyoto, June 30 - July 4, 2013.

[63] Y. Mizuno, N. Hayashi, and K. Nakamura, "Bandwidth-adjustable ultra-flat Brillouin scattering spectrum in optical fiber", 10th Conference on Lasers and Electro-Optics Pacific Rim, and the 18th OptoElectronics and Communications Conference / Photonics in Switching 2013 (CLEO-PR & OECC/PS 2013), paper WPB-19, Kyoto, June 30 - July 4, 2013.

[64] N. Hayashi, Y. Mizuno, and K. Nakamura, "Stimulated Brillouin scattering in multi-mode optical fibers: toward plastic-fiber-based BOTDA", 10th Conference on Lasers and Electro-Optics Pacific Rim, and the 18th OptoElectronics and Communications Conference / Photonics in Switching 2013 (CLEO-PR & OECC/PS 2013), paper WPF-9, Kyoto, June 30 - July 4, 2013.

[65] K. Minakawa, N. Hayashi, Y. Mizuno, and K. Nakamura, "Potential applicability of Brillouin scattering in partially chlorinated plastic optical fibers to high-precision temperature sensing", 10th Conference on Lasers and Electro-Optics Pacific Rim, and the 18th OptoElectronics and Communications Conference / Photonics in Switching 2013 (CLEO-PR & OECC/PS 2013), paper WPF-12, Kyoto, June 30 - July 4, 2013.

[66] M. Ding, N. Hayashi, Y. Mizuno, and K. Nakamura, “Measurements of Brillouin gain spectra in erbium-doped optical fibers for long-distance distributed strain and temperature sensing,” 21st International Congress on Acoustics (ICA 2013), paper 3aUWa, Montreal, Canada, June 2-7, 2013.

[67] Y. Mizuno, N. Hayashi, and K. Nakamura, “Enhancement of Brillouin signal in plastic optical fibers using pulsed pump with multimode-fiber-assisted coupling,” 5th European Workshop on Optical Fibre Sensors (EWOFS 2013), paper 8794-1, Krakow, Poland, May 19-22, 2013.

[68] N. Hayashi, Y. Mizuno, and K. Nakamura, “Observation and characterization of stimulated Brillouin gain spectra in plastic optical fibers,” 5th European Workshop on Optical Fibre Sensors (EWOFS 2013), paper 8794-26, Krakow, Poland, May

19-22, 2013.

[69] K. Minakawa, N. Hayashi, Y. Mizuno, and K. Nakamura, “Brillouin scattering properties in partially chlorinated plastic optical fibers estimated with ultrasonic pulse-echo technique,” 5th European Workshop on Optical Fibre Sensors (EWOFS 2013), paper 8794-48, Krakow, Poland, May 19-22, 2013.

[70] Y. Mizuno, N. Hayashi, and K. Nakamura, “Brillouin scattering in plastic optical fibers: fundamental properties and sensing applications,” 2012 Photonics Global Conference (PGC 2012), paper 3-4D-1, Sentosa, Singapore, December 13-16, 2012.

[71] N. Hayashi, Y. Mizuno, D. Koyama, and K. Nakamura, “Brillouin frequency shift dependences on temperature and strain in PMMA-based polymer optical fibers estimated by acoustic velocity measurement,” 22nd International Conference on Optical Fibre Sensors (OFS-22), paper 8421-192, Beijing, China, October 15-19, 2012.

[72] Y. Mizuno, N. Hayashi, and K. Nakamura, “Brillouin scattering in plastic optical fibers and its sensor applications,” 21st International Conference on Plastic Optical Fibers (POF 2012), paper 4, Atlanta, USA, September 10-12, 2012.

[73] Y. Mizuno, N. Hayashi, and K. Nakamura, “Simple coupling method for enhancing Brillouin scattering signal in perfluorinated graded-index polymer optical fiber,” 21st International Conference on Plastic Optical Fibers (POF 2012), paper 3-PostD, Atlanta, USA, September 10-12, 2012.

[74] N. Hayashi, Y. Mizuno, and K. Nakamura, “Large-strain sensing using Brillouin scattering in perfluorinated graded-index polymer optical fiber,” 21st International Conference on Plastic Optical Fibers (POF 2012), paper 2, Atlanta, USA, September 10-12, 2012.

[75] N. Hayashi, Y. Mizuno, D. Koyama, and K. Nakamura, “Measurement of acoustic velocity in PMMA polymer optical fiber for Brillouin frequency shift estimation,” 20th International Conference on Plastic Optical Fibers (POF 2011), paper 15,

Bilbao, Basque, Spain, September 14-16, 2011.

[76] N. Hayashi, Y. Mizuno, and K. Nakamura, “Simplified correlation-domain Brillouin sensor using plastic optical fiber,” 5th Asia-Pacific Optical Sensors Conference (APOS 2015), paper T1A-4, Jeju Island, Korea, May 20-22, 2015.

[77] G. Numata, N. Hayashi, M. Tabaru, Y. Mizuno, and K. Nakamura, “Modal-interference-based temperature sensing using plastic optical fibers: markedly enhanced sensitivity near glass-transition temperature,” 5th Asia-Pacific Optical Sensors Conference (APOS 2015), paper P2-47, Jeju Island, Korea, May 20-22, 2015.

[78] K. Minakawa, N. Hayashi, Y. Mizuno, and K. Nakamura, “Experimental study on thermal memory effect in plastic optical fibers,” 20th OptoElectronics and Communications Conference (OECC 2015), Shanghai, China, June 28-July 2, 2015, submitted.

[79] H. Ujihara, N. Hayashi, K. Minakawa, M. Tabaru, Y. Mizuno, and K. Nakamura, “Plastic optical fiber tapering without using external heat source,” 20th OptoElectronics and Communications Conference (OECC 2015), Shanghai, China, June 28-July 2, 2015, submitted.

[80] Y. Mizuno, N. Hayashi, and K. Nakamura, “Distributed Brillouin sensing using plastic optical fibers,” 36th Progress In Electromagnetics Research Symposium (PIERS 2015), Prague, Czech Republic, July 6-9, 2015, submitted.

[81] Y. Mizuno, N. Hayashi, H. Fukuda, and K. Nakamura, “High-performance Brillouin optical correlation-domain reflectometry,” 24th International Conference on Optical Fibre Sensors (OFS-24), Curitiba, Brazil, September 28-October 2, 2015, submitted.

[82] G. Numata, N. Hayashi, M. Tabaru, Y. Mizuno, and K. Nakamura, “Drastic sensitivity enhancement of temperature sensing based on modal interference in plastic optical fibers,” 24th International Conference on Optical Fibre Sensors (OFS-24), Curitiba, Brazil, September 28-October 2, 2015, submitted.

[83] N. Hayashi, K. Minakawa, Y. Mizuno, and K. Nakamura, “Enhanced long-term stability of Brillouin optical correlation-domain reflectometry using plastic optical

fibers based on polarization scrambling,” 24th International Conference on Optical Fibre Sensors (OFS-24), Curitiba, Brazil, September 28-October 2, 2015, to be submitted.

C. Domestic conference papers

[84] 林寧生、水野洋輔、中村健太郎, “BOCDRによる光ファイバ歪・温度分布測定システムの簡素化”, 応用物理学会第54回光波センシング技術研究会(LST-54)講演論文集, pp. 171-176, 東京理科大学神楽坂キャンパス、2014年12月9日-10日.

[85] 沼田剛毅、林寧生、田原麻梨江、水野洋輔、中村健太郎, “特殊プラスチック光ファイバ中のモード間干渉を用いた超高感度歪･温度センシング”, 応用物理学会第54回光波センシング技術研究会(LST-54)講演論文集, pp. 97-102, 東京理科大学神楽坂キャンパス、2014年12月9日-10日.

[86] 水野洋輔、林寧生、中村健太郎, “ポリマー光ファイバ中のブリルアン散乱の工学応用”, 高分子学会2014年度第1回フォトニクスポリマー研究会講演論文集, pp. 3-4, 慶應義塾大学日吉キャンパス、2014年6月26日.

[87] 水野洋輔、林寧生、田中宏樹、中村健太郎, “ポリマー光ファイバヒューズのリアルタイム観測”, 応用物理学会第53回光波センシング技術研究会(LST-53)講演論文集, pp. 133-140, 東京理科大学神楽坂キャンパス、2014年6月18日-19日.

[88] 林寧生、水野洋輔、中村健太郎, “ポリマー光ファイバ中のブリルアン散乱を用いた分布型歪・温度センシング”, 応用物理学会第53回光波センシング技術研究会(LST-53)講演論文集, pp. 127-132, 東京理科大学神楽坂キャンパス、2014年6月18日-19日.

[89] 林寧生、福田英幸、水野洋輔、中村健太郎, “テーパー加工したポリマー光ファイバ中のブリルアン散乱の観測”, 応用物理学会第53回光波センシング技術研究会(LST-53)講演論文集, pp. 25-30, 東京理科大学神楽坂キャンパス、2014年6月18日-19日.

[90] 林寧生、水野洋輔、中村健太郎, “放射温度計測による全フッ素化ポリマー光ファイバ中の欠陥の高速検出”, 応用物理学会第52回光波センシング技術研究会(LST-52)講演論文集, pp. 129-132, 東京理科大学神楽坂キャンパス、2013年12月3日-4日.

[91] 皆川和成、林寧生、篠原百合、田原正樹、細田秀樹、水野洋輔、中村健太郎, “ポリマー光ファイバ中のブリルアン散乱特性の広域温度依存性”, 応用物理学会第52回光波センシング技術研究会(LST-52)講演論文集, pp. 169-174, 東京理科大学神楽坂キャンパス、2013年12月3日-4日.

[92] 丁明杰、林寧生、水野洋輔、中村健太郎, “Characterization of Brillouin scattering properties in erbium-doped optical fibers with different erbium-doping concentrations”, 電子情報通信学会2013年度第2回光ファイバ応用技術研究会(OFT)講演論文集, pp. 5-10, 北海道大学、2013年8月22日-23日.

[93] 林寧生、水野洋輔、中村健太郎, “プラスチック光ファイバ中の誘導ブリルアン散乱の特性評価”, 応用物理学会第51回光波センシング技術研究会(LST-51)講演論文集, pp. 21-26, 東京理科大学神楽坂キャンパス、2013年6月4日-5日.

[94] 皆川和成、林寧生、水野洋輔、中村健太郎, “音速測定による部分塩素化ポリマー光ファイバ中のブリルアン周波数シフト及びその温度依存性の推定”, 応用物理学会第51回光波センシング技術研究会(LST-51)講演論文集, pp. 127-132, 東京理科大学神楽坂キャンパス、2013年6月4日-5日.

[95] 大原修治、林寧生、水野洋輔、中村健太郎, “超音波によるプラスチック光ファイバの突き合わせ接続”, 応用物理学会第51回光波センシング技術研究会(LST-51)講演論文集, pp. 15-20, 東京理科大学神楽坂キャンパス、2013年6月4日-5日.

[96] 林寧生、水野洋輔、中村健太郎, “ポンプ・プローブ法を用いたシリカ系多モード光ファイバ中の誘導ブリルアン散乱の観測”, 応用物理学会第50回光波センシング技術研究会(LST-50)講演論文集, pp. 111-116, 東京理科大学神楽坂キャンパス、2012年12月4日-5日.

[97] 丁明杰、水野洋輔、林寧生、中村健太郎, “エルビウム添加光ファイバ中のブリルアン利得スペクトル　～温度とエルビウム濃度に対する依存性～”, 33rd Symposium on UltraSonic Electronics (USE 2012), paper 2P1-7, 千葉大学, 2012年11月13日-15日.

[98] 林寧生、水野洋輔、中村健太郎, “ブリルアン測定によるポリマー光ファイバ中の音速推定　～大歪依存性の検討～”, 33rd Symposium on UltraSonic Electronics (USE 2012), paper 2E1-1, 千葉大学, 2012年11月13日-15日.

[99] 水野洋輔、林寧生、中村健太郎, “プラスチック光ファイバ中のブリルアン散乱: 歪・温度分布計測への応用”, 電子情報通信学会2014年度第9回光エレクトロニクス研究会(OPE)講演論文集, pp. 39-44, 鹿児島宝山ホール、2015年2月19日-20日 <招待講演>.

[100] 沼田剛毅、林寧生、田原麻梨江、水野洋輔、中村健太郎, “特殊プラスチック光ファイバ中のモード間干渉: 超高感度歪・温度計測への応用”, 電子情報通信学会2014年度第9回光エレクトロニクス研究会(OPE)講演論文集, pp. 137-142, 鹿児島宝山ホール、2015年2月19日-20日 [光エレクトロニクス研究会学生優秀研究賞受賞].

D. Domestic annual meeting presentations

[101] 水野洋輔、林寧生、中村健太郎, “プラスチック光ファイバ中のブリルアン散乱: 歪・温度分布計測への応用”, 電子情報通信学会2014年度第9回光エレクトロニクス研究会(OPE)講演論文集, pp. 39-44, 鹿児島宝山ホール、2015年2月19日-20日.

[102] 沼田剛毅、林寧生、田原麻梨江、水野洋輔、中村健太郎, “特殊プラスチック光ファイバ中のモード間干渉: 超高感度歪・温度計測への応用”, 電子情報通信学会2014年度第9回光エレクトロニクス研究会(OPE)講演論文集, pp. 137-142, 鹿児島宝山ホール、2015年2月19日-20日.

[103] 水野洋輔、林寧生、田中宏樹、中村健太郎, “プラスチック光ファイバヒューズ現象の観測と特性評価”, 2014年（平成26年）秋季第75回応用物理学会学術講演会, 19a-C2-4, 北海道大学札幌キャンパス、2014年9月17日-20日.

[104] 林寧生、皆川和成、水野洋輔、中村健太郎, “プラスチック光ファイバ中のブリルアン周波数シフトホッピング”, 2014 年（平成 26 年）秋季第 75 回応用物理学会学術講演会, 18a-C7-8, 北海道大学札幌キャンパス、2014 年 9 月 17 日-20 日.

[105] 林寧生、水野洋輔、中村健太郎, “プラスチック光ファイバ中のブリルアン散乱を用いた歪・温度分布測定の実証”, 2014 年（平成 26 年）秋季第 75 回応用物理学会学術講演会, 17p-S8-4, 北海道大学札幌キャンパス、2014 年 9 月 17 日-20 日.

[106] 皆川和成、小池康太郎、Qiming Du、林寧生、小池康博、水野洋輔、中村健太郎, “プラスチック光ファイバ中のブリルアン周波数シフトの温度依存性とコアのガラス転移温度との相関”, 2014 年（平成 26 年）秋季第 75 回応用物理学会学術講演会, 17p-C7-2, 北海道大学札幌キャンパス、2014 年 9 月 17 日-20 日.

[107] 沼田剛毅、林寧生、田原麻梨江、水野洋輔、中村健太郎, “全フッ素化プラスチック光ファイバ中の多モード干渉を用いた超高感度歪・温度計測”, 2014 年（平成 26 年）秋季第 75 回応用物理学会学術講演会, 17p-S8-5, 北海道大学札幌キャンパス、2014 年 9 月 17 日-20 日.

[108] 氏原大希，林寧生，田原麻梨江，水野洋輔，中村健太郎, “全フッ素化プラスチック光ファイバ中の光伝搬損失の巨大歪依存性”, 2014 年（平成 26 年）秋季第 75 回応用物理学会学術講演会, 18a-C7-7, 北海道大学札幌キャンパス、2014 年 9 月 17 日-20 日.

[109] 林寧生、福田英幸、水野洋輔、中村健太郎, “テーパー加工したプラスチック光ファイバ中のブリルアン散乱の観測”, 2014 年（平成 26 年）春季第 61 回応用物理学関連連合講演会, 17a-E8-5, 青山学院大学相模原キャンパス、2014 年 3 月 17 日-20 日.

[110] 皆川和成、小池康太郎、林寧生、小池康博、水野洋輔、中村健太郎, “ポリペンタフルオロスチレンに基づくプラスチック光ファイバ中のブリルアン周波数シフトの温度依存性”, 2014 年（平成 26 年）春季第 61 回応用物理学関連連合講演会, 17p-PA2-26, 青山学院大学相模原キャンパス、2014 年 3 月 17 日-20 日.

[111] 大原修治、林寧生、水野洋輔、中村健太郎, “超音波照射条件の検討 －MHz

帯超音波によるポリマー光ファイバの突き合わせ接続(II)－”, 日本音響学会 2013年秋季研究発表会, 2-4-11, 豊橋技術科学大学、2013年9月25日-27日.

[112] 皆川和成、林寧生、篠原百合、田原正樹、細田秀樹、水野洋輔、中村健太郎, “プラスチック光ファイバ中のブリルアン周波数シフトの広域温度依存性”, 2013年（平成25年）秋季第74回応用物理学会学術講演会, 17p-A8-9, 同志社大学京田辺キャンパス、2013年9月16日-20日.

[113] 林寧生、水野洋輔、中村健太郎, “放射温度計測によるプラスチック光ファイバ中の欠陥の高速検出”, 2013年（平成25年）秋季第74回応用物理学会学術講演会, 17p-A8-11, 同志社大学京田辺キャンパス、2013年9月16日-20日.

[114] 林寧生、水野洋輔、中村健太郎, “プラスチック光ファイバ中の誘導ブリルアン散乱特性の評価”, 2013年（平成25年）秋季第74回応用物理学会学術講演会, 17p-A8-10, 同志社大学京田辺キャンパス、2013年9月16日-20日.

[115] 丁明杰、林寧生、水野洋輔、中村健太郎, “励起光入射によるエルビウム添加光ファイバ中のブリルアン散乱信号の増幅”, 2013年（平成25年）秋季第74回応用物理学会学術講演会, 17a-P11-9, 同志社大学京田辺キャンパス、2013年9月16日-20日.

[116] 林寧生、水野洋輔、中村健太郎, “ポンプ・プローブ法を用いたシリカGI-MMF中の誘導ブリルアン散乱の観測”, 2013年（平成25年）春季第60回応用物理学関連連合講演会, 28a-B3-5, 神奈川工科大学、2013年3月27日-30日.

[117] 丁明杰、林寧生、水野洋輔、中村健太郎, “エルビウム添加光ファイバ中のブリルアン散乱特性の解明”, 2013年（平成25年）春季第60回応用物理学関連連合講演会, 28a-B3-6, 神奈川工科大学、2013年3月27日-30日.

[118] 皆川和成、林寧生、水野洋輔、中村健太郎, “音速測定による部分塩素化ポリマー光ファイバ中のブリルアン周波数シフトの推定”, 2013年（平成25年）春季第60回応用物理学関連連合講演会, 27p-PA3-1, 神奈川工科大学、2013年3月27日-30日.

[119] 大原修治、林寧生、水野洋輔、中村健太郎, “MHz帯超音波を用いたポリ

マー光ファイバの突き合わせ接続”, 日本音響学会 2013 年春季研究発表会, 2-4-8, 東京工科大学八王子キャンパス、2013 年 3 月 13 日-15 日.

[120] 林寧生、水野洋輔、小山大介、中村健太郎, “音速測定による PMMA ポリマー光ファイバ中のブリルアン周波数シフトの歪・温度依存性の推定”, 2012 年（平成 24 年）春季第 59 回応用物理学関連連合講演会, 17a-F3-4, 早稲田大学、2012 年 3 月 15 日-18 日.

[121] 林寧生、水野洋輔、小山大介、中村健太郎, “音速測定によるポリマー光ファイバ中のブリルアン周波数シフトの推定,” 2011 年（平成 23 年）秋季第 72 回応用物理学会学術講演会, 30a-P3-3, 山形大学小白川キャンパス、2011 年 8 月 29 日-9 月 2 日.

[122] 林寧生、水野洋輔、中村健太郎, “プラスチック光ファイバを用いたブリルアン光相関領域反射計の簡素化,” 2015 年（平成 27 年）春季第 62 回応用物理学関連連 合講演会, 12a-A13-8, 東海大学湘南キャンパス、2015 年 3 月 11 日-14 日.

[123] 氏原大希、林寧生、皆川和成、田原麻梨江、水野洋輔, 中村健太郎, “外部熱源を用いないプラスチック光ファイバのテーパ加工法の提案,” 2015 年（平成 27 年） 春季第 62 回応用物理学関連連合講演会, 12a-A13-9, 東海大学湘南キャンパス、2015 年 3 月 11 日-14 日.

E. Awards and funds

[124] 林寧生、物理情報システム専攻 優秀研究発表賞 受賞, 東京工業大学, 2012 年 6 月 25 日-26 日.

[125] 林寧生、平成 24 年度 東京工業大学基金奨学金「130 周年記念博士進学エンカレッジ奨学金」助成決定, 東京工業大学, 2012 年 9 月 19 日.

[126] 林寧生、平成 25 年度 日本学術振興会特別研究員(DC1)採用決定, 2013 年 1 月 28 日.

[127] 林寧生、第 28 回 テレコムシステム技術学生賞入賞, 財団法人電気通信普及財団, 2013 年 2 月 12 日.